
DISSERTATION

COLORADO STATE UNIV'S THESIS TEMPLATE

Submitted by

Matthew Gregory Hogan

Department of Physics

In partial fulfillment of the requirements

For the Degree of Doctor of Philosophy

Colorado State University

Fort Collins, Colorado

Summer 2019

Doctoral Committee:

Advisor: Walter Toki

Co-Advisor: Robert Wilson

Norman Buchanan

Wen Zhou

Copyright by Matthew Gregory Hogan 2019

All Rights Reserved

ABSTRACT

COLORADO STATE UNIV'S THESIS TEMPLATE

This document aims to get you started typesetting your thesis or dissertation in L^AT_EX.

ACKNOWLEDGEMENTS

I would like to thank the Elliott Forney for making a publicly accessible L^AT_EX template

Contents

ABSTRACT	ii
ACKNOWLEDGEMENTS	iii
Contents	iv
List of Tables	vii
List of Figures	ix
Chapter 1 Introduction	1
1.1 Introduction to Neutrinos	1
1.1.1 Neutrinos in the Standard Model	3
1.1.1.1 Weak Interactions	4
1.1.1.2 Chirality: How Neutrinos are Left Handed	5
1.1.1.3 Neutrino Scattering with Matter	10
1.1.2 Neutrino Oscillations	13
1.1.2.1 Two Flavor Derivation	14
1.1.2.2 Three Flavor Oscillations	18
1.1.2.3 Matter Effects	23
1.1.3 CP Violation: Origins of Matter	24
1.2 Tokai-to-Kamioka Experiment	25
1.2.1 Neutrino Production at J-PARC	27

1.2.2	Neutrino Near Detectors: ND280	31
1.2.2.1	Multi-pixel photon counter (MPPC)	33
1.2.2.2	On-Axis Detector	33
1.2.2.3	Off-Axis Detector Summary	34
1.2.2.4	Off Axis pi-zero detector (PØD)	38
1.2.2.5	Off Axis Time Projection Chamber (TPC)	40
1.2.2.6	Track Reconstruction in ND280	41
1.2.3	Neutrino Far Detector: Super-Kamiokande	42
1.2.4	ND Constraint	43
1.3	Summary	45
 Chapter 2	BANFF Likelihood	47
2.0.1	Motivation	48
2.0.2	Introduction to Conditional PDFs and Likelihoods	48
2.0.3	BANFF Fit Test Statistic	49
 Chapter 3	The PØD Selections and Samples	54
3.1	Global Reconstruction	55
3.2	PØD Selection Cuts	56
3.2.1	Precuts	56
3.2.2	The ν_μ CC Inclusive in FHC Cut	59
3.2.3	The $\bar{\nu}_\mu$ CC Inclusive in RHC Cuts	59
3.2.4	The ν_μ Background CC Inclusive in RHC Cuts	60
3.3	Selection Kinematics	61
3.3.1	ν_μ in FHC CC 1-Track	66
3.3.2	ν_μ in FHC CC N-Tracks	70
3.3.3	$\bar{\nu}_\mu$ in RHC CC 1-Track	72
3.3.4	$\bar{\nu}_\mu$ in RHC CC N-Tracks	74

3.3.5	ν_μ Background in RHC CC 1-Track	78
3.3.6	ν_μ Background in RHC CC N-Tracks	82
3.4	Summary of Selections	84
Chapter 4	The PØD-Only in BANFF Parameterization	86
4.1	Fit Binning	86
4.1.1	Fit Binning Determination	88
4.2	Penalty Terms and Systematic Uncertainties	89
4.2.1	Flux Model	90
4.2.2	Detector Inefficiencies Model	97
4.2.2.1	Systematic Treatments	97
4.2.2.2	Bin Normalizations and Covariance	99
4.2.2.3	The PØD-Only Systematics	106
4.2.3	Cross Section Model	108
4.2.3.1	Exclusive Channels	108
4.2.3.2	Nuclear Effects	110
4.2.3.3	Fit Parameters	110
Chapter 5	Fitter Validation	114
Chapter 6	Fitter Results	115
Chapter 7	PØD and FGD BANFF Comparisons	116
Bibliography	117
Appendix A	The PØD-Only Bin Normalization Parameters	123

List of Tables

1.1	Sensitivity of Different Oscillation Experiments	19
1.2	Table of Best Fit MNSP Parameters Split by Normal and Inverted hierarchy	23
1.3	PØD Water Target Mass Composition	39
3.1	The PØD WT FV and Corridor Definition	58
3.2	POT Used in This Analysis	61
3.3	The Expanded ν NEUT Reactions Table	63
3.4	The Expanded $\bar{\nu}$ NEUT Reactions Table	64
4.1	Flux Binning and Uncertainties Used in the BANFF Fit	91
4.1	Flux Binning and Uncertainties Used in the BANFF Fit	92
4.1	Flux Binning and Uncertainties Used in the BANFF Fit	93
4.1	Flux Binning and Uncertainties Used in the BANFF Fit	94
4.1	Flux Binning and Uncertainties Used in the BANFF Fit	95
4.2	List of Detector Systematic Effects and Treatment	98
4.3	Cross Section Model Fit Parameters in the BANFF Fit	112
4.3	Cross Section Model Fit Parameters in the BANFF Fit	113
A.1	Observable Normalization Fit Bins	123
A.1	Observable Normalization Fit Bins	124
A.1	Observable Normalization Fit Bins	125
A.1	Observable Normalization Fit Bins	126

A.1 Observable Normalization Fit Bins	127
A.1 Observable Normalization Fit Bins	128
A.1 Observable Normalization Fit Bins	129
A.1 Observable Normalization Fit Bins	130
A.1 Observable Normalization Fit Bins	131
A.1 Observable Normalization Fit Bins	132
A.1 Observable Normalization Fit Bins	133
A.1 Observable Normalization Fit Bins	134
A.1 Observable Normalization Fit Bins	135
A.1 Observable Normalization Fit Bins	136
A.1 Observable Normalization Fit Bins	137
A.1 Observable Normalization Fit Bins	138
A.1 Observable Normalization Fit Bins	139
A.1 Observable Normalization Fit Bins	140
A.1 Observable Normalization Fit Bins	141

List of Figures

1.1	The Standard Model of particle physics	4
1.2	CC And NC Feynman Diagrams	6
1.3	Helicity of Neutrino Through Decay of Charged Pi Mesons	7
1.4	$\nu_e + e^-$ Scattering	11
1.5	A ν_μ -Induced CCQE Interaction	12
1.6	Depiction of Two Neutrino Flavor Change of Basis	16
1.7	Survival and Disappearance Probability	17
1.8	Logarithmic Plot of the Two Flavor Survival Probability	18
1.9	Mass hierarchy Problem And MNSP Representation	21
1.10	Display of the matter and energy content of the Universe	24
1.11	Birds eye view of the T2K experiment on the Japanese archipelago	26
1.12	The T2K Unoscillated ν_μ Flux at SK	26
1.13	Bird's eye view of the J-PARC center	27
1.14	Schematics of the J-PARC Accelerators	28
1.15	The neutrino beamline at J-PARC	29
1.16	Photographs of the Target Station	29
1.17	T2K Accumulated Protons on Target	30
1.18	Schematic of INGRID	32
1.19	Photographs of the T2K MPPC	33
1.20	INGRID Beam Profile	34

1.21	INGRID Event Rate	35
1.22	Schematic of the Off-Axis Near Detector ND280	36
1.23	ND280 Magnetic Field Deviations from a Data Fit	37
1.24	Schematic of the PØD	39
1.25	A cross section of a PØD scintillating bar	40
1.26	Cut-Away Drawing of a TPC Volume in ND280	41
1.27	Diagram of the Super-Kamiokande Detector	42
1.28	Representative T2K Events in Super-Kamiokande	43
1.29	Predicted and Best Fit Measurements for the SK Flux	44
1.30	Predicted CCInc Cross Section at T2K Energies	45
3.1	Data and MC distributions of the ν_μ and $\bar{\nu}_\mu$ water-in CC signal selections	55
3.2	The NEUT Interaction CCQE and non-CCQE Legend	63
3.3	True Particle Selected Legend	64
3.4	NEUT ν Interaction Legend	65
3.5	NEUT $\bar{\nu}$ Interaction Legend	65
3.6	Reconstructed Kinematics for the ν_μ in FHC CC 1-Track Selection for CCQE and non-CCQE Interactions	67
3.7	Reconstructed Kinematics for the ν_μ in FHC CC 1-Track Selection for the True Selected Particle	68
3.8	Efficiency and Purity of ν_μ CCQE Interactions in the ν_μ in FHC CC 1-Track Selection	69
3.9	The ν_μ in FHC CC 1-Track True Kinematics	69
3.10	Lepton Candidate Reconstructed Kinematics for the ν_μ in FHC CC N-Tracks Selection for CCQE and non-CCQE Interactions	70
3.11	Lepton Candidate Reconstructed Kinematics for the ν_μ in FHC CC N-Tracks Selection for the True Selected Particle	71

3.12 Efficiency and Purity of ν_μ CCQE Interactions in the ν_μ in FHC CC N-Tracks Selection	72
3.13 The ν_μ in FHC CC N-Tracks True Kinematics	73
3.14 Reconstructed Kinematics for the $\bar{\nu}_\mu$ in RHC CC 1-Track Selection for CCQE and non-CCQE Interactions	74
3.15 Reconstructed Kinematics for the $\bar{\nu}_\mu$ in RHC CC 1-Track Selection for the True Selected Particle	75
3.16 Efficiency and Purity of $\bar{\nu}_\mu$ CCQE Interactions in the $\bar{\nu}_\mu$ in RHC CC 1-Track Selection	75
3.17 The $\bar{\nu}_\mu$ in RHC CC 1-Track True Kinematics	76
3.18 Lepton Candidate Reconstructed Kinematics for the $\bar{\nu}_\mu$ in RHC CC N-Tracks Selection for CCQE and non-CCQE Interactions	76
3.19 Lepton Candidate Reconstructed Kinematics for the $\bar{\nu}_\mu$ in RHC CC N-Tracks Selections for the True Selected Particle	77
3.20 Efficiency and Purity of $\bar{\nu}_\mu$ CC non-QE Interactions in the $\bar{\nu}_\mu$ in RHC CC N-Tracks Selection	78
3.21 The $\bar{\nu}_\mu$ in RHC CC N-Tracks True Kinematics	79
3.22 Reconstructed Kinematics for the ν_μ in RHC CC 1-Track Selection for CCQE and non-CCQE Interactions	80
3.23 Reconstructed Kinematics for the ν_μ in RHC CC 1-Track Selection for the True Selected Particle	80
3.24 Efficiency and Purity of ν_μ CCQE Interactions in the ν_μ in RHC CC 1-Track Selection	81
3.25 The ν_μ in RHC CC 1-Track True Kinematics	81
3.26 Reconstructed Kinematics for the ν_μ in RHC CC N-Tracks Selection for CCQE and non-CCQE Interactions	82

3.27	Reconstructed Kinematics for the ν_μ in RHC CC N-Tracks Selection for the True Selected Particle	83
3.28	Efficiency and Purity of ν_μ CC non-QE Interactions in the ν_μ in RHC CC N-Tracks Selection	83
3.29	The ν_μ in RHC CC N-Tracks True Kinematics	85
4.1	The PØD Momenta Resolutions Used for Fit Binning	89
4.2	The PØD Angular Residuals Used for Fit Binning	90
4.3	BANFF Pre-fit Flux Covariance Matrix	91
4.4	The T2K Unoscillated Neutrino Flux Prediction at SK	96
4.5	Bin Normalization Edges for the ν_μ in FHC Selections	101
4.6	Bin Normalization Edges for the $\bar{\nu}_\mu$ in RHC Selections	103
4.7	Bin Normalization Edges for the ν_μ in RHC Selections	104
4.8	Event Variations in Observable Normalization Bins	105
4.9	Detector Covariance Matrix	108
4.10	Cross Section Parameters Prefit Covariance Matrix	111

Chapter 1

Introduction

Chose trop vue n'est chère tenue

A thing too much seen is little prized

French proverb

1.1 Introduction to Neutrinos

The history of the neutrino can be traced back to electron energy spectrum observed in neutron β -decay. While measurements of α - and γ -decay of atomic nuclei showed discrete spectral lines, the electron (β particle) exhibited a continuous energy spectrum. Experimentally, there were two observed particles in each decay process and classical physics dictated that the outgoing daughter particles should have discrete energies. The fact that the β -decay spectrum was not this way posed a fundamental problem for physicists in the mid-1910s that energy was not conserved. Two solutions were postulated: either the “energy conservation law is only valid statistically in such a process [...] or an additional undetectable new particle [...] carrying away the additional energy and spin [...] is emitted [50].” The latter solution was proposed by Wolfgang Pauli in a letter dated 4 December 1930 to a group of physicists

meeting in Tübingen, modern Germany, where he first proposed the neutrino¹. Pauli's solution also predicted that the undetected neutrino would have half-integer spin, a quantum mechanical property of matter, since the observed particles in β -decay did not conserve angular momentum. The existence of the neutrino and validation of Pauli's predictions would not be experimentally verified for another 20 years.

The neutrino was first observed in 1953 by Clyde Cowan and Frederick Reines using a nuclear reactor in South Carolina, U.S.A.. Since then three types or "flavors" of neutrinos and antineutrinos have been observed from accelerators and also from unique sources like the Sun and a supernova. Neutrino physics continues to be an active area of physics since neutrinos are unique probes to processes otherwise inaccessible in laboratories. For instance in the depths of the Sun's core where fusion occurs and neutrinos are created, neutrinos are able to travel through the ultra dense and hot medium of the core (over 10^7 degrees Kelvin) and outer layers of the Sun and reach us on Earth.

Neutrinos rarely interact with normal matter, meaning that they travel essentially unimpeded towards one's particle detector. The rarity of such interactions can be illustrated with the fact that given nearly 7.0×10^{10} neutrinos/cm²/sec are incident on the Earth from the Sun², statistically one solar neutrino can harmlessly interact with an individual in their lifetime. So this begs the question: how does one detect a neutrino? The short answer is one requires a large enough flux of neutrinos passing through a large dense volume of matter just to detect one given today's technology.

Scientists continue to be interested in neutrinos due to the unusual properties they exhibit. One of the more recent and surprising aspects about neutrinos is their ability to

¹In W Pauli's December 1930 letter, he referred to his proposed particle as the "neutron", which is not the same neutron known of today. At that point in time, the neutral particles inside the atomic nucleus, also called "neutrons", had not been discovered, let alone understood. The neutron, which was discovered in 1932 by James Chadwick, has been formally associated as the neutral, cousin particle to the proton. It would be Enrico Fermi who would coin the particle in W Pauli's letter and solution to the β -decay spectrum as a "neutrino" meaning in Italian *little neutral one*.

²To give some perspective to this number, this means 70 billion neutrinos are traveling every second through an area similar to one's own thumb nail.

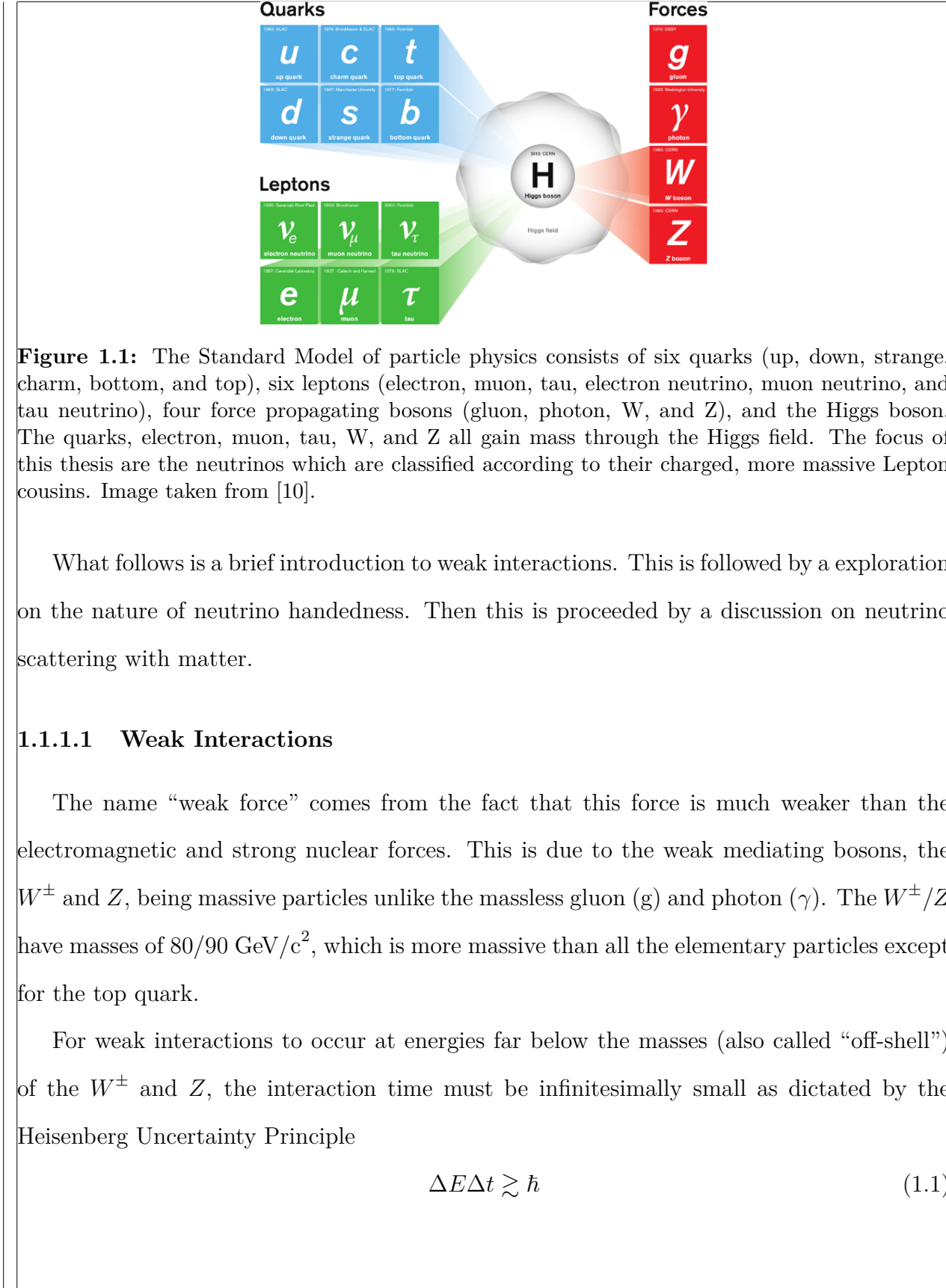
undergo “flavor oscillations” where a neutrino of definite flavor (type) is created and later observed as a different flavor. The impact of differences between neutrino and antineutrino oscillations could help explain the observed matter and anti-matter asymmetry in the Universe which one of the most profound mysteries in physics today.

1.1.1 Neutrinos in the Standard Model

The Standard Model (SM) of particle physics is the theory of elementary or fundamental particle constituents and the forces between them. These standard model forces are the electromagnetic, weak and strong. String theory, which is not yet tested, attempts to incorporate the gravitational force. The SM forces and the gravitational force constitute the four *known* fundamental forces of the Universe. Each force in the SM has at least one “force carrier” particle that mediates the interactions between particles. The force carriers are formally called “gauge bosons” which indicates they are particles with integer $(0, 1, 2, \dots)$ spin that mediate the interaction. The weak nuclear bosons, the charged W^\pm and neutral Z, couple to neutrinos as well as the other fermions, particles with half-integer $(\frac{1}{2}, \frac{3}{2}, \frac{5}{2}, \dots)$ spin, in the SM. All the elementary particles of the SM are shown in Figure 1.1 on page 4.

Neutrinos in the SM are electrically neutral, massless particles categorized into three generations based on their charged, more massive Lepton cousins. The neutrino and charged lepton pair into a “weak isospin doublet” in the SM. These doublets are locally gauge invariant under a $SU(2) \times U(1)$ symmetry which leads to the postulated existence of the photon, the W^\pm and Z bosons. They are necessary to enable local gauge invariance³.

³A gauge theory describes ways to measure physical forces or fields through interactions between elementary particles. The electric or magnetic fields for example can only be probed by charged particles. In the realm of quantum field theories, fields are postulated to permeate everywhere and it is excitations of these fields which produce experimental observables. Fields are constructed using the Lagrangian formalism and altered using gauge transformations. If altering the Lagrangian in some way does not affect the observables, this is referred to as a gauge invariance. Local gauge invariance means that under the constraints of the experiment, certain gauge transformations do not affect the observables. The allowed locally gauge invariant transformations require knowledge of its underlying Lie, or symmetry, group. With the weak isospin doublets, the Lie groups are $SU(2) \times U(1)$ where $SU(2)$ is the special unitary group of 2×2 unitary matrices, and $U(1)$ is the unitary (circle) group consisting of complex numbers of magnitude 1.



where ΔE is the energy of the particle and Δt is the time which the particle exists. As an example, consider a neutrino of energy of 1 GeV emitting a Z-boson of off-shell energy, $\Delta E = 1$ GeV like shown in Figure 1.2 on page 6. The lifetime of that boson is about 10^{-25} seconds according to (1.1). In general, the probability that a massive particle of mass M will be created from the collision of two particles is given by a relativistic Breit–Wigner distribution

$$f(M) \propto \frac{1}{(M^2 - M_0^2)^2 c^4 + M_0^2 \Gamma^2}, \quad (1.2)$$

where M_0 is the rest mass and Γ is the decay width of the particle. For $M \ll M_0$, the probability of creating that particle will be infinitesimally small. Therefore to observe a single weak interaction requires a large amount of weakly interacting particles.

Weak interactions are classified into two classes of interactions: charged current (CC) and neutral current (NC). The CC interactions involve a charged W boson and change the scattering neutrino into a electrically charged lepton of flavor l where the flavor of the neutrino ν_l is inferred from the charged lepton. The same cannot be said of NC interactions which exchange a neutral Z boson. The NC interactions are flavor agnostic since they do not produce a charged lepton. An example of each interaction type is shown in Figure 1.2 on page 6.

1.1.1.2 Chirality: How Neutrinos are Left Handed

Neutrinos are observed to have their spin direction vectors σ opposite to their momentum \mathbf{P} and this is reversed for anti-neutrinos. This property is called helicity and is given by (1.3)

$$\mathcal{H} = \frac{\sigma \cdot \mathbf{P}}{|\mathbf{P}|}. \quad (1.3)$$

Although neutrino detection is difficult, the neutrino helicity is readily inferred from the decay of the daughter muon in the pion decay, $\pi^\pm \rightarrow \mu^\pm + \nu_\mu$. Since a pion has net zero (0) spin, the spin vectors of the daughters must also sum to zero. The muon from a π^+ decay

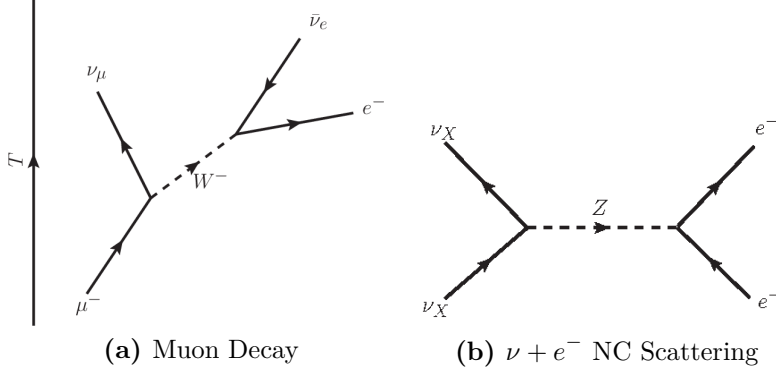


Figure 1.2: (a) Muon decay ($\mu^- \rightarrow \nu_\mu \bar{\nu}_e e^-$) Feynman diagram with time increasing from bottom to top. This is a charged current process that converts a muon into a muon neutrino via the emission of a W boson. Due to a conserved quantum number called lepton number, the W must emit an electron and electron neutrino pair. (b) Neutral current interaction Feynman diagram where time increases from left to right. This is a neutral current interaction where a neutrino of arbitrary flavor X scatters off an electron via the emission of a Z boson.

has negative helicity (-1) hence the neutrino also has negative helicity. To confirm the anti-neutrino's helicity is positive (+1), the interaction requires both a charge (C) conjugation and parity (P) transformation as shown in Figure 1.3 on page 7. A C conjugation is a linear transformation that transforms all particles into their corresponding antiparticles while the P transformation inverts all spatial coordinates. Thus neutrinos are referred to *left-handed* (LH) particles while anti-neutrinos are *right-handed* (RH) particles. It turns out helicity is a useful quantum number to describe neutrinos and coincides with a property called chirality. To understand chirality and its relationship to helicity requires an analysis of the Dirac Lagrangian and Dirac equation.

The Dirac Lagrangian for a free particle field $\psi(x)$ with half-integer spin can be written as

$$\mathcal{L} = \bar{\psi}(x) \left[\frac{i\hbar}{2} \sum_{\mu=0}^3 \gamma^\mu (\vec{\partial}_\mu - \vec{\delta}_\mu) - mc \right] \psi(x) \quad (1.4)$$

where $\psi(x)$ is a four-component vector (spinor) describing a particle field and γ^μ are a set of four 4x4 matrices. The adjoint field $\bar{\psi}(x)$ is defined as

$$\bar{\psi}(x) \equiv \psi^\dagger(x) \gamma^0 \quad (1.5)$$

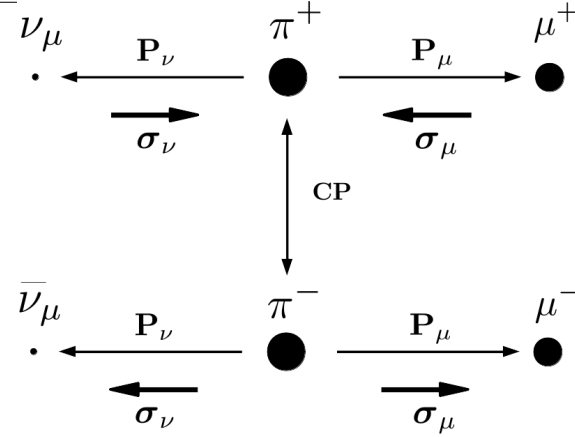


Figure 1.3: Decay of a charged pi meson into a muon and neutrino show the direction of the momentum \mathbf{P} and spin $\boldsymbol{\sigma}$ of the outgoing particles. Since a pion at rest has zero (0) angular momentum, the system of daughter particles must have net zero angular momentum as well. A neutrino (antineutrino) is a right- (left-) handed helicity particle since its spin is (anti-)parallel to its momentum. Application of charge and parity (CP) converts all the particles into their respective antiparticles.

where \dagger denotes the conjugate and transpose operations. The $\overleftrightarrow{\partial}_\mu$ operator is a four-vector defined as

$$\partial_0 = \frac{1}{c} \frac{\partial}{\partial t}, \partial_1 = \frac{\partial}{\partial x}, \partial_2 = \frac{\partial}{\partial y}, \partial_3 = \frac{\partial}{\partial z} \quad (1.6)$$

that acts only on the right of it while $\overleftarrow{\partial}_\mu$ only acts on its left (i.e. $\overline{\psi} \overleftarrow{\partial}_\mu = \partial_\mu \overline{\psi}$). The γ^μ matrices are not unique and different representations dictate different kinematic regimes. The field equations are extracted from the Lagrangian using the Euler-Lagrange procedure. In general for a set of M fields, the field equation are given by

$$\partial_\mu \frac{\partial \mathcal{L}}{\partial (\partial_\mu \psi_r)} - \frac{\partial \mathcal{L}}{\partial \psi_r} = 0 \quad (r = 0, 1, 2, \dots, M-1, M). \quad (1.7)$$

For the Dirac Lagrangian, the field equation for ψ is given by

$$\partial_\mu \frac{\partial \mathcal{L}}{\partial (\partial_\mu \overline{\psi})} - \frac{\partial \mathcal{L}}{\partial \overline{\psi}} = 0 \quad (1.8)$$

which yields the Dirac equation

$$\left[i\hbar \sum_{\mu=0}^3 \gamma^\mu \partial_\mu - mc \right] \psi(x) = 0. \quad (1.9)$$

The representation of the γ^μ matrices that is useful to describe neutrinos is the *Chiral representation* (also called the *Weyl representation*) where

$$\gamma^0 = \begin{bmatrix} 0 & I_2 \\ -I_2 & 0 \end{bmatrix}, \gamma^1 = \begin{bmatrix} 0 & \sigma_x \\ -\sigma_x & 0 \end{bmatrix}, \gamma^2 = \begin{bmatrix} 0 & \sigma_y \\ -\sigma_y & 0 \end{bmatrix}, \gamma^3 = \begin{bmatrix} 0 & \sigma_z \\ -\sigma_z & 0 \end{bmatrix}, \quad (1.10)$$

I_2 is the 2×2 identity matrix, $\sigma_{x,y,z}$ are the Pauli Spin matrices given by

$$\sigma_x = \sigma_1 = \begin{pmatrix} 0 & 1 \\ 1 & 0 \end{pmatrix}, \quad \sigma_y = \sigma_2 = \begin{pmatrix} 0 & -i \\ i & 0 \end{pmatrix}, \quad \sigma_z = \sigma_3 = \begin{pmatrix} 1 & 0 \\ 0 & -1 \end{pmatrix}.$$

Using the Chiral representation, the chirality matrix, γ^5 (the fifth gamma matrix), is defined as

$$\gamma^5 = i\gamma^0\gamma^1\gamma^2\gamma^3 = \begin{bmatrix} I_2 & 0 \\ 0 & -I_2 \end{bmatrix}, \quad (1.11)$$

which is diagonal as well as Hermitian meaning that its eigenvalues are real and observable. Let eigenfunctions of the chirality matrix be denoted with subscripts P and M such that the eigenvalue equations are

$$\begin{aligned} \gamma^5 \psi_P &= +1 \psi_P, \\ \gamma^5 \psi_M &= -1 \psi_M. \end{aligned} \quad (1.12)$$

The field equation solutions to (1.9) can be decomposed into ψ_P and ψ_M projections using two chiral projection operators $\hat{O}_{P,M}$ where

$$\psi = (\hat{O}_P + \hat{O}_M) \psi = \psi_P + \psi_M. \quad (1.13)$$

The chiral operators are explicitly given by

$$\hat{O}_M = \frac{1}{2} (I_4 - \gamma^5) = \begin{pmatrix} 0 & 0 \\ 0 & I_2 \end{pmatrix},$$

$$\hat{O}_P = \frac{1}{2} (I_4 + \gamma^5) = \begin{pmatrix} I_2 & 0 \\ 0 & 0 \end{pmatrix},$$
(1.14)

where I_4 is the 4×4 identity matrix. Taken together (1.13) and (1.14) indicate the free neutrino field is a vector ψ minus axial vector $\gamma^5\psi$, also referred to as V-A, under P transformations. This feature is what allows for the weak force to violate P-symmetry and CP-symmetry. Referring back to (1.4) and (1.7), the Dirac equation becomes a set of coupled equations

$$i\hbar \sum_{\mu=0}^3 \gamma^\mu \partial_\mu \psi_P = mc\psi_M,$$

$$i\hbar \sum_{\mu=0}^3 \gamma^\mu \partial_\mu \psi_M = mc\psi_P$$
(1.15)

where dynamics are set by the mass.

Since the chiral projection operators are decompositions of the identity matrix, the simplest nontrivial solution to ψ is

$$\psi = \begin{pmatrix} \chi_P \\ \chi_M \end{pmatrix}$$
(1.16)

where χ represent two-component spinors. Using 1.16 the Dirac equation in (1.15) can again be rewritten as

$$i\hbar \left[\frac{1}{c} \frac{\partial}{\partial t} + \boldsymbol{\sigma} \cdot \boldsymbol{\nabla} \right] \chi_P = -mc\chi_M,$$

$$i\hbar \left[\frac{1}{c} \frac{\partial}{\partial t} - \boldsymbol{\sigma} \cdot \boldsymbol{\nabla} \right] \chi_M = -mc\chi_P,$$
(1.17)

where

$$\boldsymbol{\sigma} \cdot \boldsymbol{\nabla} = \sigma_x \frac{\partial}{\partial x} + \sigma_y \frac{\partial}{\partial y} + \sigma_z \frac{\partial}{\partial z}.$$
(1.18)

In the limiting case of vanishing mass ($m \rightarrow 0$), as is in the SM, the free particle field equations in (1.17) decouple into

$$\begin{aligned} \left(\frac{E}{c} + \boldsymbol{\sigma} \cdot \mathbf{P} \right) \chi_P &= 0, \\ \left(\frac{E}{c} - \boldsymbol{\sigma} \cdot \mathbf{P} \right) \chi_M &= 0, \end{aligned} \tag{1.19}$$

where the differential operators have been evaluated as the particle's energy E and momentum three-vector \mathbf{P} . For massless neutrinos, χ_P and hence ψ_P , describe particles of negative energy $E = -|\mathbf{P}|c$ which in the context of quantum field theory are interpreted as antiparticles traveling backwards in time. Conversely, ψ_M have positive energy $E = |\mathbf{P}|c$ and which means they are particles traveling forward in time.

If one also multiplies (1.15) by $\gamma^5\gamma^0$ and using the fact that the spin operator $\boldsymbol{\sigma}$ is

$$\boldsymbol{\sigma} = i(\gamma^2\gamma^3, \gamma^3\gamma^1, \gamma^1\gamma^2) = \gamma^0\gamma^k\gamma^5 \quad (k = 1, 2, 3) \tag{1.20}$$

each decoupled equation becomes

$$\frac{\boldsymbol{\sigma} \cdot \mathbf{P}}{|\mathbf{P}|} \psi_{P,M} = \gamma^5 \psi_{P,M} = \pm \psi_{P,M}, \tag{1.21}$$

where one recognizes that helicity and chiral states are the same for $m \rightarrow 0$ only. Thus the labels M and P actually are identical to the LH and RH helicity labels, respectively. Using the results on helicity from before, a neutrino is always observed as a LH particle while the anti-neutrino is always observed as a RH antiparticle.

The observation of only LH neutrinos and RH anti-neutrinos is an important feature in the SM. However, since neutrinos are known to have mass from oscillations, it is theoretically possible to observe a RH neutrino and LH anti-neutrino. That would require boosting to a highly relativistic reference frame with respect to the laboratory.

1.1.1.3 Neutrino Scattering with Matter

Charged current (CC) neutrino interactions on nuclear particles are the interactions used in this thesis. These interactions produce an outgoing charged lepton and a variety of

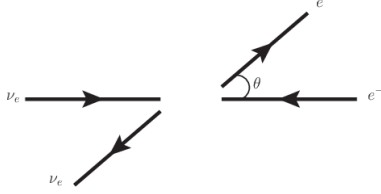


Figure 1.4: The definition of θ in $\nu_e + e^-$ (shown) and $\bar{\nu}_e + e^-$ (not shown) scattering.

hadronic states. While interactions with valence electrons is possible, they are far less common in large, subatomic particle detectors. However, the physics of neutrino-electron scattering is very similar to neutrino-nucleus scattering.

Consider neutrino-electron scattering, the cross section for $\nu_e + e^-$ is given by

$$\frac{d\sigma}{d\Omega} = \left(\frac{G\hbar c}{2\pi} \right)^2 s, \quad (1.22)$$

where G is the Fermi constant and s is the center of mass energy squared. Due to the V-A nature of the Weak force, neutrinos couple to LH particles and RH antiparticles. The outgoing particles are isotropically distributed in the center-of-mass frame since the initial and final spin state of the system is $J = 0$. Compare (1.22) with the cross section for $\bar{\nu}_e + e^-$

$$\frac{d\sigma}{d\Omega} = \left(\frac{G\hbar c}{4\pi} \right)^2 (1 - \cos \theta)^2 s, \quad (1.23)$$

where θ is the observed scattering angle of the electron as shown in Figure 1.4 on page 11. Since the total spin of the $\bar{\nu}_e + e^-$ system is $J = 1$ with z-projection $J_z = 1$, the antineutrino is preferentially forward scattered. Integrating over all angles, the cross sections come out to

$$\sigma(\bar{\nu}_e + e^-) = \frac{1}{3} \sigma(\nu_e + e^-).$$

The factor $1/3$ arises from the fact that angular momentum conservation forbids the $J_z = -1$ and 0 states for $\bar{\nu}_e + e^-$ scattering. The same $1/3$ factor arises between $\nu_\mu + d \rightarrow \mu^- + u$ and $\bar{\nu}_\mu + u \rightarrow \mu^+ + d$ scattering.

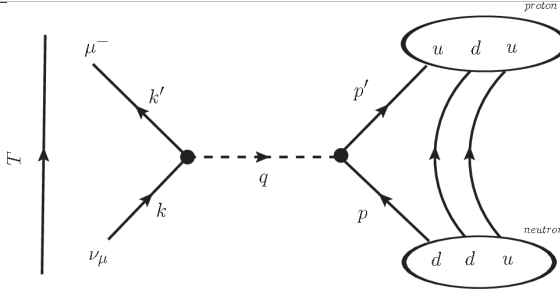


Figure 1.5: A ν_μ -induced CCQE interaction.

In neutrino-nuclear scattering, the simple picture of free quarks must be replaced with the reality of the nuclear medium. Interactions with a single quark are still possible, but nuclear effects can alter the products of the interactions. The kinematics of the particles involved can be altered as well as the existence of a particle can change depending on the point of interaction. Distinctions must be made in neutrino physics between point-like interactions ($\nu_e + e^-$) and post “final state interactions” (FSI) are what is actually observable in an experiment.

Neutrino-nuclear scattering presented in this thesis come in three primary CC varieties: quasi-elastic (CCQE), deep inelastic scattering (CC-DIS), and single pion production (CC- 1π). The ν_μ CCQE interaction refers to the process where an incoming neutrino and neutron (udd) scatter to produce a charged lepton and proton (uud) as shown in Figure 1.5 on page 12. For $\bar{\nu}_\mu$ CCQE, the proton is converted to a neutron instead. The CCQE interaction is the lowest energy CC interaction with a nucleon and is thought of classically to have approximate mass conservation between the proton-neutron states ($\Delta m = 1.29 \text{ MeV}/c^2$). While CCQE models work well to predict the neutrino energy for low-Z atoms like hydrogen, they do not extend well into many nucleon atoms due to similar observable final state nucleons. The CC-DIS interaction, also called CC Other, is a high energy transfer process that shatters the nucleus apart which has the observation of many post-FSI hadrons. Modeling CCDIS can be challenging due to FSI and the uncertainty of the possible initial states of the nucleus. Finally, CC- 1π interactions refer to processes where a post-FSI charged pion is experimentally observed presumably from the decay of resonance state like the $\Delta(1232)$ baryon. These

interactions are not well understood currently since they occur in the transition between CCQE and CCDIS interaction modes.

1.1.2 Neutrino Oscillations

Neutrino oscillations are the observation of a neutrino produced with a particular, definite flavor and later observed as a different flavor. This phenomenon was first observed as a deficit of neutrinos for a number of atmospheric and solar neutrino experiments. The deficit also seemed more pronounced for atmospheric neutrinos as the distance from their source increased. For neutrino oscillations to occur, at least one neutrino must be massive. This observation firmly established that the SM is wrong with its assumption of massless neutrinos.

The first indication of neutrino oscillations was from the Ray Davis Homestake Mine experiment [19] which began in the 1960s. Ray Davis was an expert chemist and designed a radiochemical experiment to measure the flux of neutrinos from Sun. The purpose of this experiment was to test John Bahcall’s prediction of the fusion rate in the Sun and neutrino flux from it as well. Davis’ experiment would need to operate for many years to collect enough statistics due to expected low capture rate. Measurements continued into the 1980s and showed that the flux of neutrinos as measured at Homestake and this was about $\frac{1}{3}$ the expected rate and this became known as the “Solar Neutrino Problem.” The primary solutions were either the solar model was incorrect or the neutrino capture cross section was incorrect. The Sudbury Neutrino Observatory (SNO) was able to resolve this problem by making a model-independent measurement of the solar neutrino flux. SNO observed a ν_e CC-to-NC ratio of 0.301 ± 0.033 , which confirmed that only about 30% of neutrinos arrive as ν_e flavors on Earth. Saying this another way, the majority of neutrinos arrive as the wrong flavor [50].

Another outstanding problem emerged with measurements of atmospheric neutrinos, in particular muon and electron types. Atmospheric neutrinos are produced when high energy

cosmic rays strike atmospheric particles. These cosmic ray collisions generate mostly pions and kaons that decay into neutrinos. When trying to measure the ν_μ/ν_e ratio and comparing that with expected ratio, there was another significant deficit. This was particularly a problem as a function of the zenith angle for the Super-Kamiokande (SK) experiment. SK is a 50kt tank of pure water lined with thousands of photomultiplier tubes designed to observe solar and atmospheric neutrinos. It was the first experiment to perform a neutrino oscillation analysis that successfully explained the deficit.

The observation of neutrino oscillations is relatively new, or about three decades old. Bruno Pontecorvo [38] first proposed such a mechanism in 1957 between neutrinos and antineutrinos much like known neutral K-mesons oscillations. However, oscillations between flavored neutrinos was not expected since it requires the neutrino to have mass. The reasons why are explained in the next subsection.

1.1.2.1 Two Flavor Derivation

The phenomenon of neutrino oscillations can be described with elementary, non-relativistic Quantum Mechanics. Beginning with the Schrödinger Equation in (1.24)

$$-\frac{\hbar}{i} \frac{d}{dt} |\nu(\mathbf{r}, t)\rangle = \hat{H} |\nu(\mathbf{r}, t)\rangle, \quad (1.24)$$

where \hat{H} is the Hamiltonian for the physical system, one considers a massive neutrino of mass m_j in its rest frame (free particle). The Hamiltonian is diagonal in this case, which acting on $|\nu_j\rangle$ results in the eigenvalue equation

$$\hat{H} |\nu_j(\mathbf{r}, t)\rangle = E_j |\nu_j(\mathbf{r}, t)\rangle, \quad (1.25)$$

where E_j is the energy of the neutrino $|\nu_j\rangle$. Substituting (1.25) into (1.24) and solving for $|\nu(\mathbf{r}, t)\rangle$, one obtains the following

$$|\nu_j(\mathbf{r}, t)\rangle = e^{-iE_j t/\hbar} |\nu_j(\mathbf{r}, t=0)\rangle, \quad (1.26)$$

where $|\nu_j(\mathbf{r}, t=0)\rangle$ is created with momentum \mathbf{p} at the origin $\mathbf{r} = 0$. The time-independent solution to (1.24) is a plane-wave given by

$$|\nu_j(\mathbf{r}, t=0)\rangle = e^{i\mathbf{p} \cdot \mathbf{r}/\hbar} |\nu_j\rangle. \quad (1.27)$$

Before being able to describe neutrino oscillations, the basis states must be defined. For this example, consider that there are only two eigenstates, labeled ν_1 and ν_2 , in the “mass” basis with definite mass m_1 and m_2 , respectively. However, experiments can produce neutrinos, as well as probe them, only in a definite flavor state, denoted by a Greek letter subscript λ . Let the generated neutrino, which is a linear superposition of mass states 1 and 2, have momentum \mathbf{p} and flavor α . Since both mass eigenstates share the same momentum momentum \mathbf{p} (but not energy!), the exponential term in (1.27) is an overall phase that will cancel out later. One can postulate a linear transformation, U , between the basis states given by (1.28).

$$\begin{bmatrix} \nu_\alpha \\ \nu_\beta \end{bmatrix} = \begin{bmatrix} U_{11} & U_{12} \\ U_{21} & U_{22} \end{bmatrix} \begin{bmatrix} \nu_1 \\ \nu_2 \end{bmatrix} \quad (1.28)$$

This linear transformation must be a unitary matrix ($U^{-1} = U^\dagger$, \dagger = transpose conjugate) since the states $\nu_{1,2}$ constitute a complete orthonormal basis in the mass basis. With this unitary property, U can be written as a rotation matrix

$$\begin{bmatrix} \nu_\alpha \\ \nu_\beta \end{bmatrix} = \begin{bmatrix} \cos(\theta) & \sin(\theta) \\ -\sin(\theta) & \cos(\theta) \end{bmatrix} \begin{bmatrix} \nu_1 \\ \nu_2 \end{bmatrix}, \quad (1.29)$$

where θ is the angle between the two bases. One can imagine this transformation between bases as shown in Figure 1.6 on page 16 . Creating a neutrino of flavor α and observe it after a time $t = T > 0$, the probability of observing it as flavor $\beta \neq \alpha$ is given by

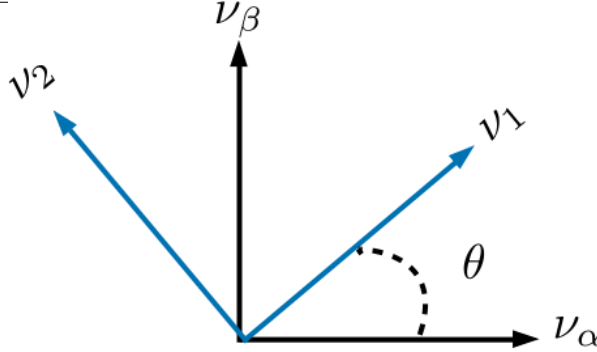


Figure 1.6: The depiction of two neutrino flavor change of basis using a rotation matrix. Compare this with (1.29).

$$\begin{aligned}
 \mathcal{P}(\nu_\alpha \rightarrow \nu_\beta) &= |\langle \nu_\alpha(t=0) | \nu_\beta(t=T) \rangle|^2 \\
 &= |\{\cos(\theta) \langle \nu_1(t=0) | + \sin(\theta) \langle \nu_2(t=0) |\} \\
 &\quad \times \{-\sin(\theta) |\nu_1(t=T)\rangle + \cos(\theta) |\nu_2(t=T)\rangle\}|^2.
 \end{aligned} \tag{1.30}$$

Evaluating all inner products and simplifying terms in (1.30) results in (1.31) below.

$$\mathcal{P}(\nu_\alpha \rightarrow \nu_\beta) = \sin^2(2\theta) \sin^2\left(\frac{E_1 - E_2}{2\hbar} T\right) \tag{1.31}$$

The terminology of “neutrino oscillations” should be more apparent now since (1.31) demonstrates that the probability changes sinusoidally as a function of time T . This equation is not, however, terribly useful in the laboratory frame since it is hard to design an experiment where the travel time an individual neutrino is well known. Instead, one can make useful approximations that are accessible in the laboratory frame. Since neutrinos are nearly massless, they travel very close to the speed of light. Therefore time T is replaced with L/c where L is the distance between the neutrino origin and detection and c is now the speed of light in vacuum. One can also approximate the energy of the mass eigenstate as

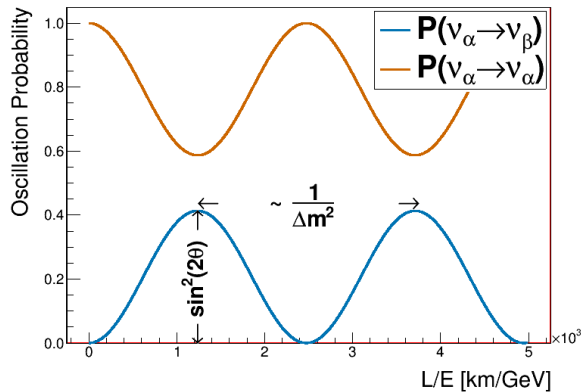


Figure 1.7: Two flavor oscillation probability as a function L/E is shown using $\theta = 20^\circ$ and $\Delta m^2 = 10^{-3} \text{ eV}^2/c^4$. The spacing between adjacent peaks/troughs is proportional to the inverse of Δm^2 . Note that $\mathcal{P}(\nu_\alpha \rightarrow \nu_\alpha) = 1 - \mathcal{P}(\nu_\alpha \rightarrow \nu_\beta)$ since the oscillation probability must always sum to 1.

$$\begin{aligned}
E_j &= \left(m_j^2 c^4 + p_j^2 c^2 \right)^{\frac{1}{2}} = p_j c \left(1 + \frac{m_j^2 c^2}{p_j^2} \right)^{\frac{1}{2}} \\
&\approx p_j c \left(1 + \frac{m_j^2 c^2}{2p_j^2} + \mathcal{O} \left(\frac{m_j c}{p_j} \right)^4 \right) \\
&\approx E_\nu + \frac{m_j^2 c^4}{2E_\nu},
\end{aligned} \tag{1.32}$$

where for oscillation experiments $p_j \gg m_j c$ and $p_j c \approx E_\nu$ where E_ν is the neutrino energy as measured in the laboratory. Substituting these assumptions in (1.31), the oscillation probability is given by

$$\mathcal{P}(\nu_\alpha \rightarrow \nu_\beta) = \sin^2(2\theta) \sin^2 \left(\frac{\Delta m^2 c^3}{4\hbar} \frac{L}{E_\nu} \right), \tag{1.33}$$

where $\Delta m^2 = m_2^2 - m_1^2$ is the mass-squared difference between the mass states. For a momentum consider evaluating all the physical constants in natural units ($c = \hbar = 1$). An appropriate choice of units for Δm^2 , L , and E_ν results in

$$\mathcal{P}(\nu_\alpha \rightarrow \nu_\beta) = \sin^2(2\theta) \sin^2 \left(1.27 \frac{\Delta m^2}{[\text{eV}^2]} \frac{L/E_\nu}{[\text{km}/\text{GeV}]} \right) [\text{natural units}] \tag{1.34}$$

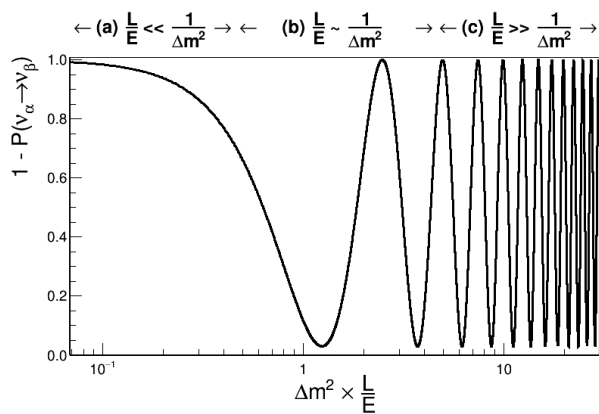


Figure 1.8: Logarithmic plot of the survival probability of flavor α ($1 - \mathcal{P}(\nu_\alpha \rightarrow \nu_\beta) = \mathcal{P}(\nu_\alpha \rightarrow \nu_\alpha)$) over a wide range of L/E values for $\theta = 40^\circ$. The arrows above the plot very roughly denote three possible cases: (a) no oscillations ($L/E \ll 1/\Delta m^2$); (b) sensitivity to oscillations ($L/E \sim 1/\Delta m^2$); (c) only average measurement ($L/E \gg 1/\Delta m^2$). Image originally inspired by [43].

which more clearly demonstrates the Physics in neutrino oscillations. The oscillation probability has an amplitude of $\sin^2(2\theta)$ and varies with frequency inversely proportional to Δm^2 as illustrated in Figure 1.7 on page 17. Since L and E_ν are the only controllable parameters for an oscillation experiment, probing θ or Δm^2 can be difficult unless the experiment can probe a large range of L/E_ν as shown in Figure 1.8 on page 18.

1.1.2.2 Three Flavor Oscillations

In the general case of oscillations using a $n \times n$ mixing matrix, the unitary transformation can be written as a rotation matrix with $\frac{n}{2}(n-1)$ weak mixing angles with $\frac{1}{2}(n-2)(n-1)$ Charge-Parity (CP) violating phases. In addition, oscillations are dictated by a total of $n-1$ mass-squared splittings [50]. This all assumes that neutrinos obey the Dirac Equation, or that they are not their own antiparticles. The favored mixing model is the 3×3 matrix since there are three known neutrino flavors, ν_e , ν_μ , and ν_τ . This means that there are three (3) mixing angles, one (1) CP violating phase, and three (3) mass-squared splittings.

The most frequently used matrix parameterization is the MNSP (MNSP: Maki-Nakagawa-Sakata-Pontecorvo) matrix. Pontecorvo is accredited for first conceiving of neutrino oscilla-

Source	Species	Baseline [km]	Mean Energy [GeV]	$\min(\Delta m^2)$ [eV ²]
Reactor	$\bar{\nu}_e$	1	$\sim 10^{-3}$	$\sim 10^{-3}$
Reactor	$\bar{\nu}_e$	100	$\sim 10^{-3}$	$\sim 10^{-5}$
Accelerator	$\nu_\mu, \bar{\nu}_\mu$	1	~ 1	~ 1
Accelerator	$\nu_\mu, \bar{\nu}_\mu$	10^3	~ 1	$\sim 10^{-3}$
Atmospheric ν 's	$\nu_{e,\mu}, \bar{\nu}_{\mu,e}$	10^4	~ 1	$\sim 10^{-4}$
Sun	ν_e	1.5×10^8	$\sim 10^{-3}$	$\sim 10^{-11}$

Table 1.1: Sensitivity of different oscillation experiments originally published in [45].

tions, albeit between neutrino and anti-neutrinos [37]. It was Maki, Nakagawa, and Sakata who conceived of the parameterization based off the ideas of Pontecorvo [34]. The MNSP matrix is decomposed into separate rotation matrices as given by (1.35)

$$U_{\text{MNSP}} = \underbrace{\begin{bmatrix} 1 & 0 & 0 \\ 0 & c_{32} & s_{32} \\ 0 & -s_{32} & c_{32} \end{bmatrix}}_{U_{32}=U_{\text{atm}}} \times \underbrace{\begin{bmatrix} c_{31} & 0 & s_{31}e^{i\delta_{\text{CP}}} \\ 0 & 1 & 0 \\ -s_{31}e^{-i\delta_{\text{CP}}} & 0 & c_{31} \end{bmatrix}}_{U_{31}=U_{\text{rea}}} \times \underbrace{\begin{bmatrix} c_{21} & s_{21} & 0 \\ -s_{21} & c_{21} & 0 \\ 0 & 0 & 1 \end{bmatrix}}_{U_{21}=U_{\text{sol}}}, \quad (1.35)$$

where

$$c_{ij} = \cos \theta_{ij}, \quad s_{ij} = \sin \theta_{ij}, \quad (1.36)$$

and δ_{CP} represents the CP violating phase. Each rotation matrix U_{ij} represents the different sources for neutrino oscillations experiments with “atm”, “rea”, and “sol” representing atmospheric ν 's, nuclear reactor ν 's, and Solar ν 's, respectively. The sensitivity of neutrino oscillations for different sources is given in Table 1.1 on page 19.

If neutrinos are their own antiparticles, they do not follow the Dirac Equation but do follow the Majorana Equation. This adds two (in general $n-1$) more CP violating Majorana phases, α and β , to the MNSP matrix

$$U_{\text{MNSP}} \rightarrow U_{\text{MNSP}} \times \overbrace{\begin{bmatrix} 1 & 0 & 0 \\ 0 & e^{i\alpha} & 0 \\ 0 & 0 & e^{i\beta} \end{bmatrix}}^{\text{Majorana}}. \quad (1.37)$$

Unfortunately, neutrino oscillations are not able to probe the Majorana phases since the Majorana matrix is diagonal. The question of if neutrinos are Majorana ($\nu = \bar{\nu}$) or Dirac ($\nu \neq \bar{\nu}$) particles is an open question and is being explored by neutrinoless double beta decay experiments [42].

The full three flavor oscillation probability is given by

$$\begin{aligned} \mathcal{P}(\nu_\alpha \rightarrow \nu_\beta) = & \delta_{\alpha\beta} - 4 \sum_{j=1}^3 \left[\sum_{i>j}^3 \text{Re}(K_{\alpha\beta,ij}) \sin^2(\phi_{ij}) \right] \\ & + 4 \sum_{j=1}^3 \left[\sum_{i>j}^3 \text{Im}(K_{\alpha\beta,ij}) \sin(\phi_{ij}) \cos(\phi_{ij}) \right] \end{aligned} \quad (1.38)$$

where

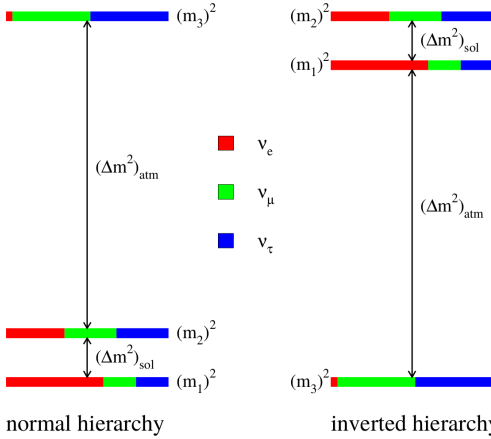
$$K_{\alpha\beta,ij} = U_{\alpha i} U_{\beta i}^* U_{\alpha j}^* U_{\beta j} \quad (1.39)$$

encapsulates the MNSP matrix elements and

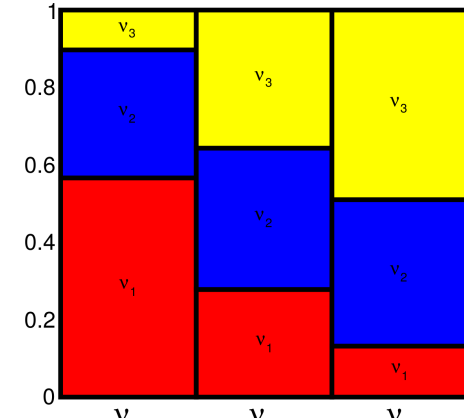
$$\phi_{ij} = \frac{\Delta m_{ij}^2 c^3}{4\hbar} \frac{L}{E_\nu}. \quad (1.40)$$

Since CP violation means that $\mathcal{P}(\nu_\alpha \rightarrow \nu_{\beta \neq \alpha}) \neq \mathcal{P}(\bar{\nu}_\alpha \rightarrow \bar{\nu}_{\beta \neq \alpha})$, CP violating terms must be an odd function of δ_{CP} . Consider the following examples, muon neutrino survival and muon neutrino to electron neutrino appearance.

1.1.2.2.1 Muon Neutrino Survival The probability of a muon type neutrinos surviving is given by



(a) Mass hierarchy as shown in [22]



(b) Mass eigenstate components as shown in [10]

Figure 1.9: Left: the mass hierarchy problem is such that while the solar and atmospheric mixing mass-squared differences are clearly defined, the absolute mass scale is unknown. Since $m_2 > m_1$ by definition, it is currently unknown if m_3 is more or less massive than m_2 , or even massless! Notice the colored bars for each mass eigenstate which corresponded to the approximate flavor content of the neutrino. For example, state “2” has about equal three portions of all three flavors. Right: the mass eigenstate components of each flavor eigenstate. This is a complementary demonstration of the MNSP matrix.

$$\begin{aligned} \mathcal{P} \left({}^{(-)}\bar{\nu}_\mu \rightarrow {}^{(-)}\nu_\mu \right) = & 1 - 4s_{23}^2 c_{13}^2 \left(V_{\cos \delta_{CP}} \right) \sin^2 \phi_{31} \\ & - 4s_{23}^2 c_{13}^2 \left(Z_{\cos \delta_{CP}} \right) \sin^2 \phi_{32} \\ & - 4 \left(V_{\cos \delta_{CP}} \right) \left(Z_{\cos \delta_{CP}} \right) \sin^2 \phi_{21} \end{aligned} \quad (1.41)$$

where

$$V_{\cos \delta_{CP}} = s_{12}^2 c_{23}^2 + s_{13}^2 s_{23}^2 c_{12}^2 + 2s_{12}s_{13}s_{23}c_{12}c_{23} \cos \delta_{CP} \quad (1.42)$$

$$Z_{\cos \delta_{CP}} = c_{12}^2 c_{23}^2 + s_{13}^2 s_{23}^2 s_{12}^2 - 2s_{12}s_{13}s_{23}c_{12}c_{23} \cos \delta_{CP} \quad (1.43)$$

and ${}^{(-)}\bar{\nu}_\mu$ represents either ν_μ or $\bar{\nu}_\mu$. If a definitive measurement of $\mathcal{P} \left(\nu_\mu \rightarrow \nu_\mu \right) \neq \mathcal{P} \left(\bar{\nu}_\mu \rightarrow \bar{\nu}_\mu \right)$ in vacuum occurs, this implies that the combined C, P and time (CPT) symmetry is violated⁴.

⁴When going to through matter however, the oscillation probability is affected. This is explained more in Section 1.1.2.3.

1.1.2.2.2 Electron Neutrino Appearance The previous subsection briefly explored the muon disappearance probability, which is not tested as a channel for CP violation. Electron neutrino appearance, however, does provide insight into CP violation in the lepton sector. The appearance probability of electron neutrinos types from muon types is given by

$$\begin{aligned} \mathcal{P}\left(^{(\bar{\nu}_\mu)} \rightarrow ^{(\bar{\nu}_e)}\right) = & 4c_{13}^2 s_{13}^2 s_{23}^2 \sin^2 \phi_{31} \\ & + 8 \left(X_{\cos \delta_{\text{CP}}} \right) \cos \phi_{23} \sin \phi_{31} \sin \phi_{21} \\ & - \underbrace{8 \left(Y_{\sin \delta_{\text{CP}}} \right)}_{\text{CP violating}} \sin \phi_{32} \sin \phi_{31} \sin \phi_{21} \\ & + 4 \left(Z_{\cos \delta_{\text{CP}}} \right) s_{12}^2 c_{13}^2 \sin^2 \phi_{21} \end{aligned} \quad (1.44)$$

where

$$X_{\cos \delta_{\text{CP}}} = c_{13}^2 s_{12} s_{13} s_{23} (c_{12} c_{23} \cos \delta_{\text{CP}} - s_{12} s_{13}) \quad (1.45)$$

$$Y_{\sin \delta_{\text{CP}}} = \frac{1}{8} \sin(2\theta_{12}) \sin(2\theta_{13}) \sin(2\theta_{23}) c_{13} \sin \delta_{\text{CP}} \quad (1.46)$$

and (+) represents the sign change from neutrinos to anti-neutrinos. The CP violating term (1.46) is also known as the Jarlskog Invariant and is a measure of CP violation independent of the mixing parameterization [31]. This oscillation channel are of primary importance in current and future proposed accelerator and atmospheric neutrino oscillation experiments.

Current and next generation experiments aim to improve knowledge of the mixing parameters. There are a couple of degeneracies to unravel as well as precise measurement of δ_{CP} . While the two defined mass-squared splittings $\Delta m_{21}^2 = \Delta m_{\text{sol}}^2$ and $\Delta m_{32}^2 = \Delta m_{\text{atm}}^2$ are known, it is unknown which eigenstates are more massive. This problem is known as the mass hierarchy problem and is illustrated in Figure 1.9a on page 21. Normal hierarchy refers to the case where $m_3 > m_2 > m_1$ whereas the inverted hierarchy has $m_2 > m_1 > m_3$. Also knowledge if θ_{23} is in the first octant $\theta \in (0, \pi/2)$ or second octant $\theta \in (\pi/2, \pi/4)$ requires large statistics. Finally the value of δ_{CP} is quite uncertain with values in the 3rd and 4th

Parameter	Normal Hierarchy value	Inverted Hierarchy value	Units
$\Delta m_{32}^2 = \Delta m_{\text{atm}}^2$	2.51 ± 0.05	-2.56 ± 0.04	10^{-3} eV 2
$\Delta m_{21}^2 = \Delta m_{\text{sol}}^2$	7.53 ± 0.18		10^{-5} eV 2
$\sin^2(\theta_{21}) = \sin^2(\theta_{\text{sol}})$	$0.307^{+0.013}_{-0.012}$		1
$\sin^2(\theta_{32}) = \sin^2(\theta_{\text{atm}})$	O1: $0.417^{+0.025}_{-0.028}$ O2: $0.597^{+0.024}_{-0.030}$	O1: $0.421^{+0.033}_{-0.025}$ O2: $0.592^{+0.023}_{-0.030}$	1
$\sin^2(\theta_{31})$	2.12 ± 0.08		10^{-2}
δ_{CP}	217^{+40}_{-28}	280^{+25}_{-28}	degrees

Table 1.2: Table of best fit MNSP parameters split by normal and inverted hierarchy. O1 and O2 correspond to the first octant ($\theta \in (0, \pi/2)$) or second octant ($\theta \in (\pi/2, \pi/4)$). All values except for δ_{CP} are combined values from the Particle Data Group and δ_{CP} is from the 2018 NuFit analysis [23, 45].

quadrants. Best fit measurements of the oscillations parameters is given in Table 1.2 on page 23.

1.1.2.3 Matter Effects

Traveling through matter has the potential to increase the sensitivity of oscillation measurements if the baseline is long enough. Known as the Mikheyev-Smirnov-Wolfenstein (MSW) effect [48], all oscillations are affected by coherent forward scattering of neutrinos with electrons in the media. Taking the example of $(\bar{\nu}_\mu \rightarrow \bar{\nu}_e)$ from (1.41), the MSW effect to first order is

$$\begin{aligned} \mathcal{P}((\bar{\nu}_\mu \rightarrow \bar{\nu}_e)) \rightarrow & \mathcal{P}((\bar{\nu}_\mu \rightarrow \bar{\nu}_e)) + \frac{8\alpha}{\Delta m_{31}^2} (c_{13}^2 s_{13}^2 s_{23}^2) (1 - 2s_{13}^2) \\ & \times \left(\sin^2 \phi_{31} \underbrace{- \left(\frac{\Delta m_{31}^2 c^3}{4\hbar} \frac{L}{E_\nu} \right)}_{\phi_{31}} \cos \phi_{32} \sin \phi_{31} \right), \end{aligned} \quad (1.47)$$

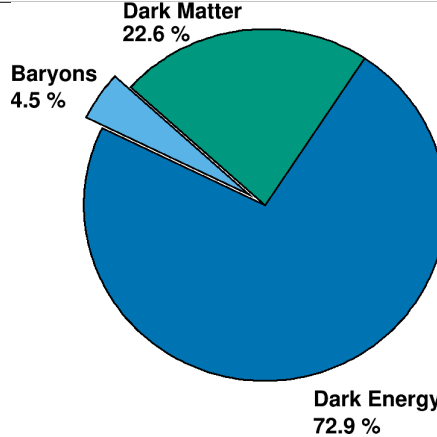


Figure 1.10: Display of the matter and energy content of the Universe. The observed content is 4.5% of baryonic matter. The rest of the Universe consists of non-baryonic matter called Dark Matter and a form of energy called Dark Energy. These inferred parameters are taken from the Λ CDM model, the simplest model that describes the cosmos [32].

where

$$\alpha = 2\sqrt{2}G_F n_e E_\nu \quad (1.48)$$

and G_F is the Fermi constant and n_e is the average electron density of the Earth which the neutrinos travel [12]. Carefully studying (1.47) reveals that the MSW effect alters the oscillation probability as a function of the electron density and increases in magnitude with baseline.

1.1.3 CP Violation: Origins of Matter

To conclude the introduction on neutrinos, it is important to examine the implications of CP violation. The observation of CP violation in the lepton sector might provide critical insight into the origins of the matter. CP violation dictates that certain interactions behave differently between matter or antimatter like $\mathcal{P}(\nu_\mu \rightarrow \nu_e) \neq \mathcal{P}(\bar{\nu}_\mu \rightarrow \bar{\nu}_e)$. The Big Bang Theory suggests that in the first fractions of a second of the Universe, equal amounts of matter and antimatter were created. However, observational evidence shows the Universe consists of only 4.5% baryonic matter (i.e. protons and neutrons) from cosmological models as shown in Figure 1.10 on page 24. The anti-baryonic fraction of the baryonic matter is

infinitesimally low from external constraints on data from gamma-ray telescopes like Fermi-GLAST [46]. This problem is known as the Baryon Asymmetry of the Universe (BAU).

The process of Baryogenesis⁵ is a favored model to explain the BAU and lacks a necessary precursor mechanism. One of the necessary conditions for Baryogenesis [41] is C symmetry violation and CP violation. Evidence of CP violation has been experimentally confirmed in the quarks, but not to the level which resolves the BAU. Baryogenesis can be achieved by having Leptogenesis⁶ occur first through the decay of very heavy, right handed Majorana neutrino ($\nu = \bar{\nu}$) through the *see-saw* mechanism. Detailed discussions on Leptogenesis and the *see-saw* mechanism can found in [10].

1.2 Tokai-to-Kamioka Experiment

The Tokai-to-Kamioka (T2K) experiment is a long baseline, neutrino oscillation experiment hosted in Japan [1] as shown in Figure 1.11 on page 26. It is the successor experiment to the KEK-to-Kamioka neutrino oscillation experiment also hosted in Japan. T2K produces its high intensity, muon neutrino pure beam at the Japan Proton Accelerator Complex (J-PARC), a world class particle accelerator facility. The beam is directed at the Super-Kamiokande (SK) [26] detector which is 295 km away from the source. Along the beamline at 280m from the beam source are a series of near detectors called ND280 [24] to observe and characterize the unoscillated beam. This thesis uses data from ND280 detector to test for increased sensitivity to beam characterization. The beam is designed to maximize the $\nu_\mu \rightarrow \nu_e$ probability at the $L = 295$ km baseline using a neutrino energy spectrum sharply peaked at $E_\nu = 0.6$ GeV as shown in Figure 1.12 on page 26. This spectrum is achieved by directing the center of the beam axis 2.5 degrees off center from SK.

⁵Baryogenesis is the mechanism by which matter and antimatter baryons are created in the early Universe.

⁶Leptogenesis is the mechanism by which leptons and anti-leptons are created in the early Universe.

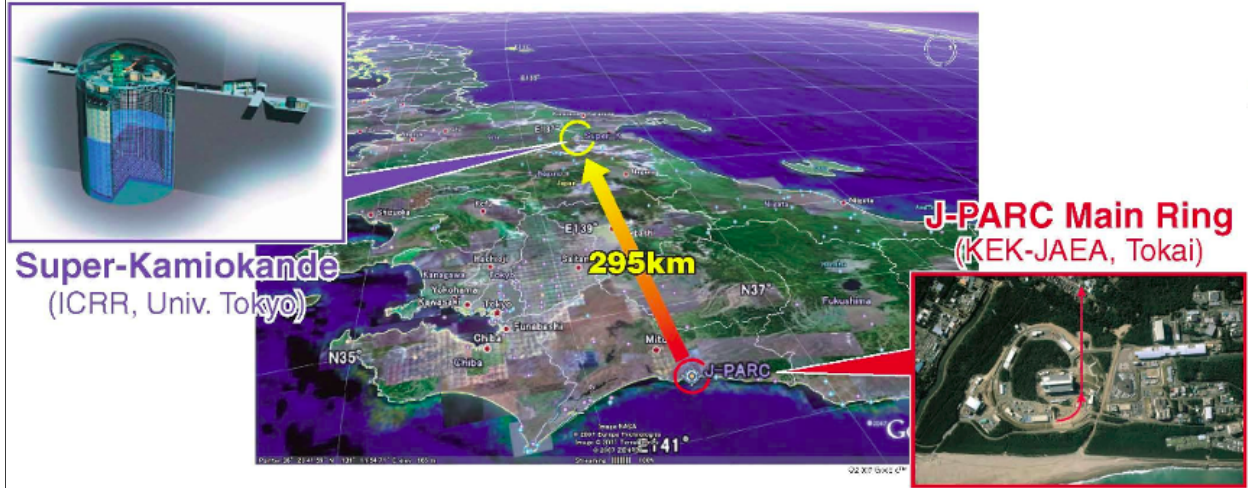


Figure 1.11: Birds eye view of the T2K experiment on the Japanese archipelago. An intense beam of neutrinos are produced at the J-PARC site (bottom right red box) using high energy protons. The beam is directed towards the Super-Kamiokande detector (top left blue box) at a distance of 295 km away from J-PARC.

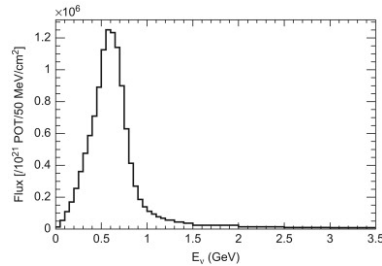


Figure 1.12: The T2K unoscillated ν_μ flux at SK at the off-axis angle of 2.5° .

T2K was primarily designed to measure the last unknown MNSP mixing angle θ_{13} , which was thought to be nearly zero. In addition it set out to measure to high precision the atmospheric mixing parameters, θ_{23} and Δm_{23}^2 . One of its early successes was a landmark 7.3σ measurement of a non-zero θ_{13} using the electron-neutrino appearance measurement [3]. It continues to be a world leader in oscillation physics and as of 2018 rejects CP conserving values ($\delta_{\text{CP}} = 0, \pi$) at the 2σ level [7].

The following topics will be discussed in the following order. First a look how neutrinos are produced at J-PARC. Next a detailed look at the T2K near detectors which are used in this thesis. This is followed by a discussion on Super-Kamiokande, the T2K far detector.

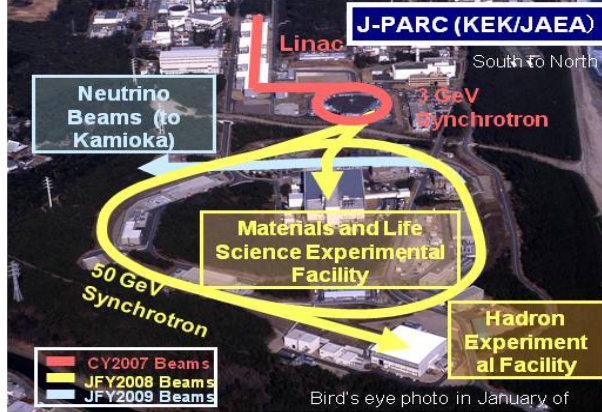


Figure 1.13: Bird's eye view of the J-PARC center showing the primary components of its accelerator programs. To generate the high intensity neutrino beam, first the linear accelerator (Linac, red) accelerates hydrogen ions (protons) into the 3 GeV Synchrotron (also red) called the rapid-cycle synchrotron (RCS). The RCS then injects some of its protons into the 50 GeV Synchrotron (yellow) called the main ring (MR) which currently runs at 30 GeV. Finally the MR protons are directed into a target material along the neutrino beamline (teal) [17].

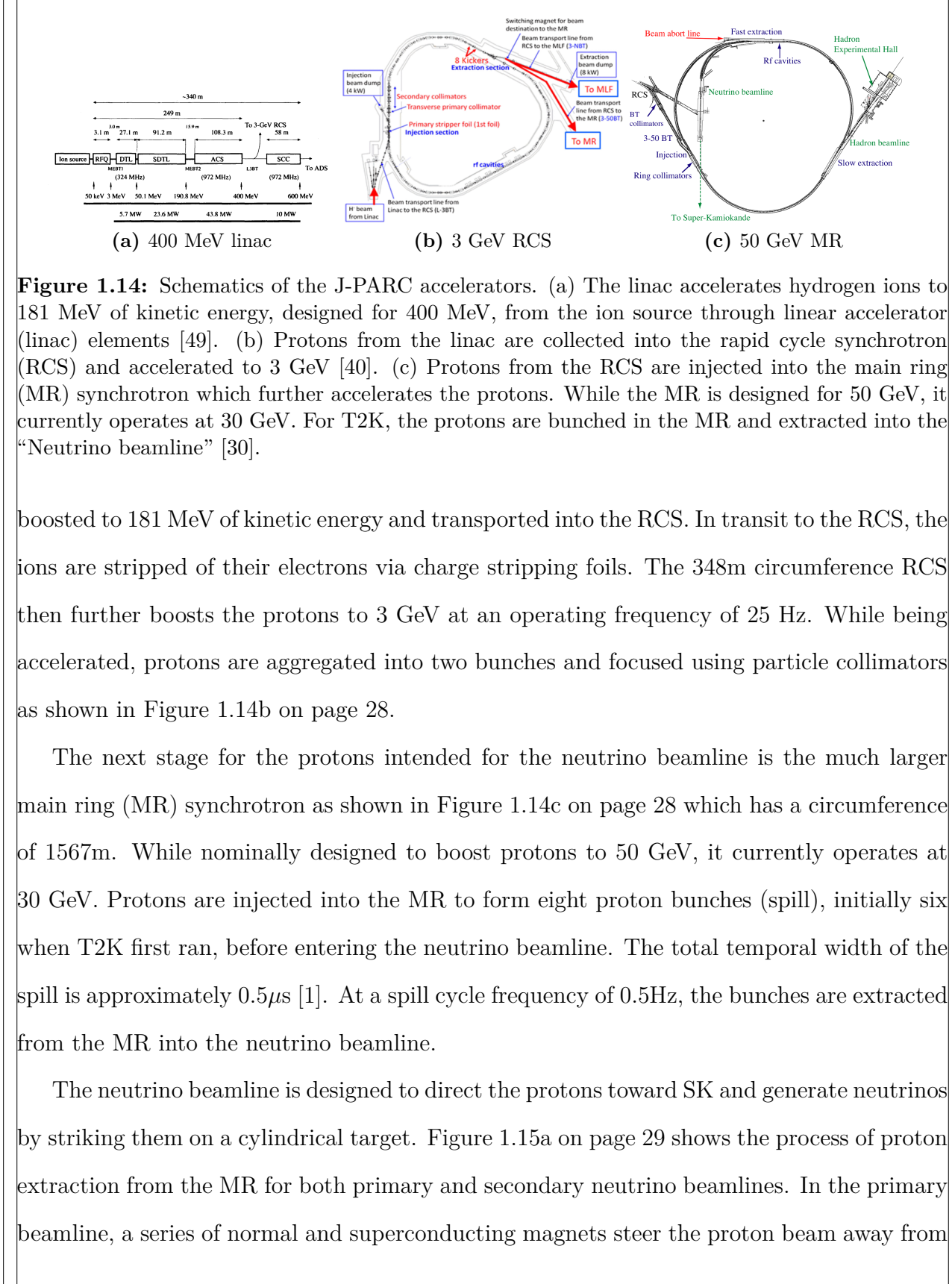
1.2.1 Neutrino Production at J-PARC

To facilitate the high intensity neutrino beam requirements for T2K, the J-PARC site generates a high intensity proton beam through a series of particle accelerators. A bird's eye view of J-PARC can be seen in Figure 1.13 on page 27 which highlights its different accelerators and facilities. For this section, note that all beam energies are kinetic energies.

Protons for the T2K beamline are first accelerated in the J-PARC linear accelerator⁷ (linac) and then the rapid cycle synchrotron⁸ (RCS). Hydrogen ions (${}^1\text{H}^-$) are extracted from plasma in a electrical discharge chamber and feed through a series of linac elements as shown in Figure 1.14a on page 28. Each linac element except for the initial quadrupole magnet apparatus accelerates the ions using carefully coordinated oscillating electric fields generated by radio frequency pulses. After traveling 240m along the linac, the ions have been

⁷A linear accelerator accelerates particles using time varying electric fields along a one direction, terminal beamline. Not only used in particle physics, they are also used in the medical field to generate X-rays.

⁸A synchrotron is cyclic particle accelerator that relies on time varying magnetic fields to accelerate particles. Since they require many magnets and large spaces to operate, they are usually operated at national laboratories for others uses as well like material and life sciences.



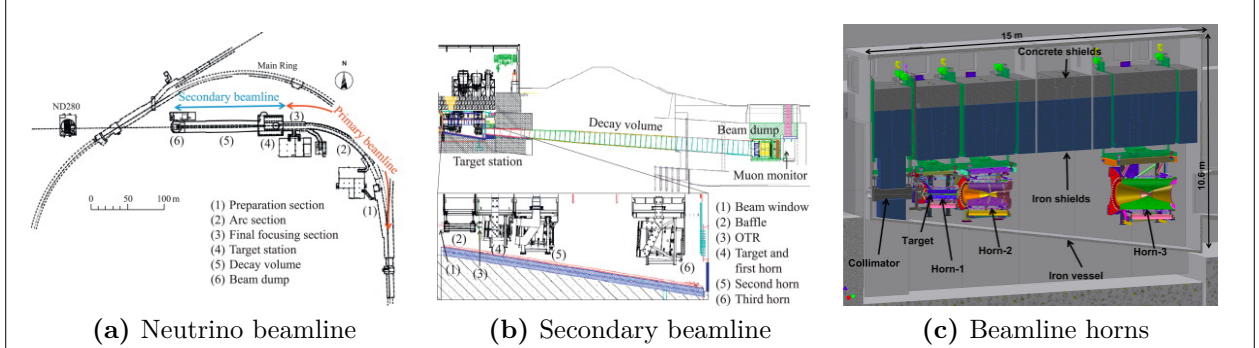
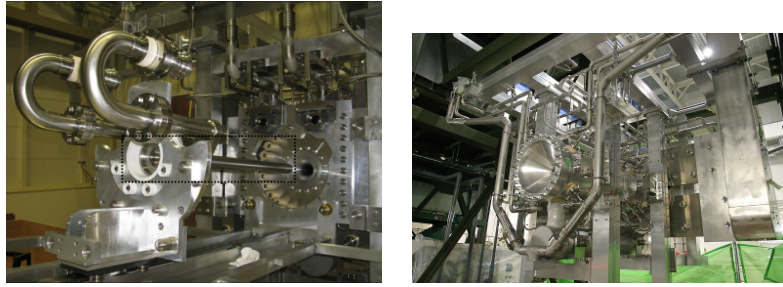


Figure 1.15: The neutrino beamline at J-PARC consists of a primary and secondary beamline. (a) The primary beamline redirects the protons towards the secondary beamline [1]. (b) In the secondary beamline, the protons are impinged on a cylindrical target producing mostly pions. The pions are focused using in sequence horns and decay in a long decay volume. Any non-decayed particles are stopped at the beam dump. (c) A further zoomed in cross section of the target station showing the target and focusing horns [44].



(a) A graphite target being extracted from the target station (b) A magnetic focusing horn

Figure 1.16: Shown are photos of work performed on the target station. (a) The graphite rod being extracted from the target station is shown in the black-dashed box. (b) One focusing horn in T2K.

the MR first along a 54m preparation section and then a 147m arc section to bend the beam towards SK. A final focusing section in the primary beamline focuses the protons into the secondary beam while directing it downwards 3.637° with respect to the local horizontal. Since a well tuned and stable proton beam is necessary for neutrino production, numerous beam monitors are installed along the primary beamline to measure any losses.

The secondary beamline marks the end of the proton beam and production of a neutrino beam. In the secondary beamline, as shown in Figure 1.15b on page 29, it consists of a target station, a decay volume for the outgoing particles from the target station, and a beam dump for any remaining particles. The target station houses a 91.4cm long, 2.6cm

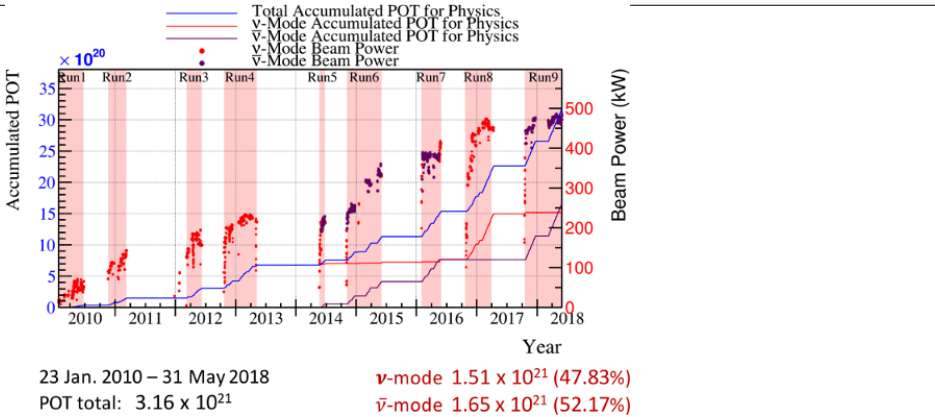


Figure 1.17: T2K accumulated protons on target since 2010 shows a steady increase in beam power over time. The gap between Run2 and Run3 is due to the damage suffered at J-PARC after the 2011 Tōhoku earthquake.

diameter, and $1.8\text{g}/\text{cm}^3$ graphite rod which corresponds to 1.9 radiation lengths. When the protons strike the target, strong (nuclear) interactions produce $\pi(\pi)$ -mesons (pions) and K-mesons (kaons). like those produced from cosmic ray collisions in the upper atmosphere. To enhance the flux of neutrinos, a series of three current pulsed, focusing magnets called horns⁹ as shown in Figure 1.15c on page 29 are used to focus the mesons of the correct charge towards SK. Photographs of a graphite target and focusing horn are shown in Figure 1.16 on page 29. The horns are pulsed at +250kA (-250kA) to select positively (negatively) charged pions. The focused pions are allowed to decay along the 96m long decay volume as to boost the daughter neutrinos along the secondary beamline direction. For safety reasons, the decay volume is filled with gaseous helium at 1 atm of pressure which has a low pion absorption rate. The daughter particles in the decay volume should be mostly muons and muon-neutrinos traveling towards SK. A beam dump is placed at the end of the decay volume to stop particles that have not yet decayed to prevent uncontrolled decay products from contaminating the beam.

Along both beamlines are numerous monitors and timing systems to observe the proton beam to ensure stable production of neutrinos. Proton beam monitors are placed along the

⁹The name horn derives from the fact that the focusing magnets are shaped like brass horns in a music ensemble or marching band. One can think of these horns like a focusing lens for charged particles.

primary beamline to ensure the proton beam is properly steered into the secondary beamline. An optical transition radiation monitor is situated around the target to observe any protons not intersecting with the target region itself. The last monitor along the secondary beamline is the a muon monitor (MUMON), which is placed downstream of the beam dump to observe the daughter muons of > 5 GeV/c momentum [1].

In order to provide timing information for the neutrino beam at SK, a global positioning system (GPS) is used to synchronize clocks at SK and J-PARC. Any event outside the beam timing window are rejected in the T2K oscillation analysis, and so having precise timing information for the neutrino beam is critical for the experiment. The GPS has an internal accuracy of 50ns, or about ~ 150 m assuming the neutrinos are traveling near the speed of light. This is well within the time it takes for any neutrino to travel the 295 km between J-PARC and SK.

J-PARC continues to improve the proton delivery and neutrino modes since T2K began in 2010. T2K has run in two horn current modes: ν -mode and $\bar{\nu}_\mu$ -mode. Focusing positively charged pions with +250 kA horn current is called forward horn current (FHC) mode. Similarly, using -250 kA horn current is called reverse horn current (RHC) mode. The aggregate running of T2K for both FHC and RHC modes are shown in Figure 1.17 on page 30 in units of protons on target (POT).

In addition the proton beam intensity, as measured in kW (energy/proton/second), has been increased over time which increases the number of neutrino interactions observed at SK. Note that while ± 250 kA is the preferred horn current in both FHC and RHC modes, the horns were run briefly at +205kA when operations resumed after 2011 Tōhoku earthquake.

1.2.2 Neutrino Near Detectors: ND280

T2K has a near detector (ND) site at J-PARC that is designed specifically observe the neutrinos in flight aimed at Super-K. The purpose of a ND site is to *constrain the neutrino flux and interaction rate* at SK in order to reduce the impact of their systematic uncertainties

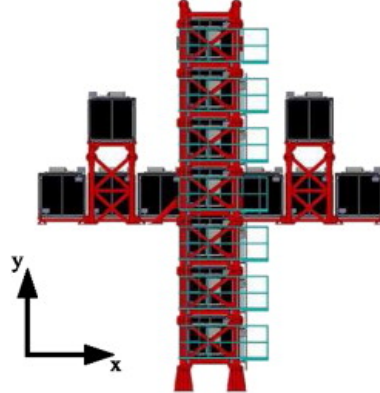


Figure 1.18: A schematic of INGRID shows the arrangement of the tracking scintillating modules. There are 16 identical modules total with seven in the vertical row, seven in the horizontal row, and two at off-axis positions. INGRID is capable of measuring the neutrino beam in a transverse area of $10\text{m} \times 10\text{ m}$. With the vertical row upstream of the horizontal row, the designed beam center intersects each row's center module [2].

in the oscillation analysis. The analysis in this thesis uses the data provided by the off-axis ND. The site is called ND280 and is located 280m away from the production target. The primary detector is an off-axis, magnetized tracking detector consisting of different subdetectors. A separate detector array called the Interactive Neutrino Grid (INGRID) measures the neutrino beam profile. Both on-axis and off-axis detectors extensively utilize a commercial light sensor called a multi-pixel photon counter (MPPC) for the light collection in the scintillator-based detectors.

The following subsections begin with a description of the MPPC technology used in T2K. Next is a description of INGRID and its purpose at ND280. This is followed by a general description primary off-axis, magnetized detector. The last two subsections are descriptions of two primary subdetectors in the off axis detector. The first and second being the pi-zero detector (PØD) and time projection chamber (TPC), respectively.

From here on unless specified, INGRID will refer only to the on-axis ND and ND280 will refer only to off-axis ND.

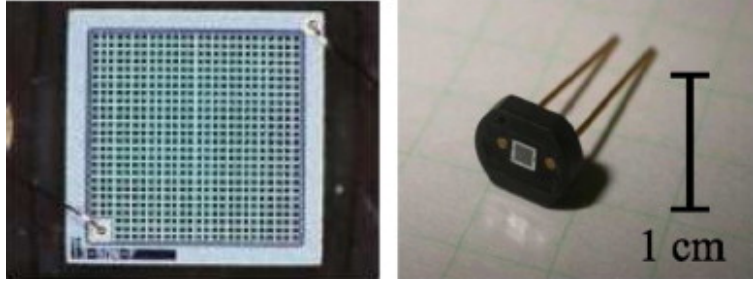


Figure 1.19: Photographs of the specially designed MPPC used in T2K. A magnified face view is shown on the left with an entire unit shown on the right [1].

1.2.2.1 Multi-pixel photon counter (MPPC)

While the reliable photo-multiplier tube (PMT) technology was used in previous scintillator-based detectors, T2K needed a different technology to work in the strong magnetic field environment. T2K selected a commercially available silicon photomultiplier sensor developed by the Hamamatsu corporation called a MPPC. A MPPC is a compact device containing many sensitive avalanche photodiode pixels that act as Geiger micro-counters. They are well matched with the spectral emission of wavelength-shifting (WLS) fibers used to collect the scintillator light in ND280 and operate in a strong magnetic field environment. T2K utilizes specialized 667-pixel MPPCs with an effective area of $1.3\text{ mm} \times 1.3\text{ mm}$ as shown in Figure 1.19 on page 33.

1.2.2.2 On-Axis Detector

The on-axis near detector called the Interactive Neutrino Grid (INGRID) is a tracking scintillator detector designed to directly measure the neutrino beam profile. As shown in Figure 1.18 on page 32, it is a cross grid of tracking modules centered at the designed neutrino beam center ($\theta = 0$). Each module consists of alternating layers of iron plates and scintillator bars except for the two most downstream scintillating layers which lack iron plates. To monitor any beam asymmetry, two separate modules are placed off the grid axis.

Each scintillating bar consists of scintillator-doped polystyrene which emits light when a charged particle deposits energy in the media. Each bar contains a single wavelength-

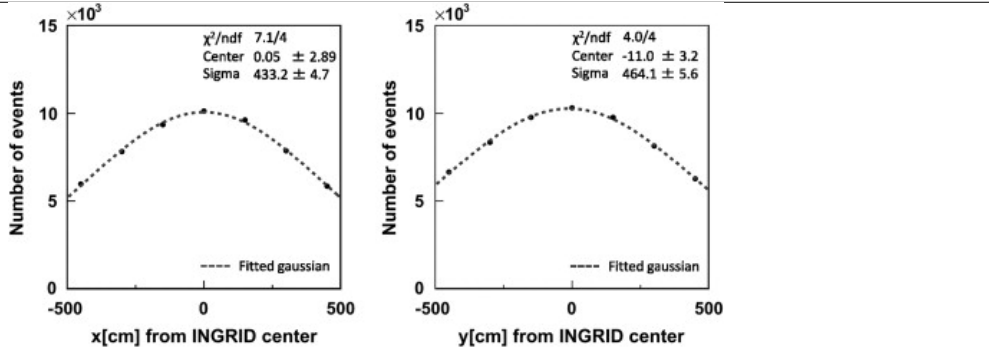


Figure 1.20: A beam profile taken with INGRID in April 2010 shows the Gaussian nature of the beam. The errors on the data points are about 1%. [2]

shifting (WLS) fiber to collect and shift the light to a different energy. The light is collected at a single MPPC device and converted into an electrical signal. In order to enhance the collection efficiency, a reflective TiO_2 doped polystyrene shell surrounds each bar. Bars are assembled into planes to provide tracking capabilities. Veto planes also surround each module to prevent false signals to trigger.

INGRID is continuously operated to check that the neutrino beam center was properly aligned at its designed center. Diagnostic plots such as Figure 1.20 on page 34 are collected on a monthly basis to ensure that the neutrino flux at Super-Kamiokande (SK) is consistent with T2K's design. A history of the beam profile and event rate on INGRID between January 2010 and October 2016 is shown in Figure 1.21 on page 35.

1.2.2.3 Off-Axis Detector Summary

The near detector in T2K is ND280, which is an off-axis, magnetized tracking detector. It is a collection of different detector technologies designed to facilitate three primary measurements:

1. ν_μ flux at SK,
2. Irreducible ν_e background flux at SK, and
3. ν_μ interaction backgrounds and cross sections for the $\nu_\mu \rightarrow \nu_e$ search.

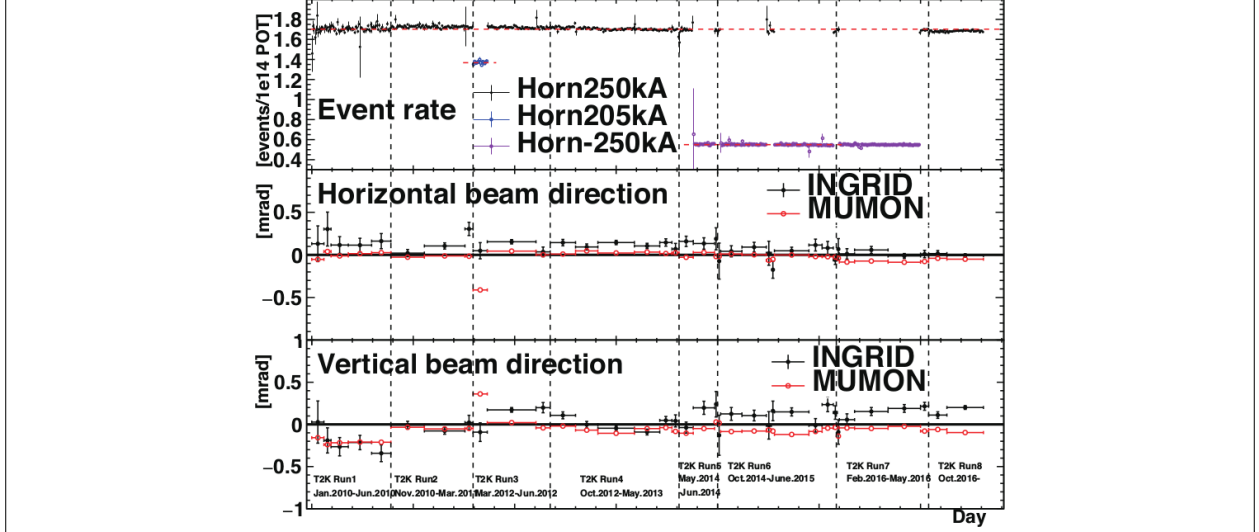


Figure 1.21: INGRID interaction event rate and beam profiles are shown. The top panel shows the event rate for the three different horn currents. The middle and bottom panels show the horizontal and vertical beam directions with respect to the beam center, respectively. A deviation of 1 mrad corresponds to a little under 30 cm. The error bars shown are the statistical errors on the mean.

ND280 consists of the pi-zero detector (PØD), the tracker region consisting of a fine grain detector (FGD) and time projection chamber (TPC), an electromagnetic calorimeter (ECal), and side muon range detector (SMRD). The ND280 subdetectors are instrumented inside the recycled UA1/NOMAD magnet with the SMRD in the magnetic field return yoke itself. All but the FGD is instrumented with the same scintillating-bar bar technology collected by MPPCs. A schematic of the different detector components of ND280 is shown in Figure 1.22 on page 36.

The analysis in this thesis use measurements from the primary subdetectors, the PØD and the TPC. The PØD serves as a massive target for the incident neutrino beam and the TPC serves to measure the charge and momentum of the outgoing particles.

The ND280 magnetic field is generated using electrical current fed through solenoid coils to generate a dipole field of strength 0.2 T^{10} in the x direction. The field is highly uniform

¹⁰This is a powerful magnetic field. According to the The US/UK World Magnetic Model for 2015-2020, the magnetic field strength on the surface of the Earth is about 0.294385 Gauss or $2.94385 \times 10^{-5} \text{ T}$. So the field inside ND280 is about 6800 times more forceful than the Earth's influence [18].

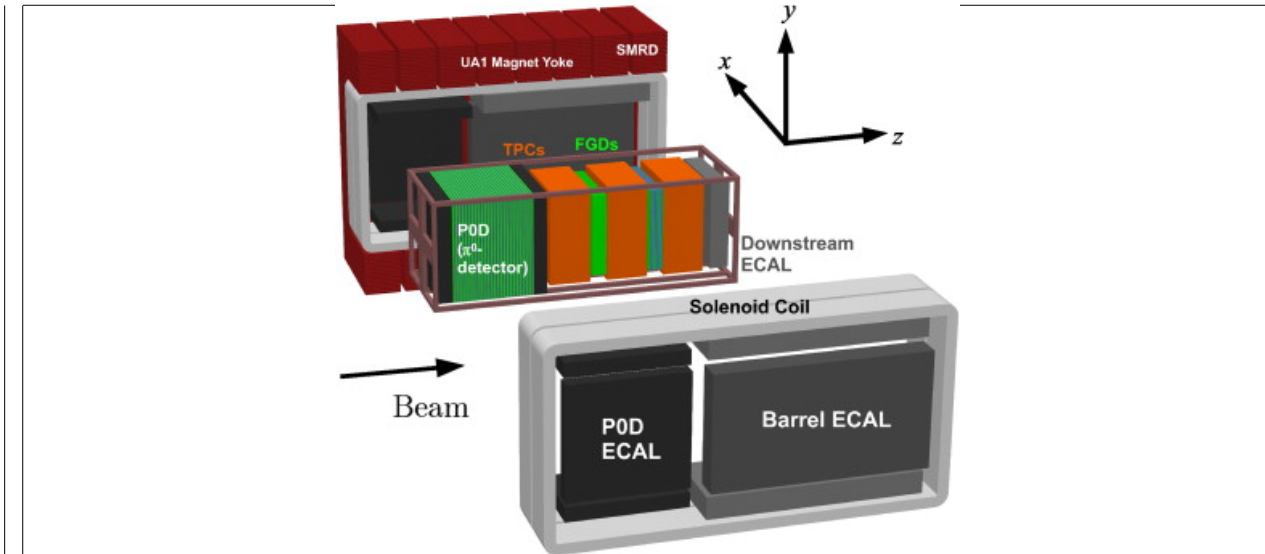


Figure 1.22: An exploded view of the ND280 off-axis detector. The magnetic field is generated from the Solenoid Coil via an electrical current which produces a dipole magnetic field of strength 0.2 T. The field is designed to return to the Magnetic Yoke.

near the center of the detector which is where the majority of the TPC system is located. However, it has significant deviations from 0.2 T near the solenoid edges. In order to fully understand the field inside ND280, a precise 3D model was generated using a machine controlled Hall probe. The operating field strength during the mapping process was 0.07 T due to power restrictions at the time. The model was then compared with measurements in the TPC region as shown in Figure 1.23 on page 37. After scaling the model to the nominal operating strength of 0.2 T, a fractional uncertainty of 10^{-3} or uncertainty of 2 Gauss in each direction was obtained.

The ND280 magnetic field permits the measurements of particle charge and momentum. A particle of charge q , rest mass m_0 , and velocity \mathbf{v} under the influence of an external electric and magnetic fields, \mathbf{E} and \mathbf{B} , respectively, experiences a force \mathbf{F} given by the Lorentz force equation

$$\mathbf{F} = q(\mathbf{E} + \mathbf{v} \times \mathbf{B}). \quad (1.49)$$

Assuming for now that there is no external electric field, the force on the particle is

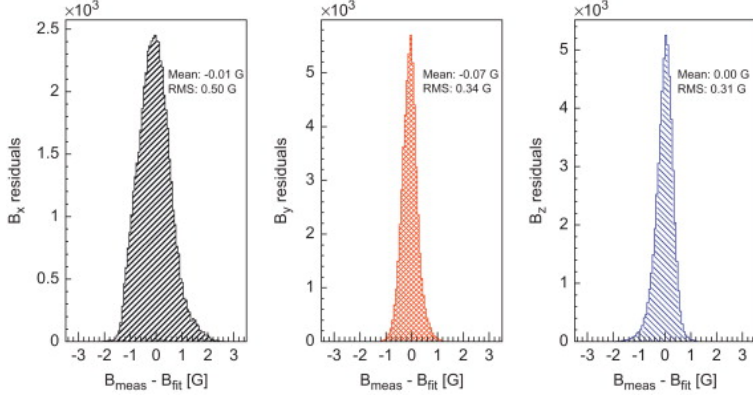


Figure 1.23: Each of the magnetic field components (x, y and z, respectively) are compared between a fit of the data and the actual measurements near the center of ND280. The systematic uncertainty on the field is extracted from the RMS of the mapping [1].

$$\mathbf{F} = q\mathbf{v} \times \mathbf{B}, \quad (1.50)$$

which is both orthogonal to \mathbf{v} and \mathbf{B} . Since the mechanical work on a particle in a magnetic field is zero, the particle's energy is unchanged ($|\mathbf{v}| = v = \text{constant}$). Newton's Second Law allows us to rewrite the force as an change in momentum \mathbf{P}

$$\begin{aligned} \mathbf{F} &= \frac{d\mathbf{P}}{dt} \\ &= \frac{d}{dt} (\gamma(v)m_0\mathbf{v}) \\ &= m_0\mathbf{v} \left(\frac{d\gamma(v)}{dt} \right) + \gamma(v)m_0 \left(\frac{d\mathbf{v}}{dt} \right) \\ &= m_0\mathbf{v} \left(\frac{d\gamma(v)}{dv} \right) \cancel{\left(\frac{dv}{dt} \right)}^0 + \gamma(v)m_0\mathbf{a} \\ &= \gamma(v)m_0\mathbf{a}, \end{aligned} \quad (1.51)$$

where $\mathbf{P} = \gamma(v)m_0\mathbf{v}$ is the relativistic momentum and $\gamma(v) = (1 - (v/c)^2)^{-1/2}$ is the Lorentz factor for relativistic particles. For uniform circular motion, the magnitude of the acceleration is given by

$$|\mathbf{a}| = v^2/R, \quad (1.52)$$

where R is the radius of curvature for the circle. Combining (1.52) and (1.51) with some algebra yields

$$R = \frac{\gamma(v)m_0v}{q|\mathbf{B}|\sin\theta_{\mathbf{vB}}}, \quad (1.53)$$

where $\theta_{\mathbf{vB}}$ is the angle between \mathbf{v} and \mathbf{B} . The numerator of (1.53) is recognized as the magnitude of the momentum $|\mathbf{P}|$. Some further rearrangement yields

$$|\mathbf{P}| = q|\mathbf{B}|R\sin\theta_{\mathbf{vB}}, \quad (1.54)$$

and thus measuring the direction and radius of curvature inside the field provides the charge and momentum, respectively, as desired.

1.2.2.4 Off Axis pi-zero detector (PØD)

The PØD is the primary detector used a neutrino target in this thesis. It is a plastic scintillator based tracking calorimeter inside the ND280 magnet region. It is designed to measure the neutral current (NC) process $\nu_\mu + N \rightarrow \nu_\mu + N + \pi^0 + X$ on water where N is a nucleus and X is any set of final state particles. NC π^0 was expected to be a significant background in the ν_e appearance search in the likelihood that $\theta_{13} \approx 0$. The PØD is a modifiable detector which can be filled or drained of water during data taking, enabling the determination of water target (WT) cross sections by comparing water-in data with water-out data.

A representation of the PØD is shown in Figure 1.24 on page 39. The active detector components are very similar to INGRID's design where scintillation light is captured by a WSF and counted by a MPPC. Each bar is triangular in shape as shown in Figure 1.25 on page 40. A plane of 134 horizontal and 129 vertical bar together to form a PØD module (PØDule) as shown in 1.24b. The PØD dimensions are $2.298 \times 2.468 \times 2.350\text{m}^3$, in XYZ respectively, with a total mass of ~ 1900 kg of water and 3570 kg of other material. The total mass of the PØD is approximately 15,800 kg when the bags are full of water. PØDules are

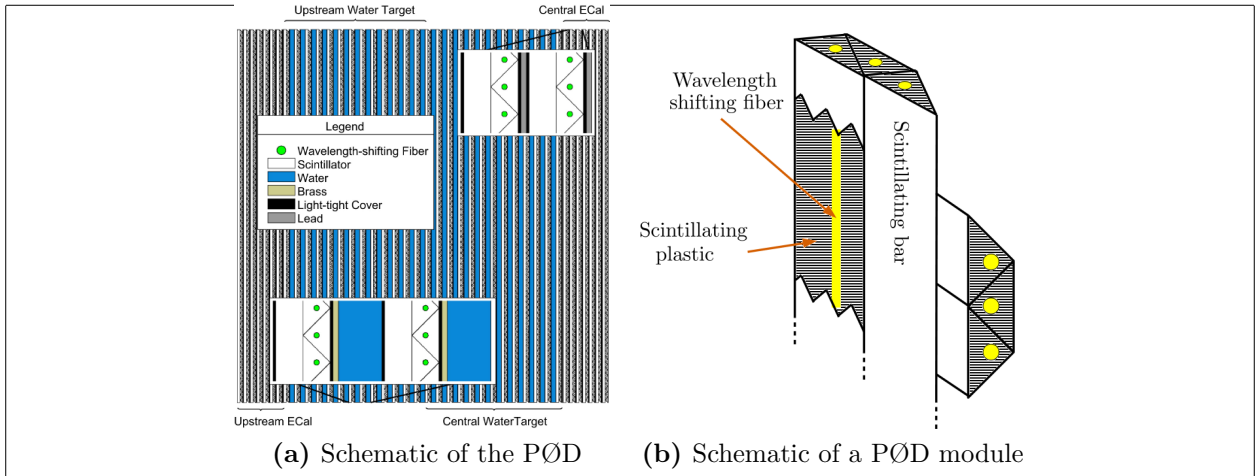


Figure 1.24: Schematics of the PØD. Left: insets detail the Water Target and ECal layers. Right: A view of a PØD module illustrating the orthogonal layout of the scintillating planes. Both: the neutrino beam is coming from the left.

Element	Symbol	Fraction [%]
Carbon	C	45.0
Oxygen	O	29.9
Copper	Cu	14.3
Hydrogen	H	8.0
Zinc	Zn	1.6
Chlorine	Cl	1.1
Titanium	Ti	0.1

Table 1.3: Elemental composition of PØD water target region. The table is sorted from top to bottom by fraction of mass. This table was originally produced in Reference [5]

arranged into three primary regions. The water target (WT) region contains 26 PØDules interleaved between bags of water 2.8 cm thick when filled and 1.3 mm thick brass sheets designed to help contain π^0 decay photons. The last two regions are the upstream ECal (USECal) central ECal (CECal). Each ECal region contains 7 PØDules with steel sheets clad with lead between them [5]. An elemental composition of the WT is shown in Table 1.3 on page 39.

The readout electronics for the PØD is based on the Trip-T application specific integrated circuit (ASIC) shared among the SMRD, ECals, and INGRID. Signals from 64 MPPCs are

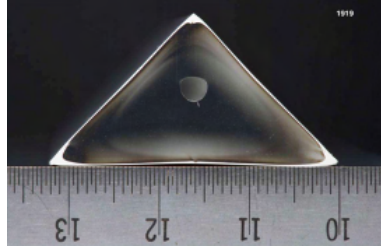


Figure 1.25: A cross section of a PØD scintillating bar. The base and height is 33 mm long and 17 mm high. The wavelength shifting fiber is inserted in the bored hole which is half-way between the base and tip.

routed to Trip-T front end boards (TFB) that each house 4 Trip-T ASICs. Each Trip-T collects the MPPC charge in 23 programmable integration cycles.

The TFB are readout to back-end electronics which control the TFBs and synchronize clocks. A total of six readout merger module (RMM) electronics receive TFB the data and control each TFB ASIC. RMM timing are synchronized with a cosmic trigger module and a slave clock module (SCM), of which both are synchronized with a master clock module from the beamline. Synchronizing the RMMs with the SCM allows for the Trip-T ASIC integration windows to match with the beam. The RMMs are responsible for distributing the TFB data to the data acquisition (DAQ) system for storage.

The ND280 DAQ consists of a MIDAS framework to monitor and control data collection. The primary client of the DAQ is to merge data and package it for long term storage. In parallel to it is the Global Slow Control (GSC) system which measures temperatures, voltages, and other physical quantities. Together the DAQ and GSC help scientists consistently produce high quality data and maintain the overall stability of the detector.

1.2.2.5 Off Axis Time Projection Chamber (TPC)

The ND280 TPC is designed to provide momenta measurements of charged particle tracks as discussed above, high resolution particle counting capabilities, and particle identification based on energy deposition. The latter most aspect is not utilized in this thesis. The TPC is divided into three volumes separated by the two FGD volumes. Each TPC volume

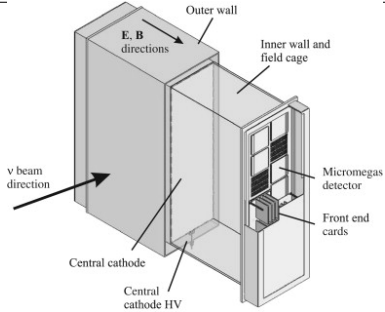


Figure 1.26: Cut-away drawing of a TPC volume in ND280 [1].

($2.3 \times 2.4 \times 1.0 \text{ m}^3$) consists of an inner box that holds an argon-based gas and an outer box that holds an insulating CO₂ gas. The inner gas mixture is 3000 L of Ar:CF₄:iC₄H₁₀ (95:3:2) gas. It was selected for its high speed, low diffusion, and good performance with the micromegas [1]. A simplified schematic of the TPC is shown in Figure 1.26 on page 41.

As charged particles traverse the inner TPC volume, they create ionization electrons in the gas which drift towards readout planes away from a central cathode. The electron drift acceleration is rapid due to the strong 5 kV/cm electric field present. Drift electrons are multiplied and sampled by micromega detectors that line the sides of the TPC, providing nearly 3 m² of active surface coverage. Arrival times of the electrons provide timing information to give a full three dimensional portrait of the events.

1.2.2.6 Track Reconstruction in ND280

The goal of track reconstruction software is to capture the shape and history of energy deposited in the detector. Since ND280 is collection of different technologies, highly specific algorithms and models are used to identify track-like patterns. Since this analysis uses neutrino events incident in the PØD and cross into the TPC, an unified and coherent reconstruction model. A reconstruction package called “Global” is designed to combine all ND280 information for this purpose.

For PØD tracks,

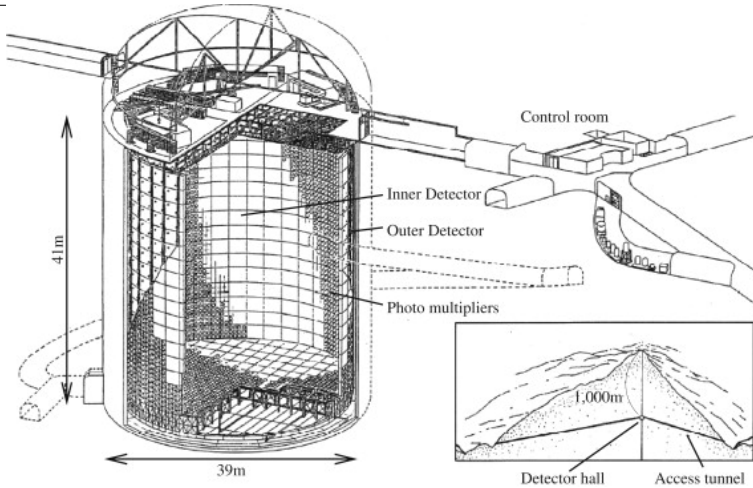


Figure 1.27: Diagram of the Super-Kamiokande detector consisting mainly of the inner and outer detector segments. The boundary between the two segments is cylindrical scaffolding used to mount photomultiplier tubes and optically isolate the segments.

1.2.3 Neutrino Far Detector: Super-Kamiokande

The Super-Kamioka neutrino detection experiment (Super-Kamiokande) is the dedicated far detector for the T2K experiment. Sitting at 295 km away from the neutrino source with a 1 km overburden, it is well designed to detect the elusive neutrino. Containing about 50 kt of pure water, is it lined with PMTs in both an inner and veto outer detector as shown in Figure 1.27 on page 42.

When charged particles travel through the water, a Cherenkov radiation cone is produced. The sharpness of the cone edge is an unique ID for the particle species that produced it. An electron produces a fuzzy edge since it experiences many large multiple scatterings off the water molecules. A muon on the other hand produces a sharp edge since it is much more massive and thus less perturbed by the water molecules. Both types of events are shown in Figure 1.28 on page 43. By determining the particle that produced it and isolating the event during the T2K beam, the neutrino flavor is deduced.

While events from SK are not used in this analysis, the goal is to try to improve T2K's parameters which depend on comparing the Near Detector neutrino measurements to the

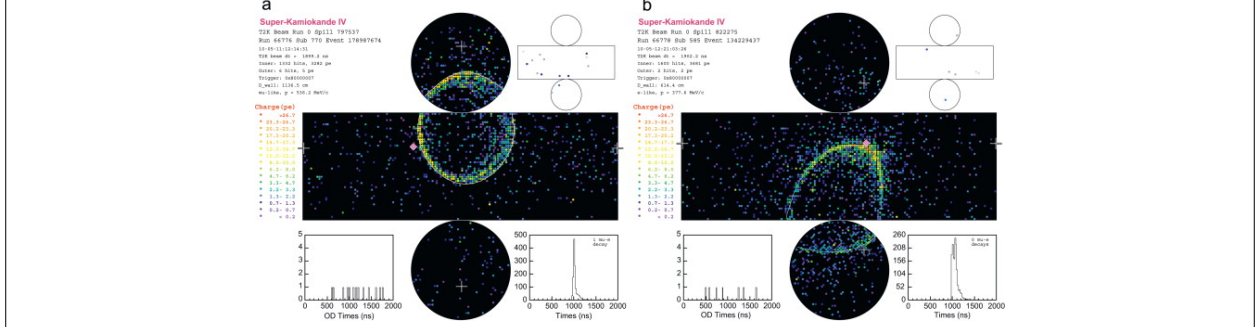


Figure 1.28: Representative T2K events in Super-Kamiokande for (a) a muon-like ring and (b) an electron-like ring. Both figures show Super-Kamiokande unrolled onto a plane with each colored point representing a PMT. The color of each PMT corresponds to the amount of charge collected. In upper right corner shows the same unrolled hit map for the veto outer detector. White crosses indicate the location of the reconstructed vertex. A solid diamond marks the location where a ray parallel to the beam would intersect the detector wall starting from the vertex.

Far Detector neutrino measurements. Therefore having some background on the oscillation analysis will illustrate ND280's utility and discussed in the next section.

1.2.4 ND Constraint

As started before, the primary goals of T2K are measure to measure the oscillation parameters θ_{13} , θ_{23} , and Δm_{23}^2 . This is performed by fitting the oscillation parameters to the number of observed flavored neutrinos at SK. The number of reconstructed neutrino events of flavor α , N_{ν_α} , observed is

$$N_{\nu_\alpha} = B + S_{\nu_\alpha} \quad (1.55)$$

where B are all misidentified ν_α events and S_{ν_α} is the number of true events. The expected rate given by

$$S_{\nu_\alpha} = \sum_{\lambda=e,\mu} \left[\mathcal{P}_{\nu_\lambda \rightarrow \nu_\alpha} (E_\nu; \vec{\sigma}) \right] \times \sum_t \left[\sigma_{\nu_\alpha}^t (E_\nu) \cdot t_N \right] \times \Phi_{\nu_\alpha} (E_\nu) \times \epsilon (p_\alpha, \theta_\alpha), \quad (1.56)$$

where $\vec{\sigma}$ is a vector of the oscillation parameters from (1.38), $\sigma_{\nu_\alpha}^t$ is the cross section for ν_α on target t , t_N is the number of targets of type t , Φ_{ν_α} is the flux of neutrinos, and

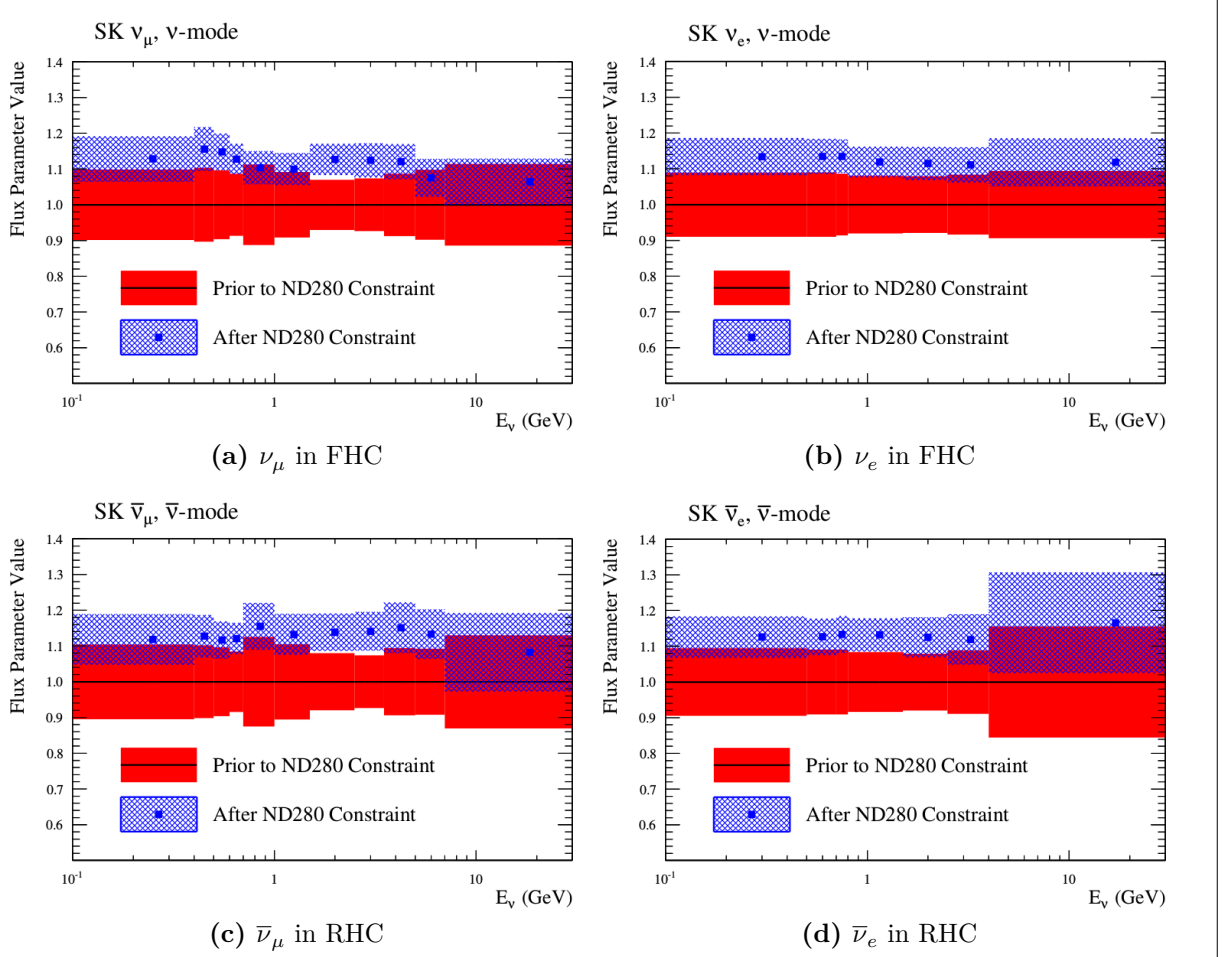


Figure 1.29: Predicted and best fit measurements for the SK flux. The horizontal axes are the neutrino energy and the vertical axes are the fractional change in the flux normalization. These figures were taken from the 2017 T2K oscillation analysis [4]. A value 1.1 corresponds to a 10% increase in the number of predicted events.

$\epsilon(p_\alpha, \cos \theta_\alpha)$ is the efficiency of reconstructing and correctly categorizing the event as a function of momentum p and angle θ .

Having a large, sensitive off-axis ND like ND280 provides critical constraints to the neutrino flux in the oscillation analysis. This includes the oscillation channel $\nu_\mu \rightarrow \nu_e$, but also the intrinsic $(\bar{\nu}_e)$ background in the T2K beam. These neutrinos interact the same way an oscillated neutrino would at SK. Without ND280, the fractional uncertainty on the flux rate is about $\sim 10\%$ per energy bin. These constraints are obtained from MUMON discussed above and the NA61/SHINE experiment [9]. Adding the ND constraint reduces the uncertainty to about $\sim 5\%$ as seen in fig. 1.29.

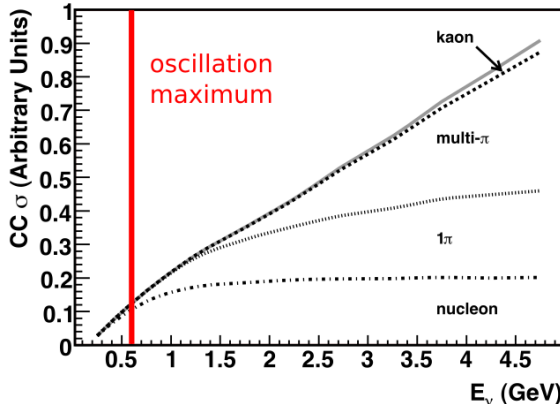


Figure 1.30: Predicted CC inclusive scattering cross section at T2K relevant energies. Only the most common final state modes are shown. A thick, red line indicates the T2K ν_e appearance probability maximum. For CCQE-like interactions, they usually include the emission of one or more nucleons. Resonance states and DIS interactions produce 1π , $N\pi$ (multi- π) and kaon final states as well. Combined, the inclusive cross section increases linearly with energy. This image was edited and originally produced by Formaggio and Zeller [25].

T2K uses the NEUT¹¹ program library to simulate neutrino interactions with nucleons and the nucleus [29]. It was originally designed to simulate atmospheric neutrinos for the Kamioka Nucleon Decay Experiment (Kamiokande). Included in NEUT are numerous models for neutrino interactions on matter and intra-medium hadron transport within the nucleus.

Using the ND280 constraint can tune the NEUT cross section model to best match the T2K data. The canonical T2K cross section model in NEUT is problematic due to model deficiencies to accurately predict the neutrino energy. The models implemented in NEUT, while being well studied in previous neutrino-nuclear Physics experiments, are known as effective models in T2K.

1.3 Summary

The Neutrino is an elusive particle to detect. The relatively new oscillation phenomenon has opened up the possibility of exploring fundamental questions of the Universe like CP

¹¹NEUT is neither an initialism nor acronym

violation. In the T2K experiment, some of the uncertainties associated with neutrino oscillations are being explored. To facilitate these goals, constraining all forms of uncertainty in neutrino-nuclear interactions and flux help improve its sensitivity to the oscillation predictions.

This thesis is presented in the following order. First is the ND280 constraint on the flux and cross section models using the BANFF maximum likelihood fit. Next is the description of the analysis samples that are used in the BANFF fit. With the samples defined, the parameterization of the fit bins and penalty terms are defined for this analysis. This is followed by the validation of the BANFF fit in a few scenarios. Then the BANFF postfit results will be analyzed in relation to previous analyses. The final chapter is a discussion of the results and prospects for the future.

Chapter 2

BANFF Likelihood

The BANFF likelihood maximization procedure is a binned likelihood maximization fitting of the ND280 data. This is separate from the fitting the Super-Kamiokande (SK) data. In a joint fit, the measurements from both detectors are considered along with their respective nuisance parameters. This approach is more computationally expensive since the time to perform a fit increases non-linearly with increasing the number of fit parameters. However it is developed in an alternate method called the Markov Chain Monte Carlo analysis (MaCh3) and this will not be explained here. The BANFF likelihood maximization, hitherto referred to as the “BANFF-fit”, includes nuisance parameters that affect the measurement of the oscillation parameters, but are not physics goals of the T2K experiment. The BANFF-fit parameters and their respective covariances are then used as inputs in the oscillation analysis. This “divide-and-conquer” approach allows for more rapidly completed studies on the effects of model parameters and biases present. Also this approach should provide the same result with a joint ND280 and SK analysis as is performed in MaCh3. However, information encoded in the ND280 measurements for shared nuisance parameters like the neutrino flux is inevitably lost in the BANFF-fit.

The modern BANFF-fit likelihood is described in detail in detail in [Insert PRD instead](#) TN-220 [28]. It uses a frequentist approach to find the best nuisance parameter set to maximize a

binned likelihood. Subsequent updates to the BANFF-fit have increased the sample sizes and systematic parameterizations.

2.0.1 Motivation

Curve fitting is commonly found in the particle physics community literature due to the need to compare two models or constrain unknown model parameters using one or more histograms. For the first case, this involves two competing models, H_0 and H_1 , in order to establish if the data supports new Physics (H_1) not predicted in the Standard Model (H_0). The second case finds the “best” set of the model predictions, θ , that match the data as is the case for the BANFF-fit. In both cases, chi-squared tests are performed to provide goodness of fit, parameter estimation (also referred to as “best fit parameters”), and error/confidence estimation.

2.0.2 Introduction to Conditional PDFs and Likelihoods

Consider the problem of extracting physics parameters \vec{y} given some data vector \vec{N} . The conditional probability density function (PDF) \mathcal{P} to measure these parameters is given as

$$\mathcal{P}(\vec{y}|\vec{N}) = \frac{\mathcal{L}(\vec{N}|\vec{y})\mathcal{P}(\vec{y})}{\int \mathcal{L}(\vec{N}|\vec{x})\mathcal{P}(\vec{x})d\vec{x}}, \quad (2.1)$$

where anything right of a vertical line represents a condition on the probability, $\mathcal{L}(\vec{N}|\vec{y})$ is the likelihood of the model with parameters \vec{y} , $\mathcal{P}(\vec{y})$ is the probability for the model, and the denominator is the normalization over all possible constraints on the observations. A frequentist interpretation of a PDF is a proportion of outcomes of repeated trials or experiments. A likelihood function is an expression of the probability of observing data as a function of the model parameters in their appropriate ranges.

One arrives at (2.1) by using the definition of compound probabilities

$$\mathcal{P}(A, B) = \mathcal{P}(B|A)\mathcal{P}(A) \quad (2.2)$$

to evaluate $\mathcal{P}(\vec{y}|\vec{N})$ as

$$\mathcal{P}\left(\underbrace{\vec{y}}_B \middle| \underbrace{\vec{N}}_A\right) = \frac{\mathcal{P}(\vec{N}, \vec{y})}{\mathcal{P}(\vec{N})} \quad (2.3)$$

with the denominator here is recognized as the normalization of the PDF. The compound PDF $\mathcal{P}(\vec{N}, \vec{y})$ can expanded using Bayes' theorem which states

$$\mathcal{P}(A|B)\mathcal{P}(B) = \mathcal{P}(B|A)\mathcal{P}(A), \quad (2.4)$$

and combined with (2.2) yielding

$$\mathcal{P}\left(\underbrace{\vec{N}}_A, \underbrace{\vec{y}}_B\right) = \mathcal{P}(\vec{N}|\vec{y}) \times \mathcal{P}(\vec{y}), \quad (2.5)$$

where the PDFs to the left and right of the \times operator are recognized as the likelihoods and priors, respectively. Combining resulting in (2.3) and (2.5) reproduces the original expression of (2.1).

2.0.3 BANFF Fit Test Statistic

For the BANFF fit, one considers the problem of trying to maximize the agreement between measured and predicted data histograms. This is equivalent to maximizing a binned likelihood function \mathcal{L} of the data given the a set of parameters that predict the measured rate. The use of likelihood functions in fits to histogram is explained further in reference [13] and the PDG review on Statistics. By invoking Wilks' theorem, also known as the likelihood ratio theorem, the likelihood maximization procedure is converted into a minimization problem involving a test statistic denoted as a chi-squared. Below is an explanation of the BANFF test statistic, $\Delta\chi^2$, and its systematic model terms.

Consider many binned samples that select different charged current topologies. A convenient choice of observables for all the samples are the outgoing charged lepton l momentum P_l and angle $\cos \theta_l$ as measured in ND280. Much of this is also documented in TN-220 [28] where additional details can be found. For each $(P_l, \cos \theta_l)$ analysis bin $i = 1, 2, \dots, M-1, M$, the likelihood is given by

$$\mathcal{L}(\vec{N}^d | \vec{N}^p) = \left(\prod_{i=1}^M \left(\vec{N}_i^p \right)^{\vec{N}_i^d} \frac{e^{-\vec{N}_i^p}}{\vec{N}_i^d!} \right) \quad (2.6)$$

where \vec{N}_i^d is the number of observed data events in the i th bin and \vec{N}_i^p is the number of predicted events as a function of nuisance parameters in the i th bin. One recognizes the likelihood function in (2.6) as a product of Poisson distributions, since this is counting data measured in M analysis bins. The sets of dependent nuisance parameters, also sometimes called systematics, that affect the predicted event rate are

- cross section physics models, labeled as “xsec”,
- neutrino flux, and
- detector biases and inefficiencies.

Given these three sets of systematics, the number of predicted CC events from any neutrino flavor ν_l at ND280 is calculated using the general formula

$$N_{\nu_l} = \underbrace{\Phi_{\nu_l}}_{\text{Flux per area}} \left[\sum_t \underbrace{(\sigma_{\nu_l}^t M_t)}_{\text{Effective area}} \right] \underbrace{\epsilon_{\nu_l}}_{\text{Efficiency}} , \quad (2.7)$$

where Φ_{ν_l} is the flux of l flavor neutrinos, $\sigma_{\nu_l}^t$ is the cross section of the interaction for neutrino flavor l on target t , M_t is the number of t targets, and ϵ_{ν_l} is the total efficiency to reconstruct and properly identify the event as ν_l CC interactions. Since the cross section is a measure of interaction probability in units of area, multiplication of M_t represents the effective cross sectional area of material t in the detector. Each term in (2.7) is modeled carefully and the

efficiency term is estimated using Monte Carlo (MC) simulations and control samples. The number of predicted events from the MC for a given analysis bin i is given by

$$\vec{N}_i^p(\vec{b}, \vec{x}, \vec{d}) = w_i^{\text{POT}} (\vec{d})_i^{\text{Det}} \sum_{j=1}^{N_i^{\text{MC}}} \left[\sum_{k=1}^{N^{\text{Flux}}} \left(\delta_{j,k}^{\text{Flux}} (\vec{b})_k^{\text{Flux}} \right) \prod_{l=1}^{N^{\text{xSyst}}} w_{j,l}((\vec{x})_l^{\text{xsec}}) \right]. \quad (2.8)$$

Here w_i^{POT} is the protons on target (POT) weight for the i th analysis which normalizes the MC statistics to expected data statistics. To account for the detector inefficiencies, the $(\vec{d})_i^{\text{Det}}$ parameters are normalization parameters that vary the total number of predicted events in the i th bin. Each $(\vec{d})_i^{\text{Det}}$ is determined prior to the fit by surveying over a large number of toy experiments with the detector systematics varied in each. The sum over $j = 1, 2, \dots, N_i^{\text{MC}} - 1, N_i^{\text{MC}}$ considers the contribution of all MC events in the i th analysis bin. The $(\vec{b})_k^{\text{Flux}}$ parameters, out of a total of N^{Flux} , are flux normalization systematics for each flux bin. Since the flux bins are categorized not only by neutrino energy, but also by flavor and horn current, the $\delta_{j,k}^{\text{Flux}}$ term in the sum over k selects the correct flux bin. The parameters $w_{j,l}$ are pre-calculated weights as a function for the l th cross section model, $(\vec{x})_l^{\text{xsec}}$, with a total of N^{xSyst} cross section model terms. Different t target materials have separate cross section parameters. Also the number of targets M_t can vary via detector systematics.

Using the likelihood ratio test theorem, a test statistic is defined as taking -2 times the natural logarithm of the ratio of predicted to observed likelihoods

$$\Delta\chi_{\text{LLR}}^2 = -2 \log \frac{\mathcal{L}(\vec{N}^d | \vec{N}^p)}{\mathcal{L}(\vec{N}^d | \vec{N}^d)}, \quad (2.9)$$

where this test statistic $\Delta\chi_{\text{LLR}}^2$ obeys a true chi-squared distribution for asymptotically large statistics and the likelihood functions are of the form (2.6). The denominator in (2.9) is the MC predicted probability which assumes the best maximum likelihood estimate is the number of observed events. Penalty terms from the cross section, flux, and detector

systematics are included in order to prevent overfitting of the data. The new test statistic for all of ND280, $\Delta\chi^2_{\text{ND280}}$, is given by

$$\begin{aligned}\Delta\chi^2_{\text{ND280}} &= \Delta\chi^2_{\text{LLR}} + \Delta\chi^2_{\text{xsec}} + \Delta\chi^2_{\text{Flux}} + \Delta\chi^2_{\text{Det}} \\ &\quad - 2 \left(\log \frac{\mathcal{L}(\vec{N}^d | \vec{N}^p)}{\mathcal{L}(\vec{N}^d | \vec{N}^d)} + \underbrace{\log \pi(\vec{x})}_{\text{xsec}} + \underbrace{\log \pi(\vec{b})}_{\text{Flux}} + \underbrace{\log \pi(\vec{d})}_{\text{Det}} \right),\end{aligned}\quad (2.10)$$

where each of the PDFs $\pi(\vec{y} = \vec{x}, \vec{b}, \vec{d})$ are assumed multivariate normal distributions

$$\pi(\vec{y}) = C_y e^{(-\frac{1}{2}\Delta\vec{y} \cdot V_y^{-1} \cdot \Delta\vec{y}^T)}, \quad (2.11)$$

$\Delta\vec{y}$ is a vector with the difference between the current/explored and nominal set of vector parameters \vec{y} , T corresponds to the transpose operator, and the normalization is given by

$$C_y = ((2\pi)^{k_y} \det(V_y))^{-\frac{1}{2}} \quad (2.12)$$

with V_y being the covariance matrix for a vector \vec{y} with k_y rows. The expanded form of the test statistic $\Delta\chi^2_{\text{ND280}}$ is given by

$$\begin{aligned}\Delta\chi^2_{\text{ND280}} &= 2 \sum_{i=1}^M \left[\vec{N}_i^p - \vec{N}_i^d + \vec{N}_i^d \log \left(\frac{\vec{N}_i^d}{\vec{N}_i^p} \right) \right] \\ &\quad + \Delta\vec{x} \cdot (V_x^{-1}) \cdot \Delta\vec{x}^T + \Delta\vec{b} \cdot (V_b^{-1}) \cdot \Delta\vec{b}^T + \Delta\vec{d} \cdot (V_d^{-1}) \cdot \Delta\vec{d}^T\end{aligned}\quad (2.13)$$

where the “ \cdot ” is the matrix multiplication operator. It must be stated that the test statistic (2.13) purposefully *excludes normalization terms*. The specific parameterization of the penalty terms in (2.13) will be further discussed in Chapter 4. Once the global minimum of the test statistic is found, the postfit covariance matrix V is calculated as the inverse of the Hessian matrix H

$$V_{i,j}^{-1}(\hat{\vec{y}}) = H_{i,j} = \left. \frac{\partial^2}{\partial y_i \partial y_j} (\Delta\chi^2_{\text{ND280}}) \right|_{\vec{y}=\hat{\vec{y}}} \quad (2.14)$$

where $y_i, y_j \in \vec{y}$ and $\hat{\vec{y}}$ is the maximum likelihood estimate for the parameters \vec{y} .

Chapter 3

The PØD Selections and Samples

This chapter describes the development of ν_μ and $\bar{\nu}_\mu$ CC inclusive selections in both FHC and RHC beam configuration for PØD-based analyses. These selections are the continuation of previous works that developed ν_μ CC inclusive selections between the PØD and the TPC. The first such analysis was the ν_μ CC inclusive cross-section using the previous ND280 simulation and reconstruction software called Production 5 [21]. That analysis relied on each sub-detector's reconstruction software and developed a track matching algorithm since the ND280 “Global” reconstruction matching was not available in that software production. Another cross section analysis measuring the cross section ratio of $\bar{\nu}_\mu/\nu_\mu$ also used this “pre-Global” technique with the modern T2K Production 6 software [5]. As the inter-detector matching reconstruction became available in Global, two cross section analyzes, ν_μ CC 0π [6] and $\bar{\nu}_\mu$ CC 0π [8, 14], were developed that also used the CC inclusive selection as pre-selection cuts. These pre-selection cuts are well validated and have published results as shown in Figure 3.1 on page 55. The selections described in this thesis also employ the same pre-selection cuts with the latest stable Global reconstruction software, Production 6. The next paragraph is a layout of the following topics.

The first topic is the event reconstruction using the “Global” reconstruction software. Next is the pre-selection cut flow. With the pre-selection cuts established, each of the three

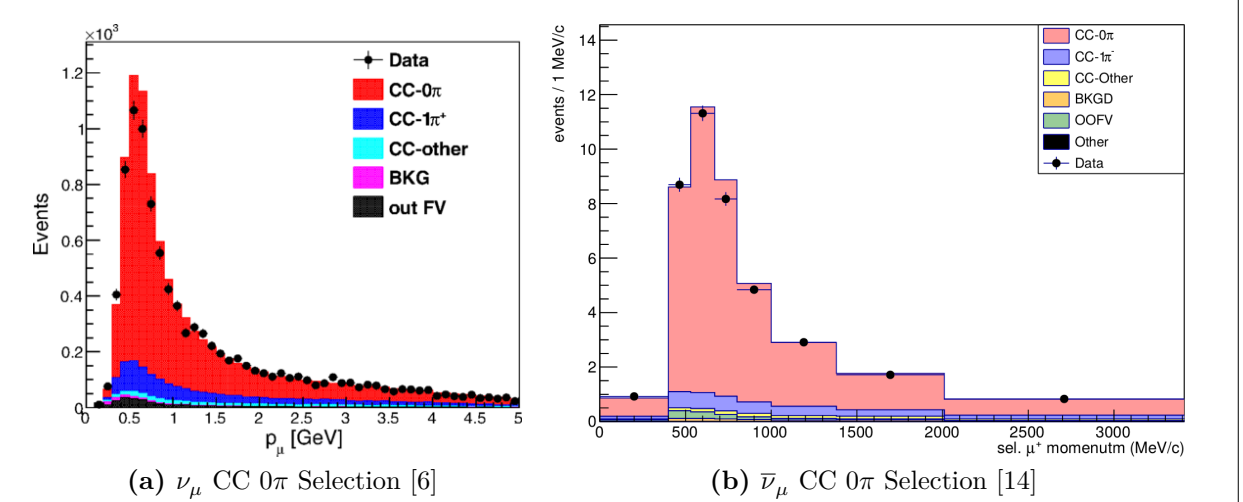


Figure 3.1: Data and MC distributions of the PØD water-in ν_μ and $\bar{\nu}_\mu$ CC 0π signal selections. They importantly share the same pre-selection cuts as this analysis. The plots have been normalized to data POT and are sorted into various truth topologies.

CC inclusive selection's cut flow is described. Concluding this section is a discussion of the three samples in the following order: ν_μ in FHC mode, $\bar{\nu}_\mu$ in RHC, and ν_μ background in RHC.

3.1 Global Reconstruction

The task of the Global reconstruction is to combine all the ND280 information into a combined reconstructed object. It was originally designed to analyze “CCQE-like” events in the Tracker, FGD+TPC, region and has been extended to operate with all of ND280. A brief description of the Global reconstruction is described below.

The Global reconstruction is a software package that attempts to recognize patterns of data to form tracks and find their common origin, or vertices, for those tracks. Particle shower reconstruction in Global will not be discussed in this thesis since no shower objects are considered. Each sub-detector reconstruction is run as the seed to Global’s track matching algorithms. This includes the PØD’s track-finding algorithms, which defines a PØD track as a sequence of nodes each at a single bar layer. To facilitate inter-detector matching, Global attempts to re-fit the PØD track using a Kalman filter [47]. The re-fit procedure

also corrects for particle energy loss as a function of length (dT/dx) and multiple scattering processes. A PØD vertex, which is the reconstructed location of the neutrino interaction, is then associated with the re-fit track using another Kalman filter algorithm. Matching tracks between the PØD and the TPC is done automatically in the ND280 Global fit.

3.2 PØD Selection Cuts

The selection of CC inclusive events use a series of cuts to select the primary lepton. The pre-selection cuts (“precuts”) are applied first to extract events that start in the PØD fiducial volume (FV). A minimum ionizing particle (MIP) is more likely to reach TPC1 from the PØD FV since the PØD is constructed out of heavy materials especially in the CECal. So the main track each selection is designed to select a muon.

This following sections will describe the precuts common to all CC inclusive selections and the branching of different cuts, after the precuts, to select the main track.

3.2.1 Precuts

The precuts were initially developed to select ν_μ CC inclusive using the PØD and TPC sub-detector reconstruction softwares separately [5,21]. They were then used with the Global reconstruction software for the ν_μ CC- 0π selection in the FHC beam configuration [6]. The description and sequence of the precuts is described below.

The following precuts are checked on the collected data from each Trip-T integration cycle as follows:

1. The event has a “good” data quality flag.
 - An event is rejected if any sub-detector or electronics in ND280 reported as “bad” during that bunch.
2. There is at least one (1) track reconstructed in TPC1.

- There are no restrictions on the number of tracks fully contained in the PØD or exiting into other sub-detectors.
3. The track in the TPC must have more than 18 nodes.
- The TPC reconstruction gathers vertical and horizontal hits into clusters of hits. The charge distribution of the cluster is used to get a vertical (horizontal) position that is more accurate than the individual readout pads. A node is constructed out of each cluster with associated track state information. The set of nodes are used to fit a helix shaped track.
4. The reconstructed vertex is within the PØD water target (WT) FV.
- The PØD FV is defined to include as much as the WT regions as possible. Its X and Y borders are 25 cm away from the PØDule edges while its Z borders intersect the last and first half downstream PØDule in the USECal and CECal, respectively. The enumerated volume edges are shown in Table 3.1 on page 58. This volume, while used for track-based analyzes in the past, was optimized for π^0 and ν_e analyses.
5. All tracks that enter the TPC pass the veto cut
- An event is rejected if any PØD track enters the TPC from outside the “corridor” volume. This cut was designed to eliminate broken tracks between the PØD and TPC1 the pre-Global separate sub-detector reconstruction was used [15]. In practice, this cut ensures that Global tracks entering the TPC are away from its X and Y edges. The corridor definition is the same as defined in the pre-published $\bar{\nu}_\mu/\nu_\mu$ cross section ratio analysis [16] and shown in Table 3.1 on page 58.

PØD WT FV			Corridor Volume		
-836	$< X <$	764	-988	$< X <$	910
-871	$< Y <$	869	-1020	$< Y <$	1010
-2969	$< Z <$	1264	-3139	$< Z <$	-900

Table 3.1: The PØD WT FV (left) and veto corridor volume (right) in the ND280 coordinate system. The corridor spans from the 5th (8th) to 40th (80th) PØDule (scintillator layer). All the units are given in millimeters.

After passing all the precuts, a single, global track, which is observed in TPC1, is assigned as the lepton candidate or “main track” of a selection.

The momentum of the main track, P , is sum of its momentum in the TPC, P_{TPC} , with the estimate momentum lost in the PØD, $\Delta P_{\text{PØD}}$

$$P = P_{\text{TPC}} + \Delta P_{\text{PØD}}. \quad (3.1)$$

Momentum lost in the PØD is estimated by first summing the total energy loss, ΔT , along the track path \mathcal{C}

$$\Delta T = \int_{\mathcal{C}} \left(\frac{dT}{dx} \right) dx. \quad (3.2)$$

Using the chain rule, we can convert the energy loss function, dT/dx , into momentum loss

$$\begin{aligned} \frac{dT}{dx} &= \left(\frac{dT}{dP} \right) \left(\frac{dP}{dx} \right) \\ &= \left(\frac{Pc^2}{E} \right) \left(\frac{dP}{dx} \right) \\ &= \beta c \left(\frac{dP}{dx} \right), \end{aligned} \quad (3.3)$$

where β is the changing particle velocity as a ratio of the speed of light c . The fundamental theorem of Calculus permits us to write the energy loss as a momentum loss along the track’s

path \mathcal{C} as

$$\Delta P_{\text{P}\emptyset\text{D}} = \int_{\mathcal{C}} \left(\frac{dP}{dx} \right) dx = \frac{1}{c} \int_{\mathcal{C}} \left[\left(\frac{dT}{dx} \right) \frac{1}{\beta(x)} \right] dx. \quad (3.4)$$

Since the reconstructed track's path \mathcal{C} is not infinitesimally precise due to inherent detector resolution, we must replace the integral with a sum and differential $dx \rightarrow \Delta x$. We then arrive at the expression of the momentum loss estimate in the PØD as

$$P = P_{\text{TPC}} + \frac{1}{c} \sum_t \left[\left(\frac{dT}{dx} \right) \left(\frac{\Delta x}{\beta(x)} \right) \right]_t. \quad (3.5)$$

For most tracks entering the TPC, they will be highly relativistic in the PØD ($\beta \approx 1$), and (3.5) simplifies to

$$P = P_{\text{TPC}} + \frac{1}{c} \sum_t \left[\left(\frac{dT}{dx} \right) \Delta x \right]_t \quad (3.6)$$

The next sections describe the selection cuts, first in FHC mode and then RHC mode.

3.2.2 The ν_μ CC Inclusive in FHC Cut

- The highest momentum negatively charged track (HMNT) is the lepton candidate

As discussed in Section section 3.2.1 on page 56, this selection is the basis for the PØD ν_μ CC-0 π analysis [6]. In FHC mode, the vast majority of neutrino interactions are ν_μ CC events producing an outgoing, negatively charged muon. So if there is no negatively charged track in the TPC, the event is rejected.

3.2.3 The $\bar{\nu}_\mu$ CC Inclusive in RHC Cuts

- The highest momentum positively charged track (HMPT) is the lepton candidate
- The HMPT must be the highest momentum track (HMT)

In RHC, the majority of neutrinos in the beam is $\bar{\nu}_\mu$ since the horn focuses negatively charged pions. To select $\bar{\nu}_\mu$ CC interaction events, the lepton candidate is the HMPT in the TPC.

The event is rejected if there is no positively charged track. However, since the RHC mode beam is not as $\bar{\nu}_\mu$ pure as the FHC beam, another cut was added to reduce this effect.

Since RHC neutrino beam can be described as a $\bar{\nu}_\mu$ -enhanced beam, the HMPT must also be the HMT due to the significant “wrong-sign” ν_μ background. This effect is two fold due to the nature of the neutrino source and the cross section between neutrinos and antineutrinos. Firstly the neutrino flux is larger in RHC mode due to neutrino production at the target. The source of neutrinos are from mainly positively charged pions and kaons decays produced proton collisions on a graphite target. This method is more likely to produce positively charged pions in the target than negatively charged one. While the horns are designed to select the negatively charged pions in RHC mode, the excess amount of positively charged pions will penetrate this filter. Therefore there are many more $\pi^+ \rightarrow \mu^+ + \nu_\mu$ decays in RHC compared to FHC mode. Secondly, antineutrino interactions on matter are suppressed compared to neutrinos due to helicity considerations as explained in Section 1.1.1.3.

3.2.4 The ν_μ Background CC Inclusive in RHC Cuts

- The highest momentum negative track (HMNT) is the lepton candidate
- The HMNT must be the highest momentum track (HMT)

As discussed in section 3.2.3 on the preceding page, the RHC neutrino beam has a significant wrong-sign ν_μ background. The selection of the HMNT is designed to select the negatively charged muons. To prevent selecting the antineutrino events, the HMNT must also be the HMT. The event is rejected if there is no negatively charged track. If there are both positively and negatively charged tracks, the HMT cut discriminates if the event originates from a ν_μ or $\bar{\nu}_\mu$.

Run period	Horn current [kA]	PØD status	Data POT ($\times 10^{20}$)	MC POT ($\times 10^{20}$)
2	+250	Water	0.4339	12.03
		Air	0.3591	9.239
3b	+205		0.2172	4.478
3c	+250		1.364	26.32
4			1.782	34.99
		Water	1.642	34.97
5c	-250		0.4346	22.77
6b		Air	1.288	14.17
6c			0.5058	5.275
6d			0.7753	6.884
6e			0.8479	8.594
7b		Water	2.436	33.70
8	+250		1.580	26.46
		Air	4.148	36.06
Sand	+250		-	11.19
Sand	-250		-	12.92
2, 3b, 3c, 4, 8		FHC	Air	7.872
2, 4, 8			Water	3.657
6b, 6c, 6d, 6e		RHC	Air	3.417
5c, 7b			Water	2.871
				56.48

Table 3.2: T2K MC and data POT divided by run periods. The bottom four rows are the aggregated periods grouped by horn current and PØD status which is how the data analysis is performed.

3.3 Selection Kinematics

This section examines the kinematics for each of selections while differentiating between water-in and water-out mode. The selection cuts were implemented in Psyche which is the software interface that BANFF uses to select events. The data sets used in this analysis are runs 2-8 in both PØD water-in and water-out (air) modes as shown in Table 3.2 on page 61. There will be no data events shown to prevent any potential biases that exist between the data and MC. Simulated events will be broken down into various true categories to understand selection kinematics, efficiencies, and purities.

True interactions for these selections are generally divided into four interactions classes:

- neutrino-induced CCQE (ν CCQE):
 - Only NEUT generated neutrino-induced CCQE event at the interaction vertex
- neutrino-induced non-CCQE (ν non-CCQE),
 - Any NEUT generated neutrino-induced CC and NC event *except* neutrino-induced CCQE at the interaction vertex
- antineutrino-induced CCQE ($\bar{\nu}$ CCQE)
 - Only NEUT generated antineutrino-induced CCQE event at the interaction vertex
- antineutrino-induced non-CCQE ($\bar{\nu}$ non-CCQE)
 - Any NEUT generated antineutrino-induced CC and NC event *except* antineutrino-induced CCQE at the interaction vertex

An enlarged legend of these four interaction classes used in this analysis is shown in Figure 3.2 on page 63. Out of fiducial volume (OOFV) events refer to neutrino and antineutrino interactions occurring in ND280, but not in the PØD water target (WT) fiducial volume (FV). Sand muons, similar to OOFV events, are any neutrino/antineutrino-induced interaction truly occurring in the sand surrounding the ND280 pit.

The non-CCQE category can be further divided among the dominant T2K CC and all NC interactions modes as enumerated in Table 3.3 on page 63 and Table 3.4 on page 64. For neutrino-based selections, the legend shown in Figure 3.4 on page 65 is also used to describe the neutrino-induced interaction purity of the selection. Similarly for antineutrino-based selections, the legend shown in Figure 3.5 on page 65 is used for the same purpose.

The true particle matched with the main track is also analyzed here as shown in Figure 3.3 on page 64. The ND280 MC uses the GEANT4 software toolkit [11] to simulate the passage of particles through matter. A GEANT4 particle is assigned to a reconstructed track if it contributed the most to the track's reconstructed hits. True particles include protons (p)

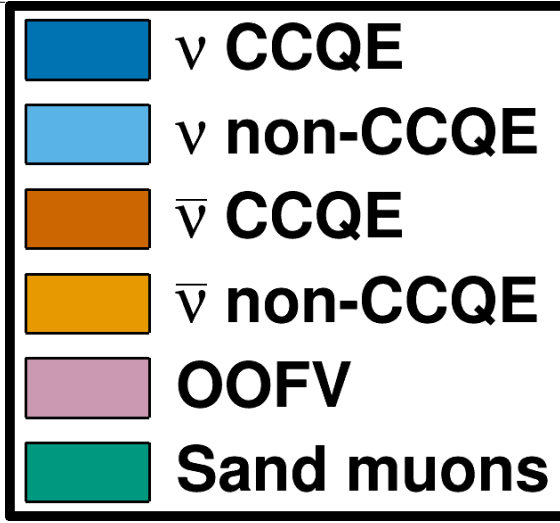


Figure 3.2: NEUT CCQE and non-CCQE interactions legend. The enumerated NEUT codes are given in Figure 3.4 on page 65 and Figure 3.5 on page 65.

Category	NEUT Codes
ν CCQE	1
ν 2p2h	2
ν CC-1 π	11 → 16
ν non-CCQE	
ν CC-N π	21
ν CC-DIS	26
ν CC-Other	17, 22, 23
ν NC	31 → 100
$\bar{\nu}$	-1 → -100
OOFV	-100 → 100
Sand muons	-100 → 100

Table 3.3: The expanded ν NEUT reactions table as shown in Figure 3.4 on page 65. An arrow indicates a sequence of integer steps from left to right of the arrow.

Category	NEUT Codes
$\bar{\nu}$ CCQE	-1
$\bar{\nu}$ 2p2h	-2
$\bar{\nu}$ CC-1 π	-11 → -16
$\bar{\nu}$ non-CCQE	$\bar{\nu}$ CC-N π
	-21
	$\bar{\nu}$ CC-DIS
	-26
	$\bar{\nu}$ CC-Other
	-17, -22, -23
	$\bar{\nu}$ NC
	-31 → -100
ν	1 → 100
OOFV	-100 → 100
Sand muons	-100 → 100

Table 3.4: The expanded $\bar{\nu}$ NEUT reactions table as shown in Figure 3.5 on page 65.

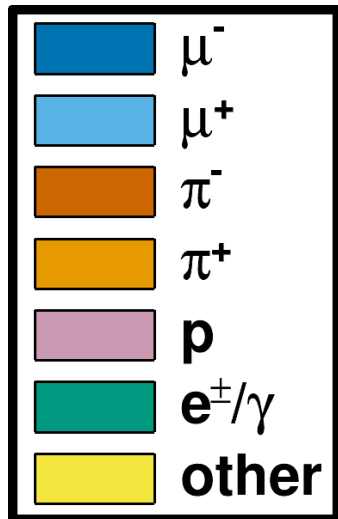


Figure 3.3: True particle selected legend

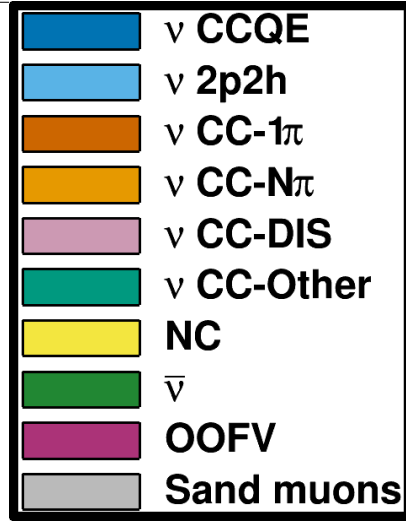


Figure 3.4: The NEUT neutrino interaction legend used in this analysis. The labels are enumerated in Table 3.3 on page 63.

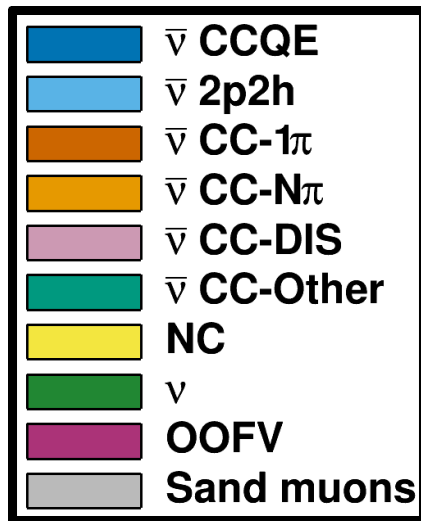


Figure 3.5: NEUT antineutrino interaction legend used in this analysis. The labels are enumerated in Table 3.4 on page 64.

and both negatively and positively charged muons (μ^\pm), pions (π^\pm), and electrons/positrons (e^\pm). In addition, any electron and positron generated from pair production are grouped together as “ e^\pm/γ ”. Particles that do not match any of these categories is labeled as “other”.

3.3.1 ν_μ in FHC CC 1-Track

This selection provides the CCQE-like samples in FHC mode. Figure 3.6 on page 67 and Figure 3.7 on page 68 displays the momentum and angular distributions that are inputs to BANFF. In the majority of cases, the lepton candidate is the true muon, making this a very pure ν_μ sample. Comparing between water-in and water-out modes, we see the reconstructed kinematics are nearly identical. Following this paragraph and the following sections, only the PØD water-in mode will be shown.

The underlying true kinematics of the interactions are shown in Figure 3.9 on page 69 which are of theoretical importance in the cross section and flux models. Using Figure 1.5 on page 12 as reference, the true neutrino energy $E_\nu = k_0$ and 4-momentum transfer $Q^2 = -q^2$. An interesting CCQE-like topology in this selection are 2p2h events. Interaction model uncertainties for 2p2h are quite large in T2K and are included the BANFF fit. Therefore these events could help reduce the 2p2h model uncertainties.

This selection contains a modest fraction of non-CCQE interactions. The largest contamination is 1π interactions, which can happen primarily for a couple of reasons. Firstly, when the final state pion is produced, it is subject to final state interactions (FSI) where a pion can be absorbed or scattered in the nucleus. Secondly, and more importantly, a pion might not be reconstructed as a track in the PØD if its energy is below reconstruction threshold. Together, the large 1π background affects the CC-0 π and CC-1 π model parameters in the BANFF fit.

We can examine the efficiencies and purities differentially for true ν_μ CCQE interactions in Figure 3.8 on page 69. The efficiency, ϵ , and purity, ρ , are defined as

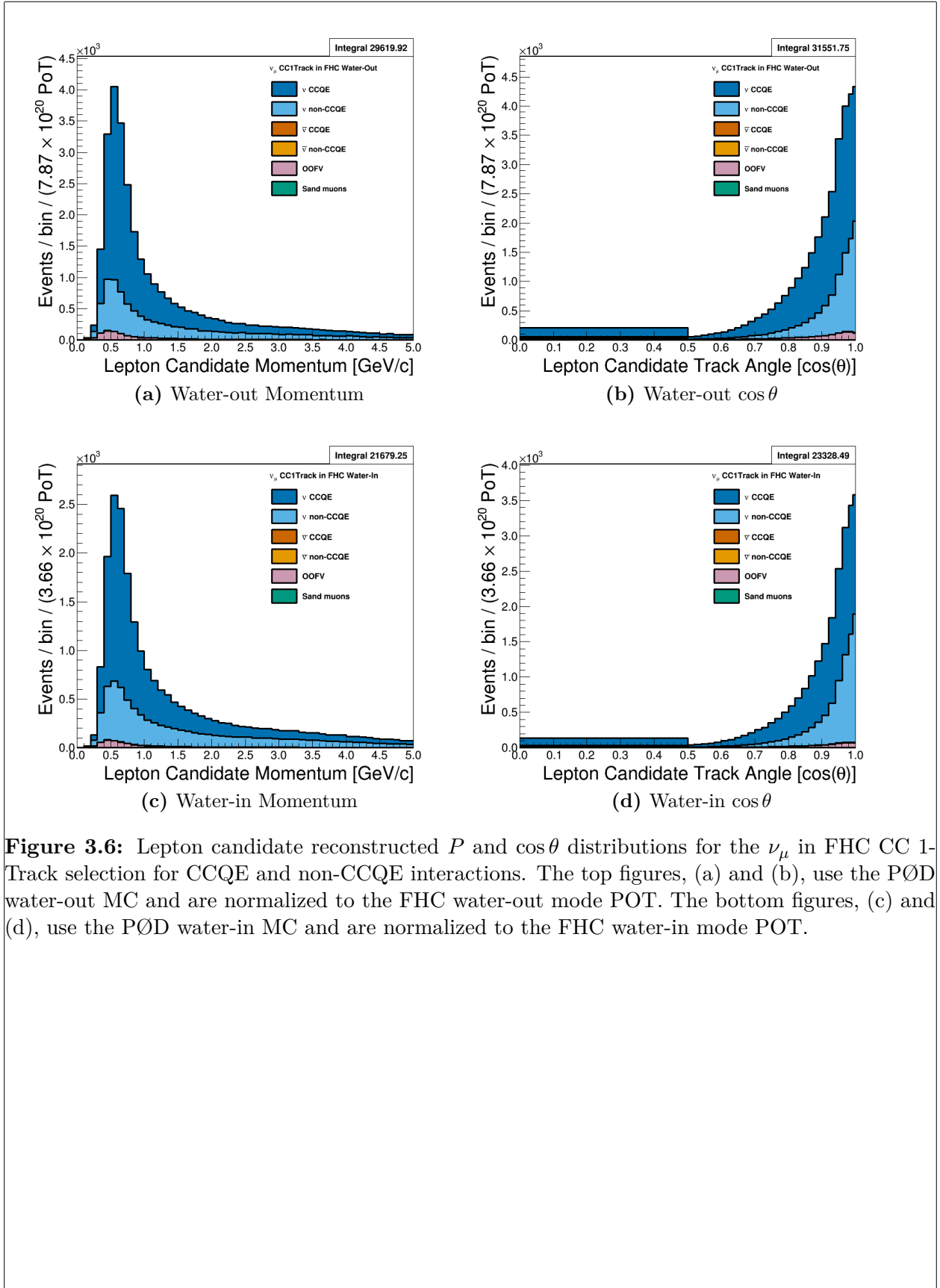


Figure 3.6: Lepton candidate reconstructed P and $\cos \theta$ distributions for the ν_μ in FHC CC 1-Track selection for CCQE and non-CCQE interactions. The top figures, (a) and (b), use the PØD water-out MC and are normalized to the FHC water-out mode POT. The bottom figures, (c) and (d), use the PØD water-in MC and are normalized to the FHC water-in mode POT.

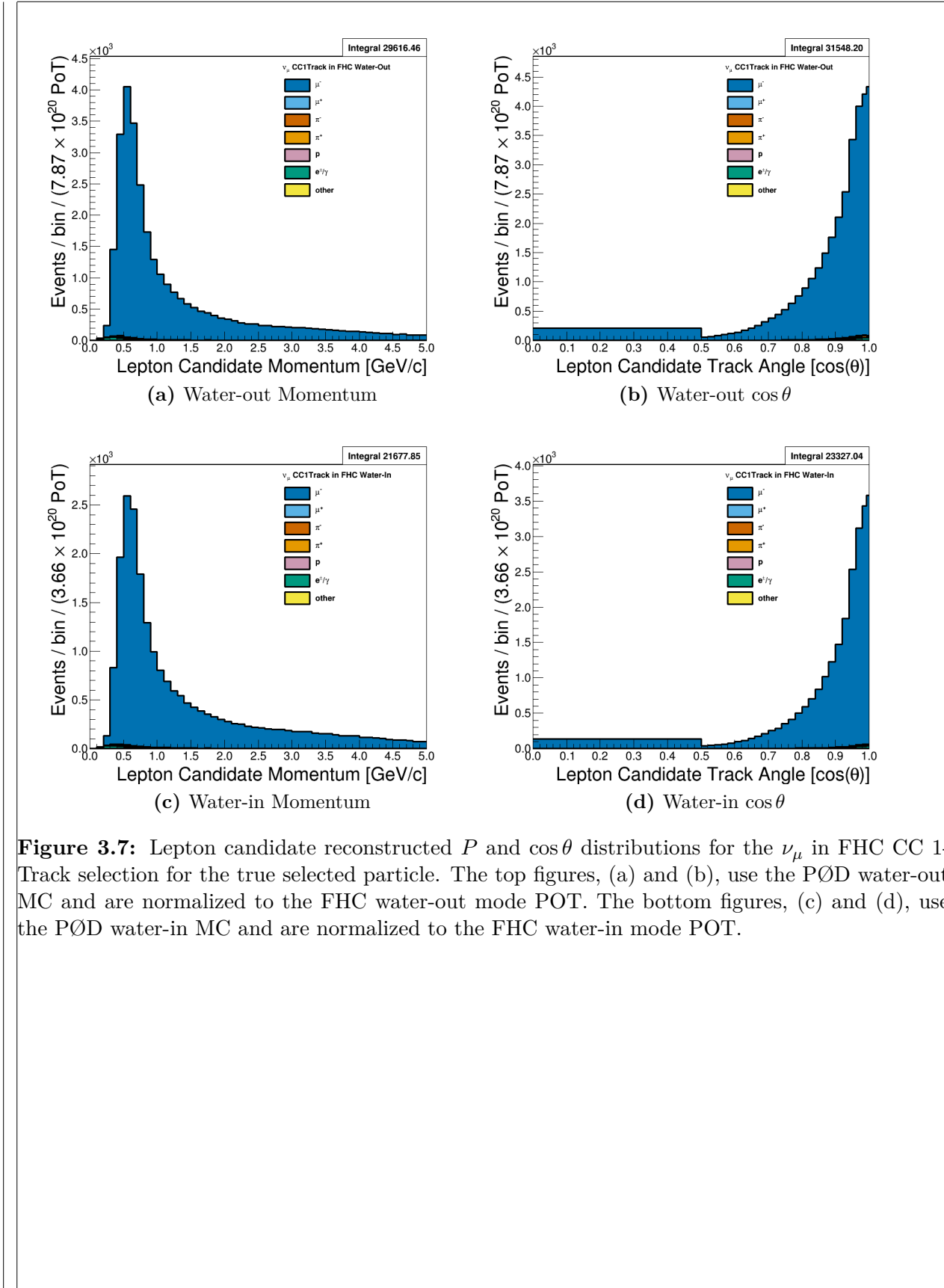


Figure 3.7: Lepton candidate reconstructed P and $\cos\theta$ distributions for the ν_μ in FHC CC 1-Track selection for the true selected particle. The top figures, (a) and (b), use the PØD water-out MC and are normalized to the FHC water-out mode POT. The bottom figures, (c) and (d), use the PØD water-in MC and are normalized to the FHC water-in mode POT.

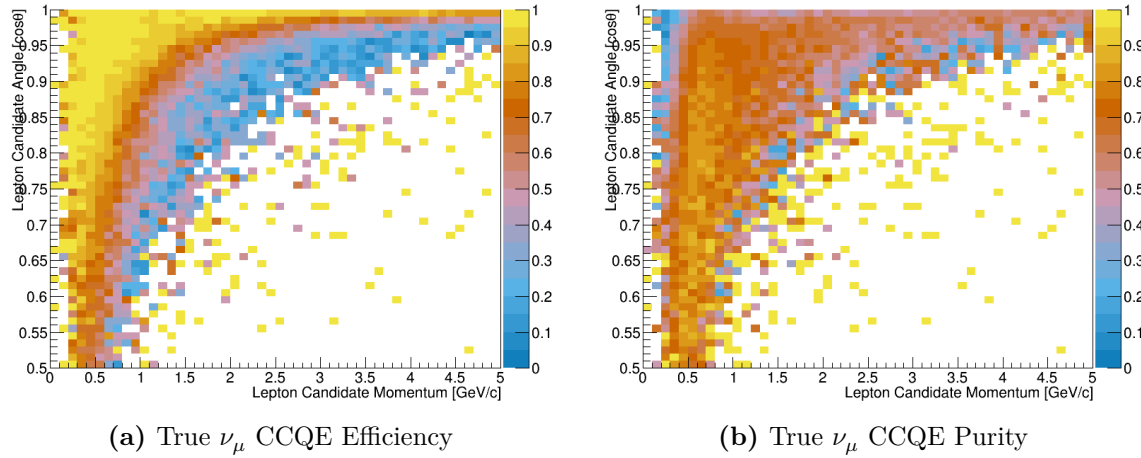


Figure 3.8: The efficiency and purity in reconstructed kinematics of ν_μ CCQE interactions in the ν_μ in FHC CC 1-Track selection. True events are defined as correctly matched μ^- tracks from ν_μ -induced CCQE interactions at the vertex .

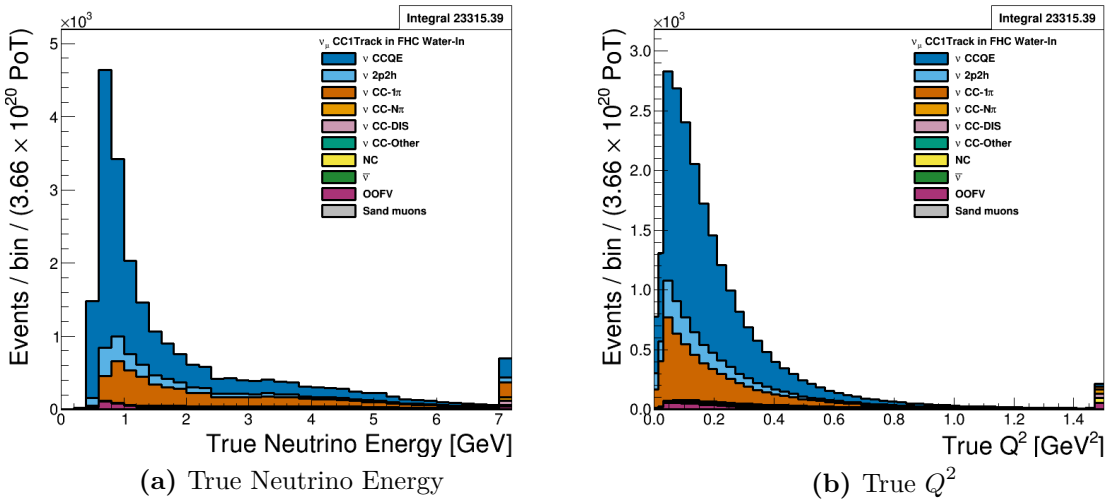


Figure 3.9: The ν_μ in FHC CC 1-Track true kinematics broken down by true NEUT interaction modes. Water-in mode is displayed here only with the last bin shown is used as overflow. The figures use the PØD water-in MC and are normalized to the FHC water-in mode POT.

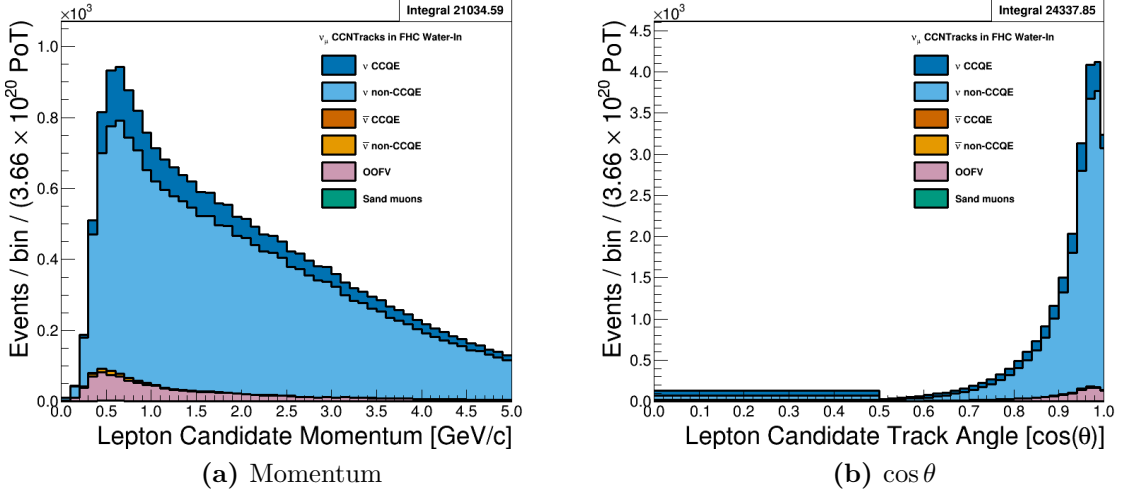


Figure 3.10: Lepton candidate reconstructed P and $\cos\theta$ distributions for the ν_μ in FHC CC N-Tracks selection for CCQE and non-CCQE interactions. The figures use the PØD water-in MC and are normalized to the FHC water-in mode POT.

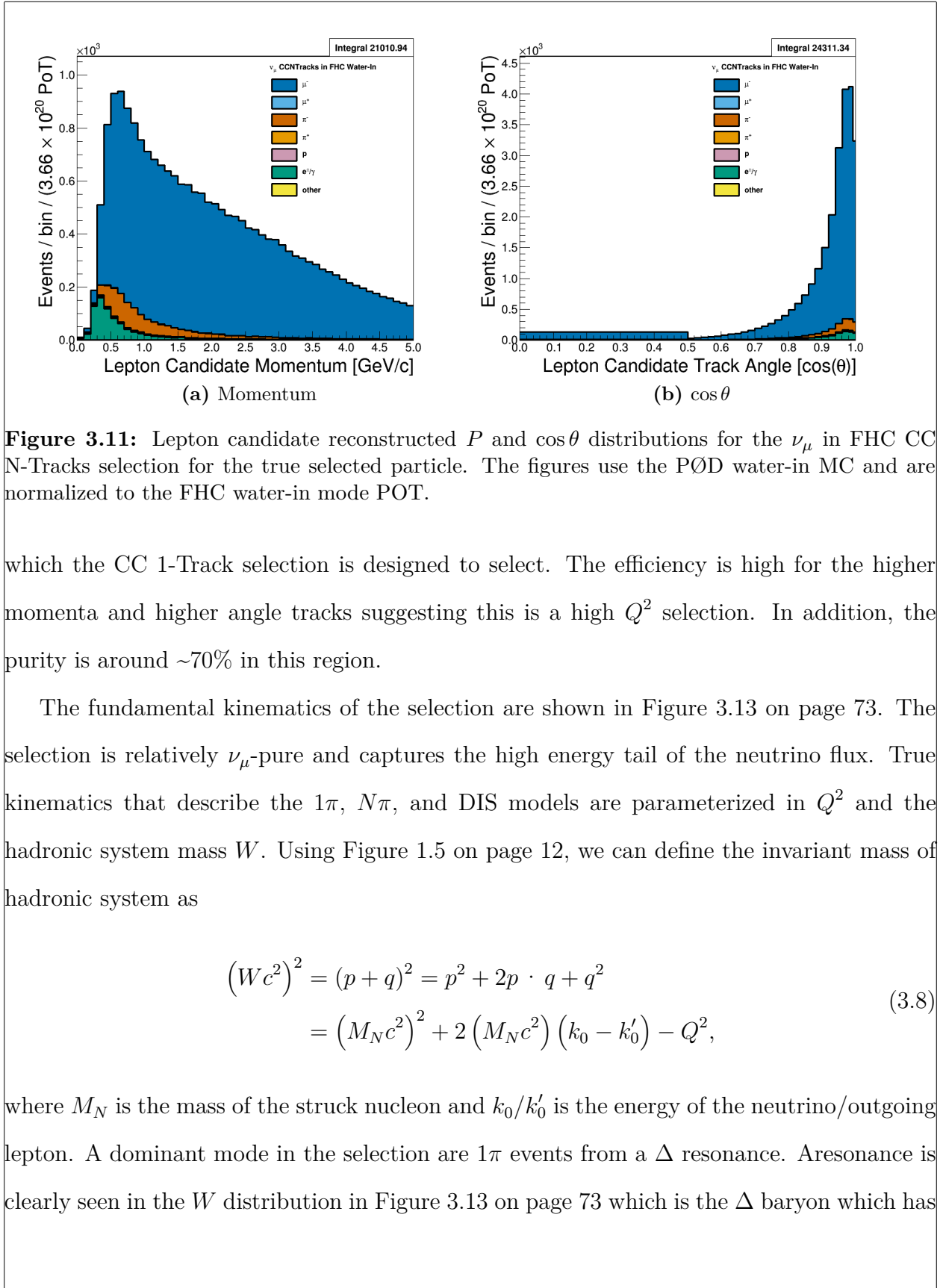
$$\epsilon = \frac{N_{\text{Selected}}^{\text{True}}}{N^{\text{True}}} \quad \rho = \frac{N_{\text{Selected}}^{\text{True}}}{N_{\text{Selected}}}, \quad (3.7)$$

where $N_{\text{Selected}}^{\text{True}}$ is the number of true, selected events, N^{True} is the number of true events, and N_{Selected} is the number of selected events. They demonstrate that the purity is highest near 0.5 GeV/c with the efficiency highly dependent on the track angle.

3.3.2 ν_μ in FHC CC N-Tracks

This selection provides non-CCQE-like samples in FHC mode inputs to BANFF. The reconstructed momentum and angular distributions are shown in Figure 3.10 on page 70 and Figure 3.11 on page 71. Since this selection is not optimized for any particular CC topology, there are a variety of interactions modes present including 1π , multiple pion ($N\pi$) and deep inelastic scattering (DIS). There are a number of mis-identified lepton candidates in the form of electrons and pions.

We can examine the efficiencies and purities differentially for the selection in Figure 3.12 on page 72. The true signal here is any ν_μ CC interaction except ν_μ CCQE (CC non-QE)



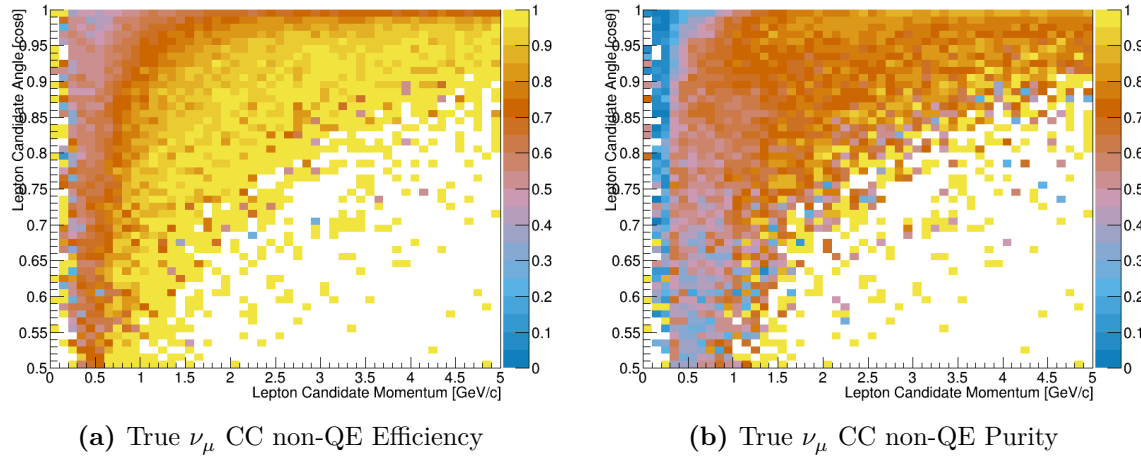


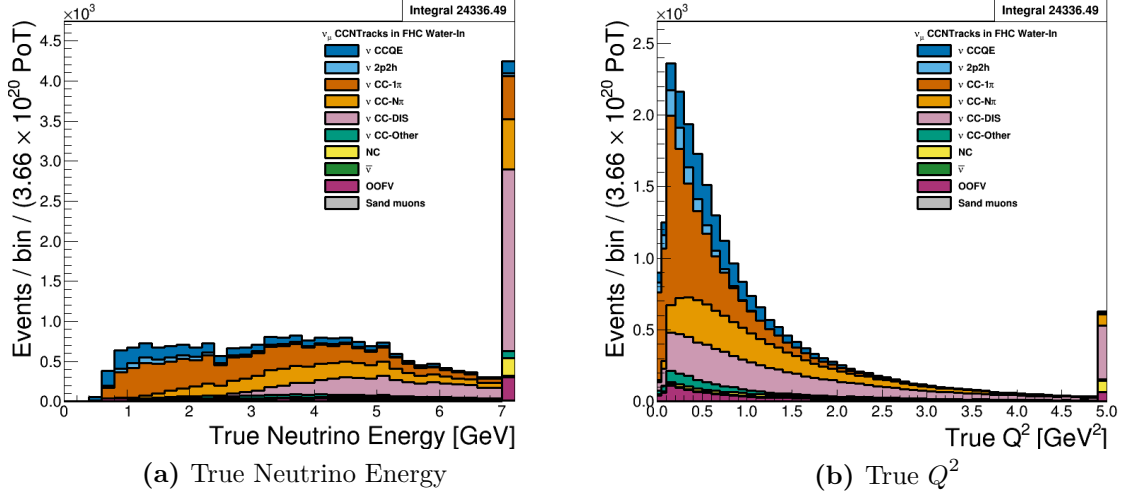
Figure 3.12: The efficiency and purity in reconstructed kinematics of ν_μ CC non-QE interactions in the ν_μ in FHC CC N-Tracks selection. True events are defined as correctly matched μ^- tracks from ν_μ -induced CC non-QE interactions at the vertex.

a rest mass of 1.232 GeV/c². Higher order resonance states are present as well since there are no cuts to distinguish muons and pions from protons.

The origin of the mis-identified particles, in particular the pions, becomes more clear since this is a high Q^2 selection. Multiple pion and DIS events can produce a negatively charged pion. For high Q^2 interactions topologies, the energy transfer to the final hadronic state can produce a higher energy pion than the true muon or the muon does not enter the TPC.

3.3.3 $\bar{\nu}_\mu$ in RHC CC 1-Track

This selection provides the $\bar{\nu}_\mu$ CCQE-like samples in RHC mode that are inputs to BANFF. In Figure 3.14 on page 74 and Figure 3.15 on page 75 display the momentum and angular distributions for this selection. The selection is $\bar{\nu}_\mu$ -pure with the selected lepton candidate being positively charged muons. There is a large OOFV background from proton tracks. They are high momentum (> 1 GeV/c) tracks which, at these energies, are become minimum ionizing and can reach into the TPC.



(a) True Neutrino Energy

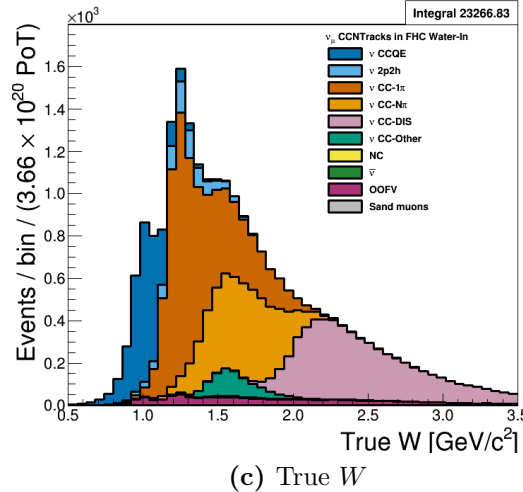
(b) True Q^2 (c) True W

Figure 3.13: The ν_μ in FHC CC N-Tracks true kinematics broken down by true NEUT interaction modes. The last bin shown in (a) and (b) is used as overflow. The figures use the PØD water-in MC and are normalized to the FHC water-in mode POT.

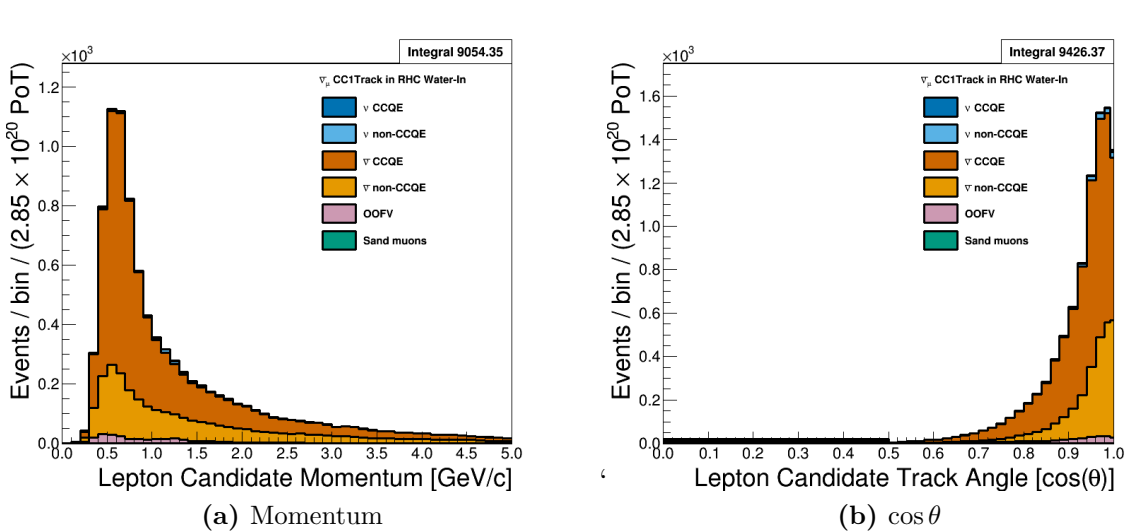


Figure 3.14: Lepton candidate reconstructed P and $\cos\theta$ distributions for the $\bar{\nu}_\mu$ in RHC CC 1-Track selection for CCQE and non-CCQE interactions. The figures use the PØD water-in MC and are normalized to the RHC water-in mode POT.

We can examine the efficiencies and purities differentially for the selection in Figure 3.16 on page 75. The two distributions are very similar to the ν_μ in FHC CC 1-Track efficiencies and purities, with the efficiency being relatively high (90%) for high statistics regions.

The underlying true kinematics, E_ν and Q^2 , of the interactions are shown in Figure 3.17 on page 76. We see a similar true reaction composition to the ν_μ in FHC selection in Section 3.3.1. Most reactions are true CCQE with a mixture of 2p2h and 1 π events. As previously seen in Section 3.3.1, the significant 1 π contamination may reduce the sensitivity both CC-0 π and CC-1 π model parameters in the BANFF fit.

3.3.4 $\bar{\nu}_\mu$ in RHC CC N-Tracks

This selection provides the $\bar{\nu}_\mu$ non-CCQE-like samples in RHC mode. Figure 3.18 on page 76 and Figure 3.19 on page 77 display the momentum and angular distributions that are inputs to BANFF. The most striking feature of this selection is the the number of mis-identified events. In particular protons are selected as the HMPT when they become minimum ionizing particles, which is about 1.3 GeV/c. At these energies protons can escape

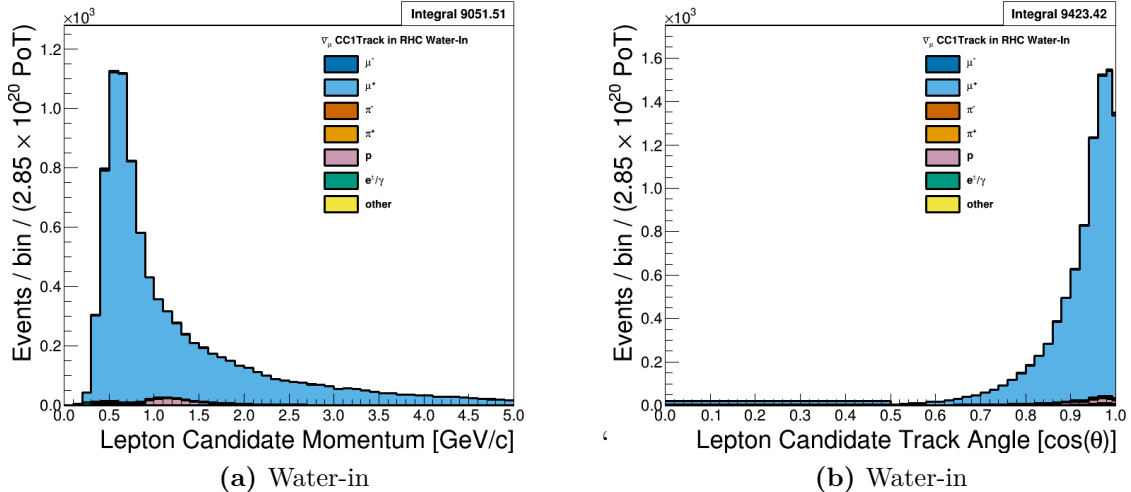


Figure 3.15: Lepton candidate reconstructed P and $\cos\theta$ distributions for the $\bar{\nu}_\mu$ in RHC CC 1-Track selection for the true selected particle. The figures use the PØD water-in MC and are normalized to the RHC water-in mode POT.

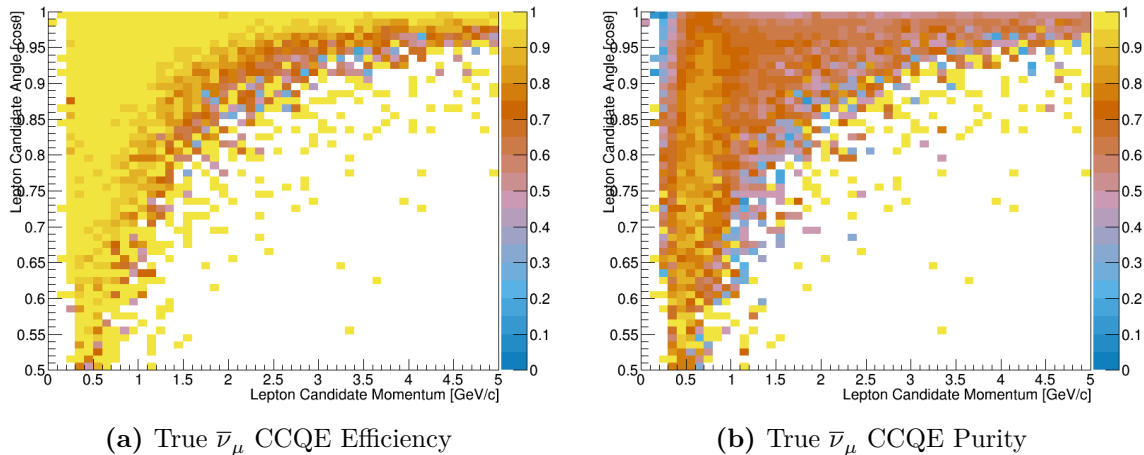


Figure 3.16: The efficiency and purity in reconstructed kinematics of $\bar{\nu}_\mu$ CCQE interactions in the $\bar{\nu}_\mu$ in RHC CC 1-Track selection. The true events are $\bar{\nu}_\mu$ CCQE at the vertex and the selected lepton candidate is the true μ^+ .

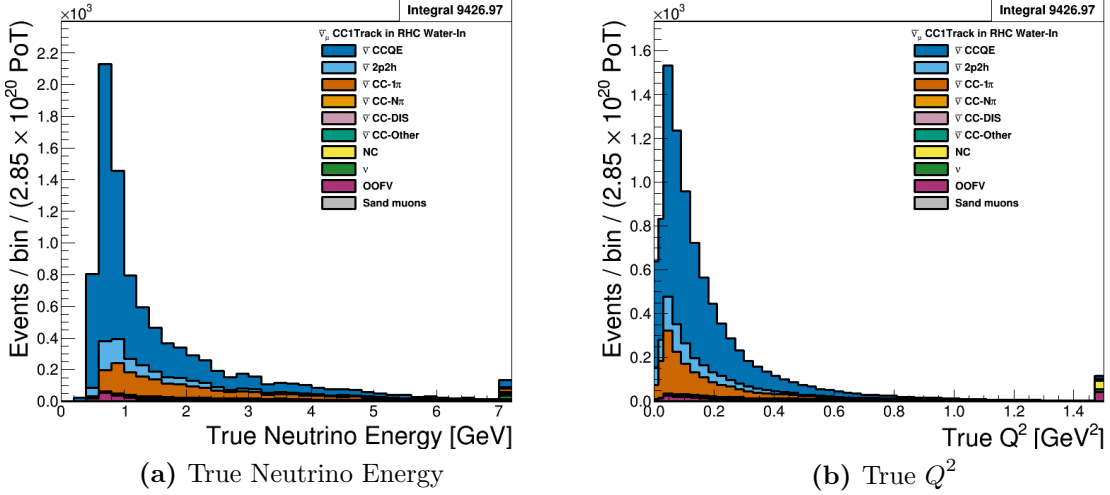


Figure 3.17: The $\bar{\nu}_\mu$ in RHC CC 1-Track true kinematics broken down by true NEUT interaction modes. Water-in mode is displayed here only with the last bin shown is used as overflow. The figures use the PØD water-in MC and are normalized to the RHC water-in mode POT.

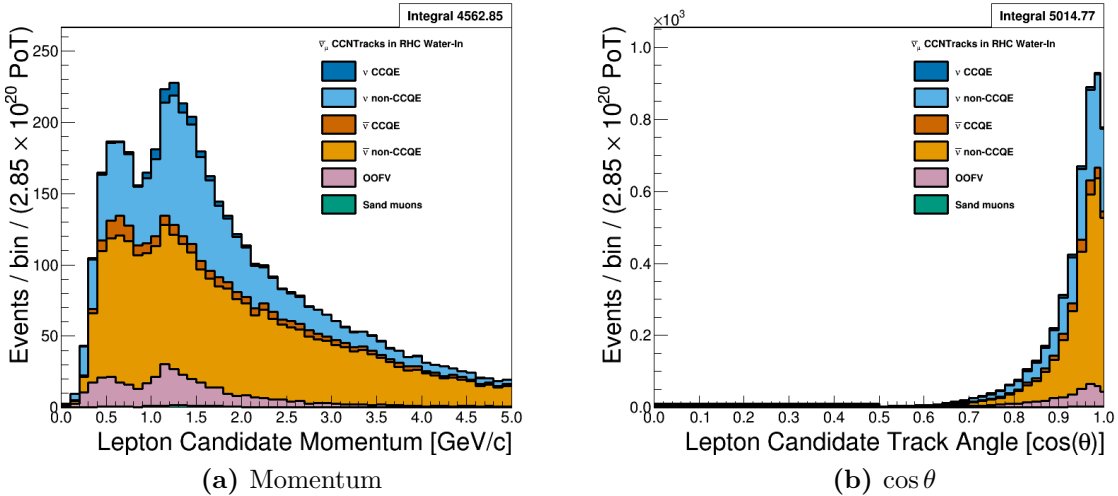
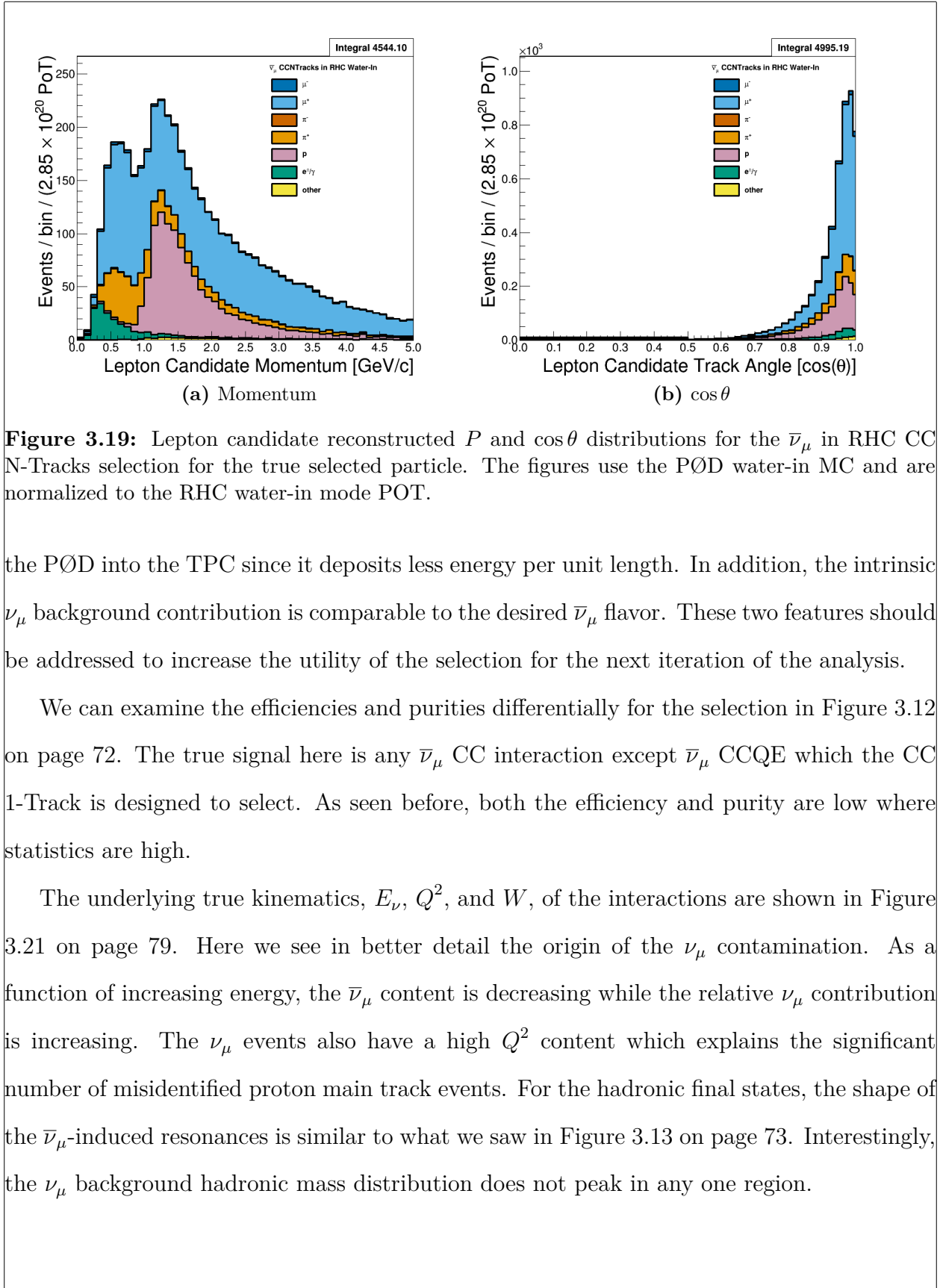


Figure 3.18: Lepton candidate reconstructed P and $\cos \theta$ distributions for the $\bar{\nu}_\mu$ in RHC CC N-Tracks selection for CCQE and non-CCQE interactions. The figures use the PØD water-in MC and are normalized to the RHC water-in mode POT.



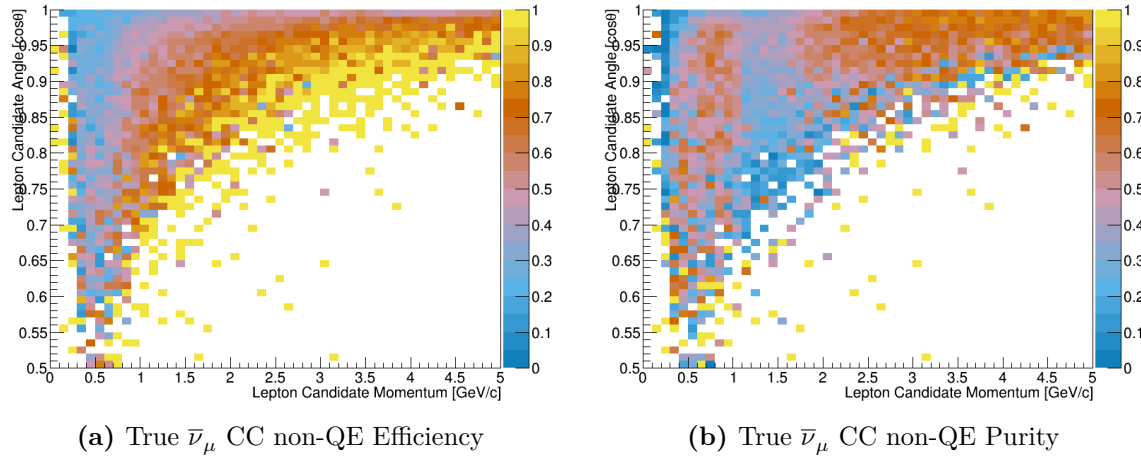


Figure 3.20: The efficiency and purity in reconstructed kinematics of $\bar{\nu}_\mu$ CC non-QE interactions in the $\bar{\nu}_\mu$ in RHC CC N-Track selections. The true events are any $\bar{\nu}_\mu$ CC interaction except $\bar{\nu}_\mu$ CCQE at the vertex and the selected lepton candidate is the true μ^+ .

3.3.5 ν_μ Background in RHC CC 1-Track

This selection provides the ν_μ in RHC, also called wrong-sign background, CCQE-like samples. Figure 3.22 on page 80 and Figure 3.23 on page 80 display the momentum and angular distributions that are inputs to BANFF. We can see this is a relatively low-angle, forward going selection compared to previous selections. Importantly the selection is ν_μ -pure which should help constrain the wrong-sign background in BANFF. However, the CCQE purity is modest given number of correctly identified lepton candidates.

We can examine the efficiencies and purities differentially for the selection in Figure 3.24 on page 81, The efficiency is similar to the ν_μ in FHC CC 1-Track efficiency. As for the purity, it is roughly 70% in a banded region between low momenta, low angle and high momenta, high angle tracks.

The underlying true kinematics, E_ν and Q^2 , of the selection are shown in Figure 3.25 on page 81. Due to the flux of the wrong-sign background, the neutrino energy is not sharply peaked at 0.6 GeV. This explains the significant non-CCQE event contamination in the form of 2p2h and 1π interactions.

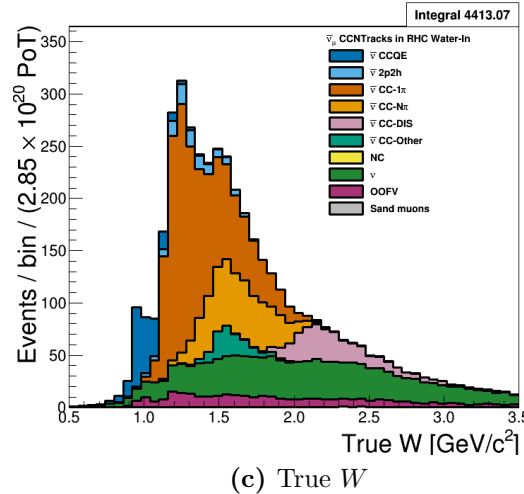
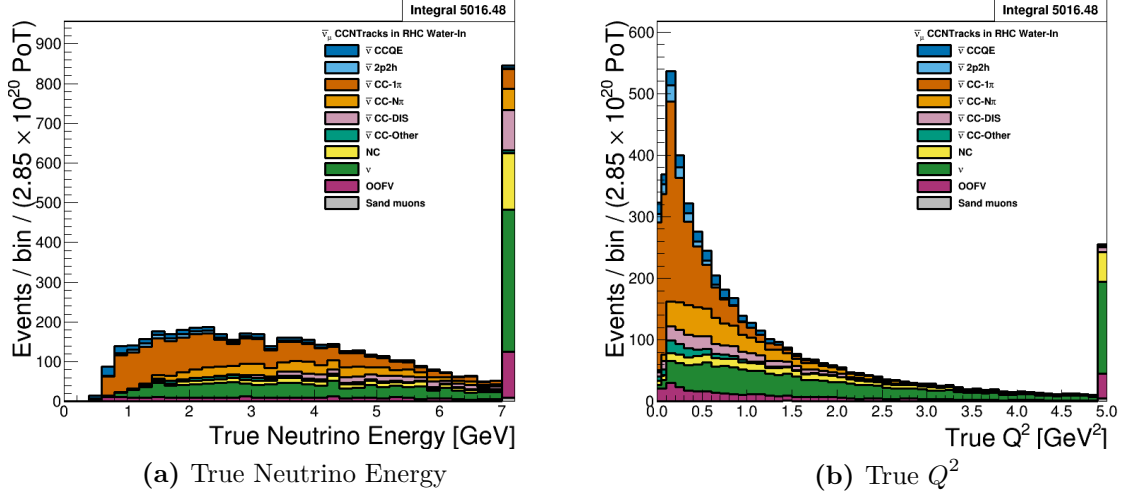


Figure 3.21: The $\bar{\nu}_\mu$ in RHC CC N-Tracks true kinematics broken down by true NEUT interaction modes. The last bin shown in (a) and (b) is used as overflow. The figures use the PØD water-in MC and are normalized to the RHC water-in mode POT.

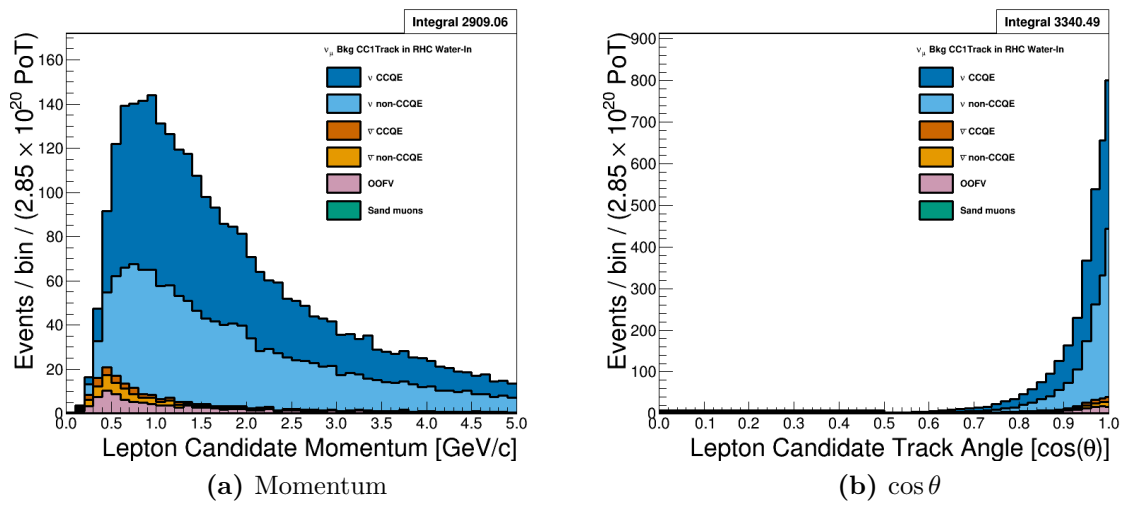


Figure 3.22: Lepton candidate reconstructed P and $\cos \theta$ distributions for the ν_μ in RHC CC 1-Track selection for CCQE and non-CCQE interactions. The figures use the PØD water-in MC and are normalized to the RHC water-in mode POT.

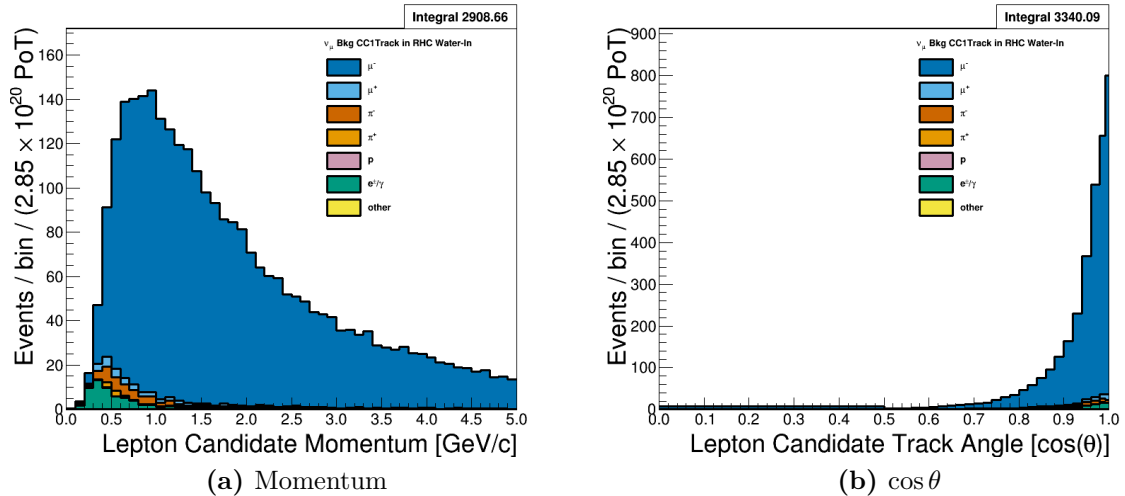
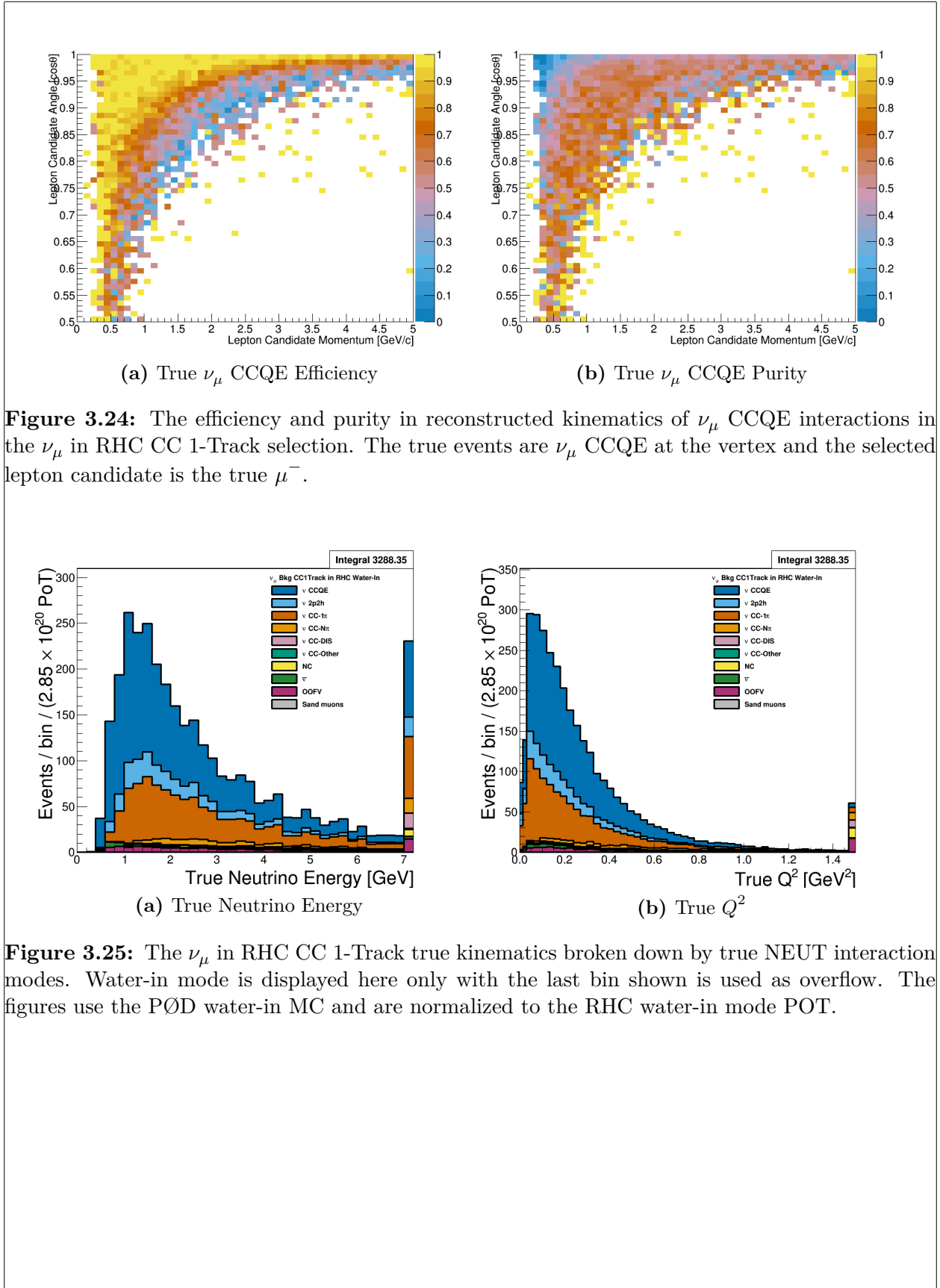


Figure 3.23: Lepton candidate reconstructed P and $\cos \theta$ distributions for the ν_μ in RHC CC 1-Track selection for the true selected particle. The figures use the PØD water-in MC and are normalized to the RHC water-in mode POT.



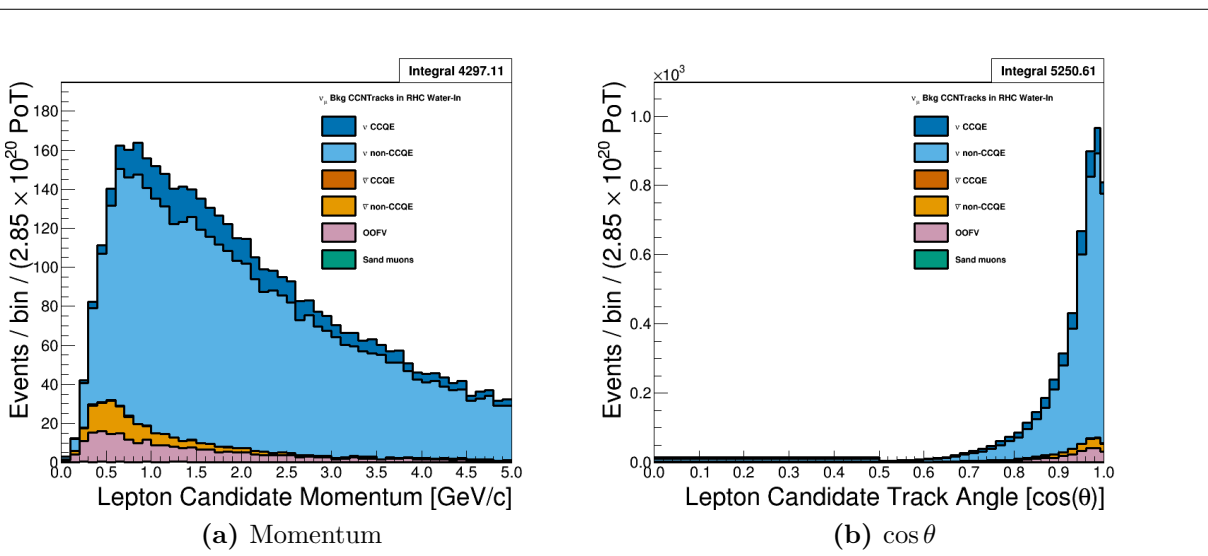


Figure 3.26: Lepton candidate reconstructed P and $\cos\theta$ distributions for the ν_μ in RHC CC N-Tracks selection for CCQE and non-CCQE interactions. The figures use the PØD water-in MC and are normalized to the RHC water-in mode POT.

3.3.6 ν_μ Background in RHC CC N-Tracks

This selection provides the ν_μ background non-CCQE-like samples in RHC mode. Figure 3.26 on page 82 and Figure 3.27 on page 83 show the momentum and angular distributions that are inputs to BANFF. We can see the selection is relatively ν_μ -pure with a significant mis-identified track rate. Interestingly, the misidentified pion main tracks have a high momentum tail.

We can examine the ν_μ CC non-QE efficiency and purity of the selection in Figure 3.28 on page 83. There is a reduction in the purity below 1.5 GeV/c due to the the $\bar{\nu}_\mu$ selections occupying the same phase space. Fortunately, the efficiency and purity are relatively high above 1.5 GeV/c.

The underlying true kinematics, E_ν , Q^2 , and W , of the interactions are shown in Figure 3.29 on page 85. As we have seen before with the CC N-Tracks samples, these are high E_ν events with large Q^2 exchanges. The invariant hadronic system displays the previously seen resonances, with the largest still being from the Δ baryon.

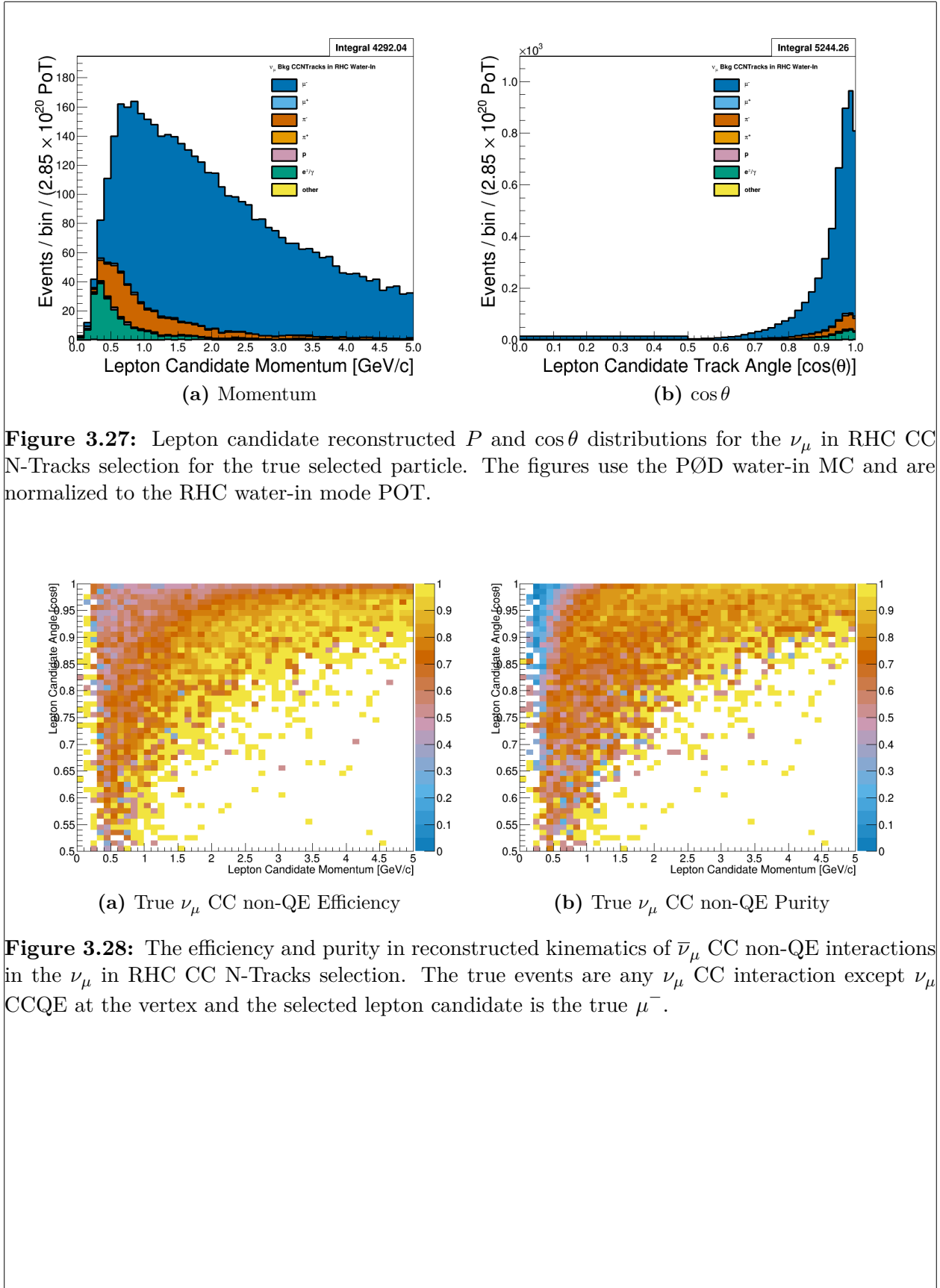
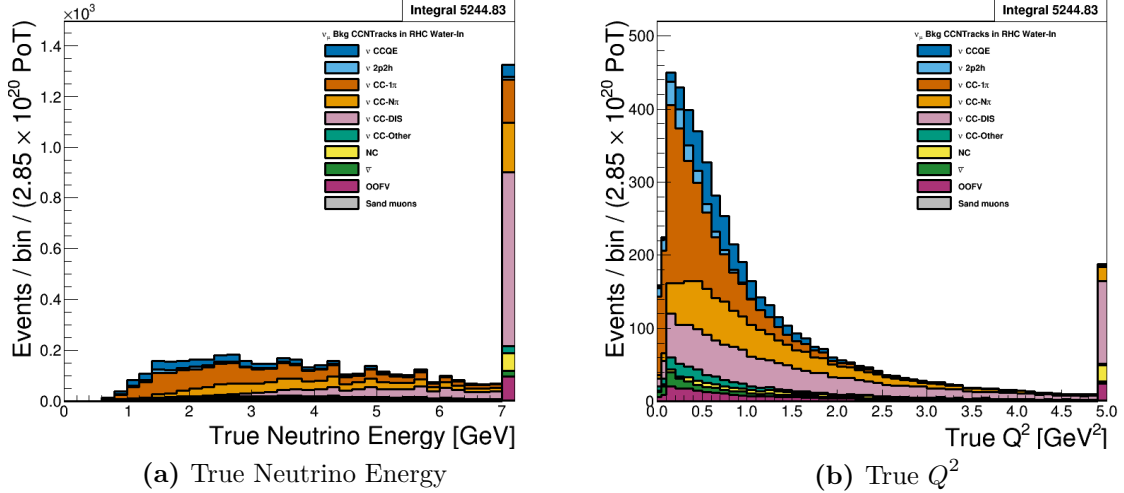


Figure 3.27: Lepton candidate reconstructed P and $\cos\theta$ distributions for the ν_μ in RHC CC N-Tracks selection for the true selected particle. The figures use the PØD water-in MC and are normalized to the RHC water-in mode POT.

Figure 3.28: The efficiency and purity in reconstructed kinematics of $\bar{\nu}_\mu$ CC non-QE interactions in the ν_μ in RHC CC N-Tracks selection. The true events are any ν_μ CC interaction except ν_μ CCQE at the vertex and the selected lepton candidate is the true μ^- .

3.4 Summary of Selections

We have examined that the selection procedures described above produces some reasonably pure CCQE samples using the 1-Track cut. By inverting that cut, we obtain some handles on other topologies like CC 1π and high Q^2 CCDIS events. Importantly is the ability to constrain the correct sign ν_μ and wrong sign backgrounds in RHC. We can now move forward to the systematic uncertainties present in the analysis.



(a) True Neutrino Energy

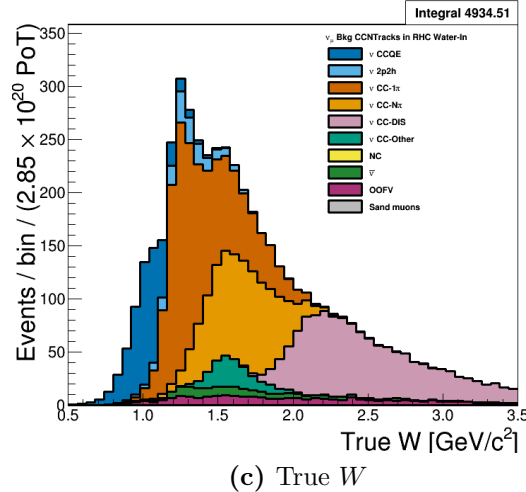
(b) True Q^2 (c) True W

Figure 3.29: The ν_μ in RHC CC N-Tracks true kinematics broken down by true NEUT interaction modes. The last bin shown in (a) and (b) is used as overflow. The figures use the PØD water-in MC and are normalized to the RHC water-in mode POT.

Chapter 4

The PØD-Only in BANFF Parameterization

In addition to the likelihood ratio maximization, the BANFF fit includes three sources of systematic uncertainties: neutrino flux, cross section model, and detector inefficiencies. This chapter explores the fit binning and penalty terms in the test statistic in this analysis. The sources of systematic uncertainties, also referred to just as systematics, will be defined in order to understand their effect on any analysis.

This chapter is presented in the following order. The first section explores the method to define fit bins in the likelihood ratio. The second section is divided into three subsections to define the parameterization of each penalty term in the test statistic. The penalty terms discussed in order are the neutrino flux model, the detector inefficiencies, and lastly the cross section model.

4.1 Fit Binning

The PØD ND280 BANFF fit uses the samples described in Chapter 3. The bin edges used in the BANFF fit to evaluate the log-likelihood ratio term, $\Delta\chi^2_{\text{LLR}}$, are tabulated below.

There are a total 988 fit bins with water-in and water-out modes sharing the same bin edges.

The determination of the fit binning is discussed below.

- ν_μ in CC 1-Track fit bin edges:

- p [GeV/c]: 0, 0.3, 0.4, 0.5, 0.6, 0.7, 0.8, 1, 1.25, 1.5, 2, 3, 4, 5.5, 30

- $\cos \theta$: -1, 0.7, 0.8 , 0.88, 0.94, 0.96, 0.975, 0.99, 1

- ν_μ in FHC CC N-Tracks fit bin edges:

- p [GeV/c]: 0, 0.4, 0.5, 0.6, 0.7, 0.8, 1, 1.2, 1.5, 1.8, 2.2, 2.7, 3.5, 5, 10, 30

- $\cos \theta$: -1, 0.65, 0.77, 0.85, 0.9, 0.94, 0.97, 0.99, 1

- $\bar{\nu}_\mu$ in RHC CC 1-Track fit bin edges:

- p [GeV/c]: 0, 0.4, 0.5, 0.6, 0.7, 0.8, 1, 1.25, 1.5, 2, 3, 30

- $\cos \theta$: -1, 0.82, 0.87, 0.9, 0.93, 0.95, 0.97, 0.99, 1

- $\bar{\nu}_\mu$ in RHC CC N-Tracks fit bin edges:

- p [GeV/c]: 0, 0.5, 0.9, 1.25, 1.6, 2, 3, 8, 30

- $\cos \theta$: -1, 0.8, 0.89, 0.95, 0.97, 0.99, 1

- ν_μ in RHC CC 1-Track fit bin edges:

- p [GeV/c]: 0, 0.4, 0.6, 0.8, 1.1, 2, 10

- $\cos \theta$: -1, 0.78, 0.84, 0.89, 0.92, 0.95, 0.97, 0.98, 0.99, 1

- ν_μ in RHC CC N-Tracks bin edges:

- p [GeV/c]: 0, 0.4, 0.6, 0.8, 1, 1.5, 2, 3, 10

- $\cos \theta$: -1, 0.7, 0.8, 0.85, 0.9, 0.94, 0.965, 0.98, 0.99, 1

4.1.1 Fit Binning Determination

The fit binning is optimized to ensure at least 1 predicted Monte Carlo (MC) event in each bin when scaled to the collected data POT. The fit bins must also account for detector smearing effects. In order to mitigate smearing and event migration, the reconstructed kinematics were examined to their MC truth value using only correctly identified leptons in one-dimensional kinematic slices. Since the MC provides about $10\times$ the data statistics, the statistical uncertainty for each bin should be negligible in high statistics regions. The kinematics are scanned across their full relevant spaces in order to understand the required width for a fit bin. The first fit bin is always defined starting from the kinematic maximum.

For the momentum bins, the momentum resolution is compared to MC truth. The momentum resolution is defined as

$$R(r, t) = \frac{r - t}{t},$$

where r is the reconstructed momentum and t is the true momentum. The momentum was scanned in finite bin widths with the mean and standard deviation of the resolution R extracted. The mean and standard deviation are used as a proxy for the true bias and resolution, respectively. In addition, a bootstrapping algorithm was employed to understand the accuracy of the sample estimates. Bootstrapping in this context is sampling over all relevant values of true momentum and randomly replacing the values. For each scanned bin, at least 1000 bootstrapping sampling with replacement was performed. In the case of large variances in the bootstrapping samples, additional 10000 sampling with replacement were performed. The results for analyzing the ν_μ in FHC CC 1-Track selection is shown in Figure 4.1 on page 89.

The angle bins are treated in an almost identical manner. While the fit bins and Physics are dictated in $\cos\theta$ space, the detector smearing is a function θ . In addition, since the angle can be nearly zero for the most forward-going tracks, the resolution was not used to

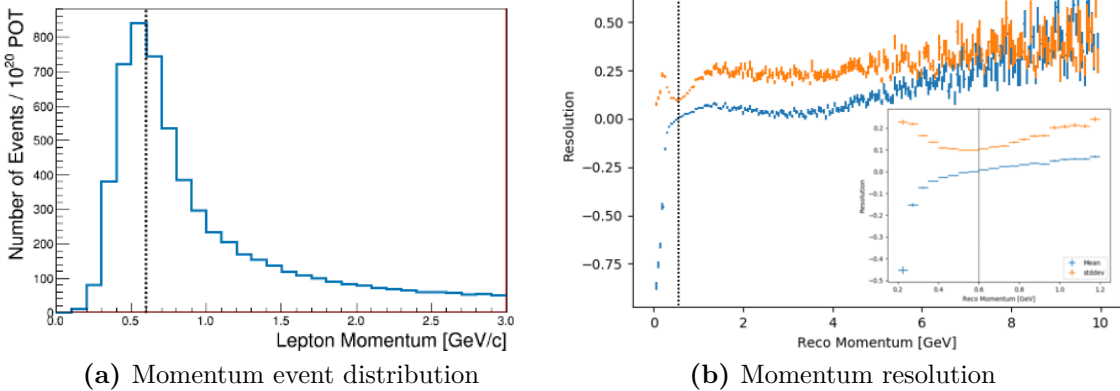


Figure 4.1: The momentum event distribution and uncertainty for ν_μ in FHC CC 1-Track events is shown above. Only correctly identified muons are shown. (a) The number of events is scaled to 10^{20} POT which is the approximate scale for all the samples in this analysis. A dashed line indicates the maximum of the peak. (b) The resolution of the momentum measurement is shown for a wide region of momenta. In the inset is the resolution zoomed near the momentum distribution maximum. Like in (a), a dashed line shows the momentum maximum.

characterize the angular uncertainties. Instead, the difference between the true and reconstructed angle were analyzed as shown in Figure 4.2 on page 90. The mean and standard deviation were studied as before to set the fit $\cos \theta$ bin edges. Bootstrapping was again used to quantify the accuracy of the mean and standard deviation.

4.2 Penalty Terms and Systematic Uncertainties

This section expands on the definition of the penalty terms in the BANFF fit. The cross section and flux penalty terms in this analysis are identical to previous BANFF studies since the T2K experiment utilizes a set of canonical flux and cross section systematics that are shared between ND280 and SK. Also, those systematics are not altered in this analysis for the purpose of comparability between PØD-only and FGD-only best fit results. For the ND280 detector systematics, many are shared between the PØD and TPC subdetectors. However, due to the different detector technologies, additional detector inefficiency systematics will be incorporated.

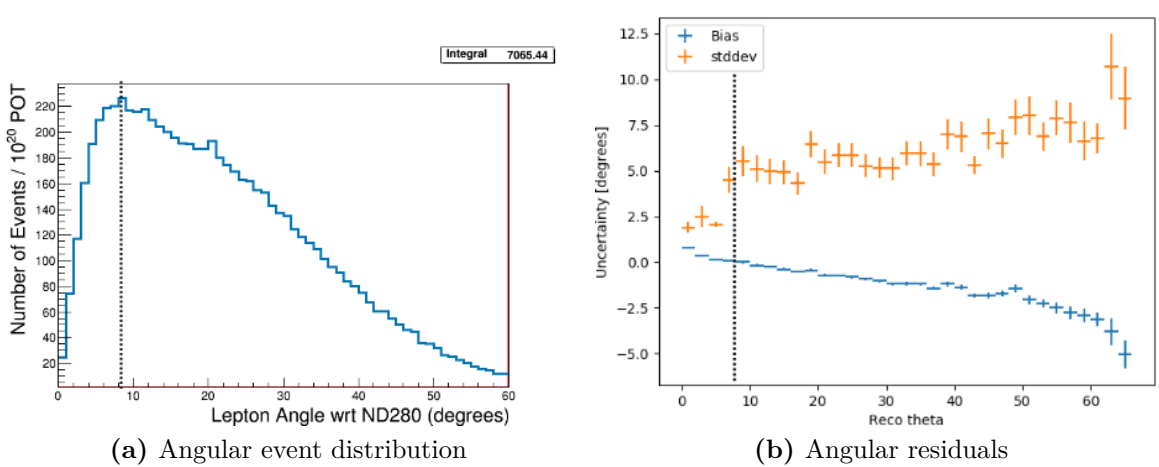


Figure 4.2: The angular event distribution and uncertainty for ν_μ in FHC CC 1-Track events is shown above. Only correctly identified muons are shown. (a) The number of is scaled to 10^{20} POT which is the approximate scale for all the samples in this analysis. A dashed line indicates the track angle distribution maximum of the peak. (b) The residual of the angular measurement is shown up to where there are sufficient statistics. Like in (a), a dashed line shows the distribution maximum.

4.2.1 Flux Model

The T2K neutrino flux model is a description of the neutrino beam spectrum by run period and flavor. This model includes simulations of the beam interactions and subsequent hadron production at the target. The predicted hadron production rate, including inside and outside the target, is tuned based to the results from the NA61/SHINE [9] replica target experiment and other hadron production experiments. The uncertainties in the unoscillated flux tuning are dominated on hadron production. Smaller effects on the unoscillated flux uncertainty include the proton beam profile, off-axis angle, horn current, and horn alignment. Further details about the flux model and uncertainties can be found here [4].

The flux penalty term in the BANFF fit is defined, as previously seen in Chapter 2, as

$$\Delta\chi_{\text{Flux}}^2 = \Delta\vec{b} \cdot \left(V_b^{-1}\right) \cdot \Delta\vec{b}^T. \quad (4.1)$$

All penalty terms in this analysis follow this format with each b_i corresponding to a neutrino energy bin normalization. These bins are further differentiated by horn current/polarity

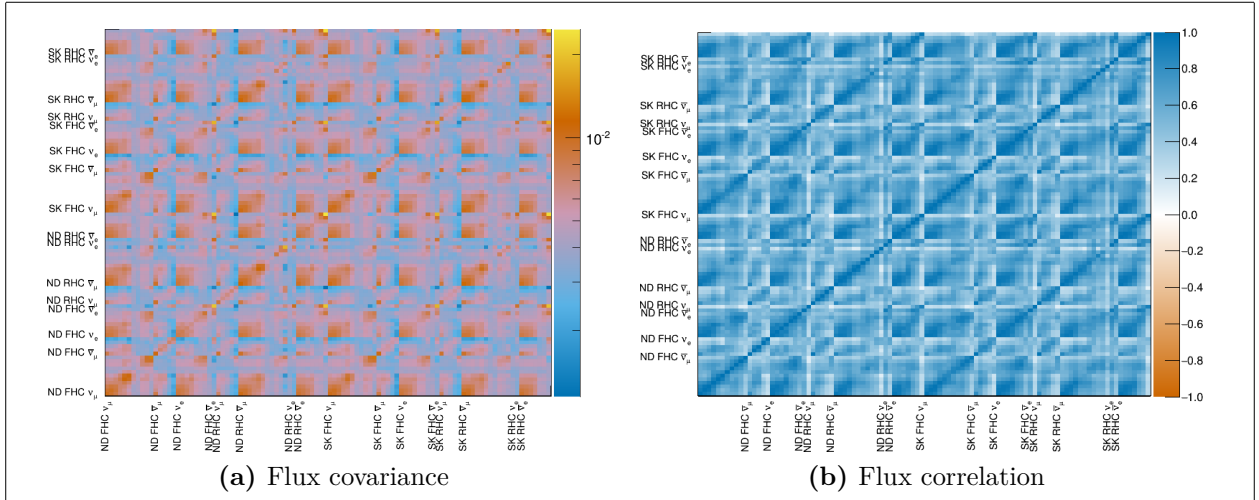


Figure 4.3: BANFF pre-fit flux covariance matrix shown with respective detector, horn current, and neutrino flavor.

(FHC and RHC) and neutrino flavor (ν_μ , $\bar{\nu}_\mu$, ν_e , and $\bar{\nu}_e$). The binning and covariance matrix, shown in Figure 4.3 on page 91, is provided by the T2K flux group.

There are 50 ND280 and 50 SK flux parameters to yield a total of 100 flux normalizations. In addition, the bin edges are shared between the ND280 and SK. The SK neutrino flux and the flux bin edges are shown in Figure 4.4 on page 96. In the BANFF fit, both ND280 and SK flux parameters are extracted simultaneously. This is achieved using correlations between ND280 and SK flux parameters as shown in Figure 4.3 on page 91. The tabulated flux parameters/bins in this analysis are given in Table 4.1 on page 95. Each flux bin is assigned with an initial value of one (1) for all events in that neutrino energy bin. A postfit value of 1.1 indicates that all events in that energy bin have an additional weight of 1.1, signaling that the postfit prefers to increase that neutrino flux by 10%.

Table 4.1: Flux binning and uncertainties used in the BANFF fit.

Bin index	Beam mode	Bin edges [GeV]	Prefit
0	ND280 ν_μ FHC	0.0 - 0.4	1 ± 0.100909
1		0.4 - 0.5	1 ± 0.099431
2		0.5 - 0.6	1 ± 0.092025

Table 4.1: Flux binning and uncertainties used in the BANFF fit.

Bin index	Beam mode	Bin edges [GeV]	Prefit
3		0.6 - 0.7	1 ± 0.085239
4		0.7 - 1.0	1 ± 0.105356
5		1.0 - 1.5	1 ± 0.104375
6		1.5 - 2.5	1 ± 0.073612
7		2.5 - 3.5	1 ± 0.068993
8		3.5 - 5.0	1 ± 0.082334
9		5.0 - 7.0	1 ± 0.097308
10		7.0 - 30	1 ± 0.114706
11	ND280 $\bar{\nu}_\mu$ FHC	0.0 - 0.7	1 ± 0.103804
12		0.7 - 1.0	1 ± 0.084158
13		1.0 - 1.5	1 ± 0.081349
14		1.5 - 2.5	1 ± 0.085208
15		2.5 - 30	1 ± 0.087735
16	ND280 ν_e FHC	0.0 - 0.5	1 ± 0.091336
17		0.5 - 0.7	1 ± 0.089699
18		0.7 - 0.8	1 ± 0.084648
19		0.8 - 1.5	1 ± 0.079722
20		1.5 - 2.5	1 ± 0.079766
21		2.5 - 4.0	1 ± 0.081399
22		4.0 - 30	1 ± 0.095795
23	ND280 $\bar{\nu}_e$ FHC	0.0 - 2.5	1 ± 0.072069
24		2.5 - 30	1 ± 0.142921
25	ND280 ν_μ RHC	0.0 - 0.7	1 ± 0.094066
26		0.7 - 1.0	1 ± 0.079866
27		1.0 - 1.5	1 ± 0.080948

Table 4.1: Flux binning and uncertainties used in the BANFF fit.

Bin index	Beam mode	Bin edges [GeV]	Prefit
28		1.5 - 2.5	1 ± 0.083251
29		2.5 - 30	1 ± 0.082653
30	ND280 $\bar{\nu}_\mu$ RHC	0.0 - 0.4	1 ± 0.107277
31		0.4 - 0.5	1 ± 0.098851
32		0.5 - 0.6	1 ± 0.089710
33		0.6 - 0.7	1 ± 0.084692
34		0.7 - 1.0	1 ± 0.106871
35		1.0 - 1.5	1 ± 0.098711
36		1.5 - 2.5	1 ± 0.073350
37		2.5 - 3.5	1 ± 0.070520
38		3.5 - 5.0	1 ± 0.092905
39		5.0 - 7.0	1 ± 0.089083
40		7.0 - 30	1 ± 0.134911
41	ND280 ν_e RHC	0.0 - 2.5	1 ± 0.066214
42		2.5 - 30	1 ± 0.086977
43	ND280 $\bar{\nu}_e$ RHC	0.0 - 0.5	1 ± 0.095575
44		0.5 - 0.7	1 ± 0.089033
45		0.7 - 0.8	1 ± 0.088406
46		0.8 - 1.5	1 ± 0.081472
47		1.5 - 2.5	1 ± 0.078353
48		2.5 - 4.0	1 ± 0.089427
49		4.0 - 30	1 ± 0.156972
50	Super-K ν_μ FHC	0.0 - 0.4	1 ± 0.102555
51		0.4 - 0.5	1 ± 0.101771
52		0.5 - 0.6	1 ± 0.092573

Table 4.1: Flux binning and uncertainties used in the BANFF fit.

Bin index	Beam mode	Bin edges [GeV]	Prefit
53		0.6 - 0.7	1 ± 0.084265
54		0.7 - 1.0	1 ± 0.102271
55		1.0 - 1.5	1 ± 0.084528
56		1.5 - 2.5	1 ± 0.066909
57		2.5 - 3.5	1 ± 0.072355
58		3.5 - 5.0	1 ± 0.085299
59		5.0 - 7.0	1 ± 0.096725
60		7.0 - 30	1 ± 0.114112
61	Super-K $\bar{\nu}_\mu$ FHC	0.0 - 0.7	1 ± 0.103129
62		0.7 - 1.0	1 ± 0.078327
63		1.0 - 1.5	1 ± 0.082367
64		1.5 - 2.5	1 ± 0.082121
65		2.5 - 30	1 ± 0.085123
66	Super-K ν_e FHC	0.0 - 0.5	1 ± 0.090918
67		0.5 - 0.7	1 ± 0.087065
68		0.7 - 0.8	1 ± 0.082527
69		0.8 - 1.5	1 ± 0.076514
70		1.5 - 2.5	1 ± 0.075773
71		2.5 - 4.0	1 ± 0.082078
72		4.0 - 30	1 ± 0.092882
73	Super-K $\bar{\nu}_e$ FHC	0.0 - 2.5	1 ± 0.071921
74		2.5 - 30	1 ± 0.128982
75	Super-K ν_μ RHC	0.0 - 0.7	1 ± 0.093954
76		0.7 - 1.0	1 ± 0.076369
77		1.0 - 1.5	1 ± 0.074900

Table 4.1: Flux binning and uncertainties used in the BANFF fit.

Bin index	Beam mode	Bin edges [GeV]	Prefit
78		1.5 - 2.5	1 ± 0.078108
79		2.5 - 30	1 ± 0.077505
80	Super-K $\bar{\nu}_\mu$ RHC	0.0 - 0.4	1 ± 0.108593
81		0.4 - 0.5	1 ± 0.101912
82		0.5 - 0.6	1 ± 0.092787
83		0.6 - 0.7	1 ± 0.082669
84		0.7 - 1.0	1 ± 0.102090
85		1.0 - 1.5	1 ± 0.087732
86		1.5 - 2.5	1 ± 0.068117
87		2.5 - 3.5	1 ± 0.069902
88		3.5 - 5.0	1 ± 0.091711
89		5.0 - 7.0	1 ± 0.084736
90		7.0 - 30	1 ± 0.115488
91	Super-K ν_e RHC	0.0 - 2.5	1 ± 0.066204
92		2.5 - 30	1 ± 0.082645
93	Super-K $\bar{\nu}_e$ RHC	0.0 - 0.5	1 ± 0.095453
94		0.5 - 0.7	1 ± 0.088889
95		0.7 - 0.8	1 ± 0.085644
96		0.8 - 1.5	1 ± 0.078536
97		1.5 - 2.5	1 ± 0.075246
98		2.5 - 4.0	1 ± 0.086384
99		4.0 - 30	1 ± 0.152507

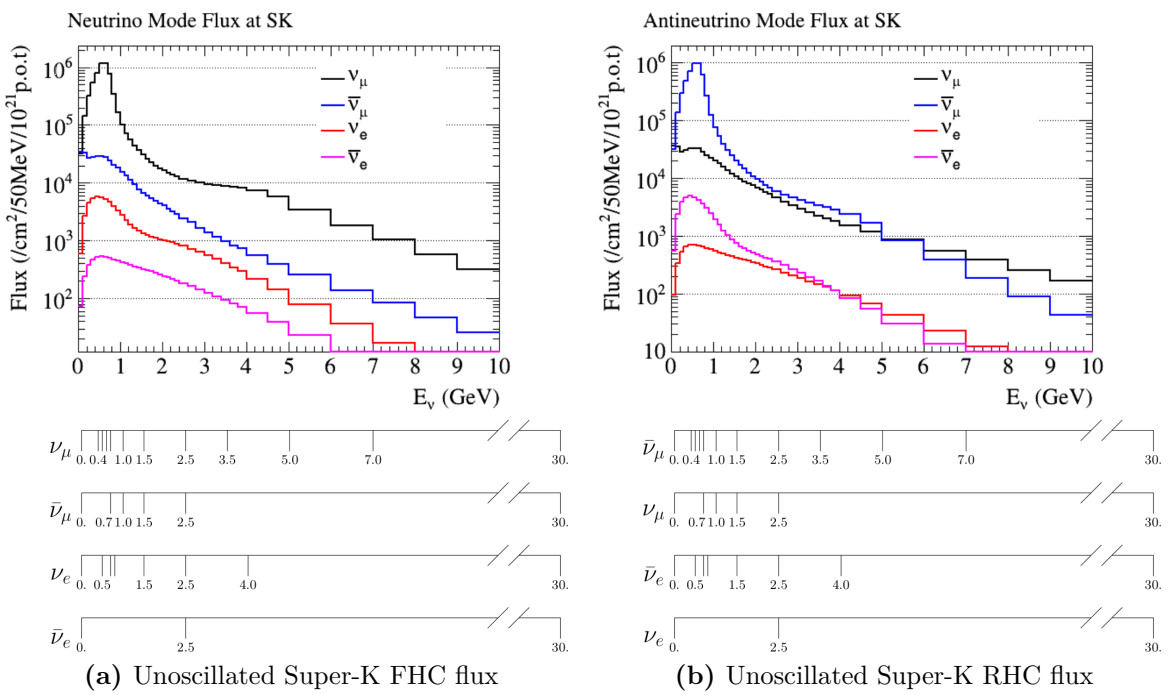


Figure 4.4: The T2K unoscillated neutrino flux prediction at SK for FHC (left) and RHC (right) modes. The shared ND280 and SK binning used for the flux systematic parameters is also shown below the plots.

4.2.2 Detector Inefficiencies Model

In the BANFF fit, bin normalization parameters are used to evaluate the detector inefficiency penalty term, $\Delta\chi^2_{\text{Det}}$. The idea is that the MC does not accurately model detector inefficiencies that affect the predicted event rate. Since improperly modeled inefficiencies can cause event migrate from sample-to-sample, bin-to-bin, or both, numerous fake “toy experiments” are performed to evaluate possible scenarios. When all toy experiments are analyzed together, the variation in the event rate provides a constraint on the bin normalization uncertainty. We will see the result of such variations in the coming pages. Hitherto in this thesis, detector inefficiencies will be referred to as detector systematics.

All the detector systematics are evaluated either as observable variations or weights. An observable variation affects the physical observables of selected events like the calculated energy loss of a track in the PØD. A weight is a multiplicative factor that alters the normalization of a single event in a bin. The list of detector systematics used in this analysis is given in Table 4.2 on page 98. The TPC systematics are fully discussed in the following reference [4]. Description of the new PØD-only systematics will be explained below.

4.2.2.1 Systematic Treatments

There are two types of systematic treatments in this analysis: observable variations and weights. Each rely on the method of throwing a random number, x , to evaluate the systematic.

Efficiency-like systematics are treated as weights to the MC predictions in order to evaluate the uncertainty the systematic has on an analysis. They are based on studies comparing data and MC predictions in control samples (CS). A CS is designed to provide a reliable measurement with minimal influence from other dependent and independent factors. An example of a well established CS is a collection of single, isolated cosmic ray (muon) tracks to measure the energy loss in a detector. In general, a CS may have different properties than the analysis sample like event topology. In particular the cosmic ray CS cannot account for

Systematic effect	Affected Detector	Treatment
TPC cluster eff.	TPC	efficiency
TPC tracking eff.	TPC	efficiency
TPC charge misassignment	TPC	efficiency
TPC momentum resol.	TPC	observable variation
TPC momentum scale	TPC	observable variation
B field distortion	TPC	observable variation
Pion secondary interactions	All	efficiency
Proton secondary interactions	All	efficiency
TPC Particle ID	TPC	observable variation
TPC track quality eff.	TPC	efficiency
<hr/>		
PØD energy loss scale	PØD	observable variation
PØD energy loss resol.	PØD	observable variation
PØD mass	PØD	(see text)
PØD-TPC matching eff.	PØD+TPC	(see text)

Table 4.2: List of detector systematic effects and the way each one is treated within the simulated samples to propagate the uncertainty. The systematics listed above the horizontal line are discussed in the following reference [4]. The PØD mass and track matching systematics were not available in the BANFF framework and treated as uncorrelated additions to the total covariance matrix.

efficiency effects if other tracks present. Therefore a model extrapolation is needed to map the CS to the analysis sample. The model used in BANFF is that the efficiency of the data and MC is the same in both analysis sample and CS

$$\epsilon_{\text{Data}}(o) = \left(\frac{\epsilon_{\text{Data}}(o)}{\epsilon_{\text{MC}}(o)} \right)_{\text{CS}} \epsilon_{\text{MC}}(o), \quad (4.2)$$

where $\epsilon_{\text{MC}}/\epsilon_{\text{Data}}$ denotes the mean efficiency of the MC/data as a function of some observable o . We need to update this model to account for statistical uncertainties in the CS. The updated model, with o dependence assumed, is now

$$\epsilon'_{\text{Data}} = \left(\frac{\epsilon_{\text{Data}} + x_{\text{Data}} \cdot \sigma_{\epsilon_{\text{Data}}}}{\epsilon_{\text{MC}} + x_{\text{MC}} \cdot \sigma_{\epsilon_{\text{MC}}}} \right)_{\text{CS}} \epsilon_{\text{MC}} \quad (4.3)$$

where $\sigma_{\epsilon_{\text{MC}}}/\sigma_{\epsilon_{\text{Data}}}$ is the standard deviation of the efficiency of the MC/Data and x_{Data} and x_{MC} are different random normally distributed numbers from $\mathcal{N}(\mu = 0, \sigma^2 = 1)$. A weight

is derived from the event depending if the event is selected, w_{eff} , or not selected, w_{ineff} . These weights are given below

$$\begin{aligned} w_{\text{eff}} &= \frac{\epsilon'_{\text{Data}}}{\epsilon_{\text{MC}}} \\ w_{\text{ineff}} &= \frac{1 - \epsilon'_{\text{Data}}}{1 - \epsilon_{\text{MC}}}. \end{aligned} \quad (4.4)$$

Observable variation systematics are evaluated as alterations to physically measured quantities like momentum and energy. The systematic is evaluated using the following formula

$$o' = o_{\text{Nom}} + \overline{\Delta o} + x\sigma_{\Delta o}, \quad (4.5)$$

where o' is the varied observable value, o_{Nom} is the nominal MC value, $\overline{\Delta o}$ is the average correction to the observable, $\sigma_{\Delta o}$ is the uncertainty on the correction, and x is a random, normal number from $\mathcal{N}(\mu = 0, \sigma^2 = 1)$. The TPC-only momentum resolution is usually a large systematic for BANFF analyses. However, the PØD has additional variation systematics that must be considered.

4.2.2.2 Bin Normalizations and Covariance

After many toy experiments which vary the observables ($p, \cos \theta$) and their weights, the number of varied events per fit bin can be examined. From here, the observable normalization (obsnorm) and covariance terms are calculated. The detector covariance matrix, σ_{Det}^2 , between bins x and y is given as

$$\sigma_{\text{Det}}^2(x, y) = \left[\frac{1}{x_{\text{Nom}}} \right] \left[\frac{1}{y_{\text{Nom}}} \right] (\sigma_{\text{Cov}}^2(x, y) + \sigma_{\text{Stat}}^2(x, y)), \quad (4.6)$$

where “Nom”, “Cov”, and “Stat” refer to the nominal MC prediction, covariance, and statistical uncertainties for bins x and y , respectively. This covariance matrix is a fractional covariance as to be consistent with the definition for the flux covariance matrix. The obsnorm expectation for bin x is

$$x_{\text{Nom}} = \sum_{k=1}^{N_x^{\text{MC}}} w_k, \quad (4.7)$$

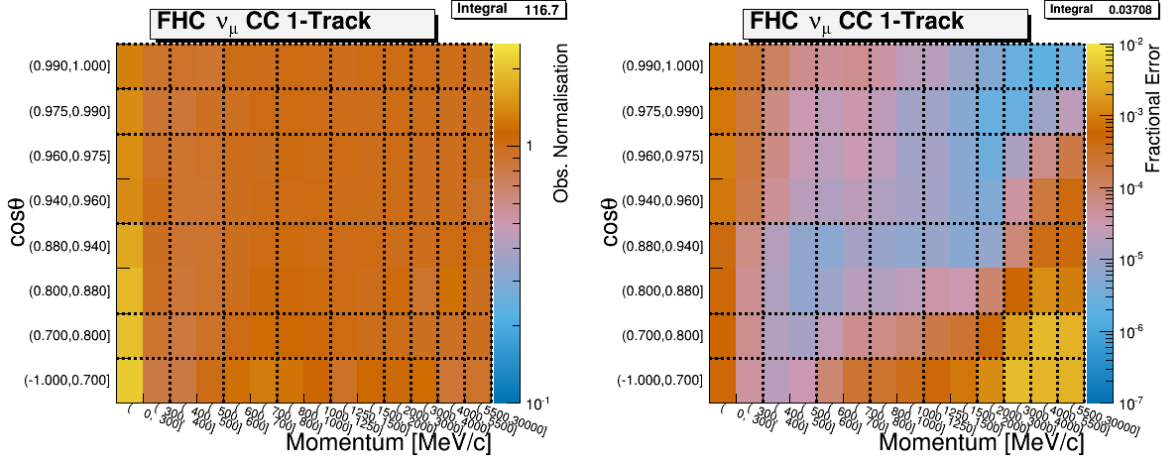
where N_x^{MC} being the number of predicted MC events in the bin and w_k being the product of all the weights applied to the k th event (see (2.8) for all possible weights). The covariance and statistical terms are given by

$$\begin{aligned} \sigma_{\text{Cov}}^2(x, y) &= \frac{1}{N_{\text{Toy}}} \sum_{t=1}^{N_{\text{Toy}}} (x_t - \bar{x})(y_t - \bar{y}) \\ \sigma_{\text{Stat}}^2(x, y) &= \delta(x, y) \sum_{k=1}^{N_x^{\text{MC}}} w_k^2, \end{aligned} \quad (4.8)$$

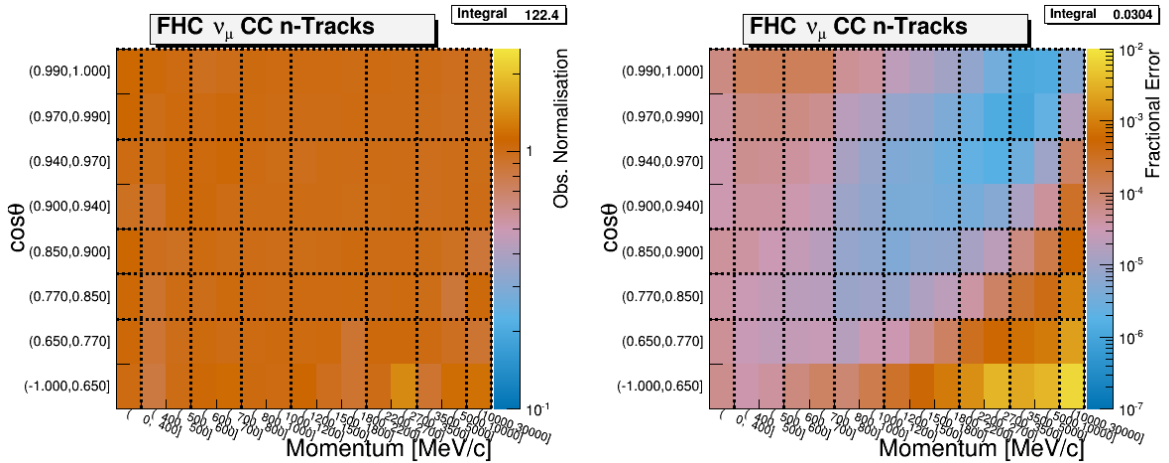
where N_{Toy} is the number of toy experiments, \bar{x}/\bar{y} is the mean of the all the toy experiments in bin x/y , and $\delta(x, y)$ is the Kronecker delta function. Additional uncertainties would be added to the covariance terms in quadrature. This will be

While there could be one obsnorm for each analysis bin, a single obsnorm can be assigned to multiple analysis bins. The purpose is to reduce the number of fit parameters since the time to fit increases non-linearly with the number of fit parameters and events. Previously, the obsnorm edges were determined by combining fit bins with “similar” covariance. This method proved problematic since the fit bins with relatively higher statistics were shared with the same obsnorm parameter. This left the remaining low statistics regions of $(p, \cos \theta)$ phase space more susceptible to systematic variations in the toy experiments.

A new procedure was developed to improve the shortcomings of old procedure which requires careful consideration of the statistical uncertainties and variations between obsnorm prefit values. This procedure can be imagined as lowering the number of contours in a topographic map while considering external constraints from other sensing data. To start, initialize all the obsnorm bin edges to be the same as the fit bin edges. All steps after this are performed iteratively. Starting from the obsnorm bin with the highest statistics, consider merging it with all immediate adjacent bins. Unless individual fractional errors differ significantly before the merge, do not merge them. In this analysis, a factor of 10 in



(a) ν_μ in FHC CC 1-Track



(b) ν_μ in FHC CC N-Tracks

Figure 4.5: Bin normalization edges for the ν_μ in FHC selections. There are two plots shown for each sub-figure. The left and right plots show the bin normalization and the bin statistical fractional error, respectively, if each fit bin had a single bin normalization. The dashed lines indicate the edges of the bin normalization parameters finalized for this analysis.

fractional uncertainty was chosen to describe the similarity between bins. Additionally if the two unmerged bin normalizations differ by more than 10%, perform the bin merging. This step serves to smooth out the obsnorm prefit space.

While the problem of a few obsnorm parameters having the majority of statistics is still present, fluctuations between adjacent obsnorm parameters is iteratively minimized. The detector systematic that had the largest effect on the obsnorm prediction was the PØD energy loss resolution. With it, the event rate in each obsnorm bin varied non-normally. This effect can be seen in Figure 4.8 on page 105.

A considerable drawback to designing normalizations in this way of varying detector systematics in toy experiments is that not all detector systematics affect the observables ($p, \cos \theta$) in the same way. There are non-symmetric systematics and especially non normal in their effects, and so the covariance matrix from (4.6) is not an exact representation of the detector systematics. To demonstrate this, results of varied number of events in are shown in Figure 4.8 on page 105 with an without the PØD energy loss resolution systematic enabled.

The finalized obsnorm bins are listed below and shown visually in Figures 4.5 to 4.7. Their respective fit index and prefit values are tabulated in Appendix A.

- ν_μ in FHC CC 1-Track bin normalization edges:
 - p [GeV/c]: 0, 0.4, 0.6, 0.8, 1.25, 2, 3, 4, 5.5, 30
 - $\cos \theta$: -1, 0.7, 0.8, 0.94, 0.975, 0.99, 1
- ν_μ in FHC CC N-Tracks bin normalization edges:
 - p [GeV/c]: 0, 0.4, 0.6, 0.8, 1.2, 2.2, 3.5, 10, 30
 - $\cos \theta$: -1, 0.77, 0.85, 0.9, 0.97, 1
- $\bar{\nu}_\mu$ in RHC CC 1-Track bin normalization edges:
 - p [GeV/c]: 0, 0.5, 0.6, 0.8, 1.25, 2, 3, 30
 - $\cos \theta$: -1, 0.82, 0.9, 0.95, 0.99, 1

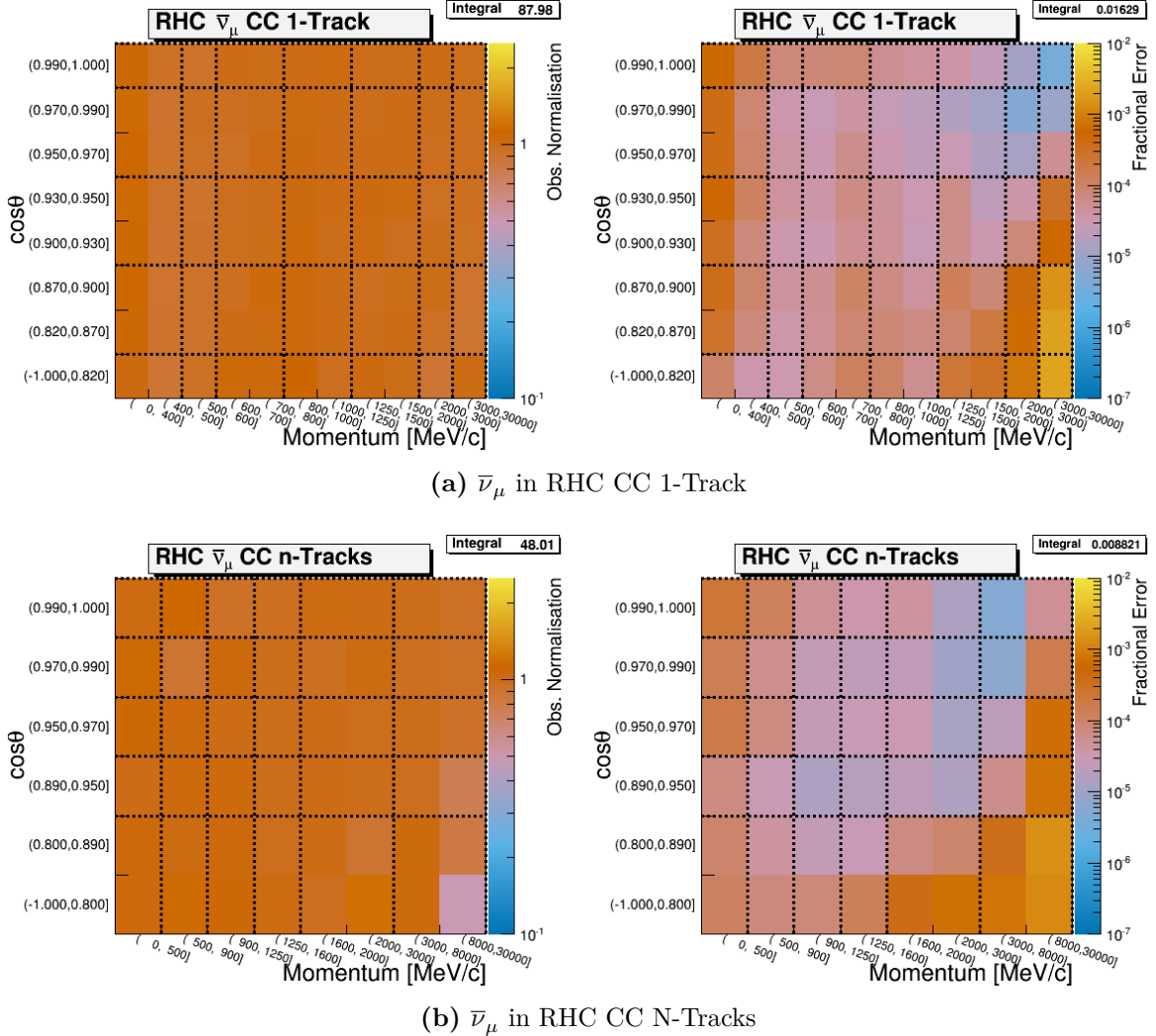
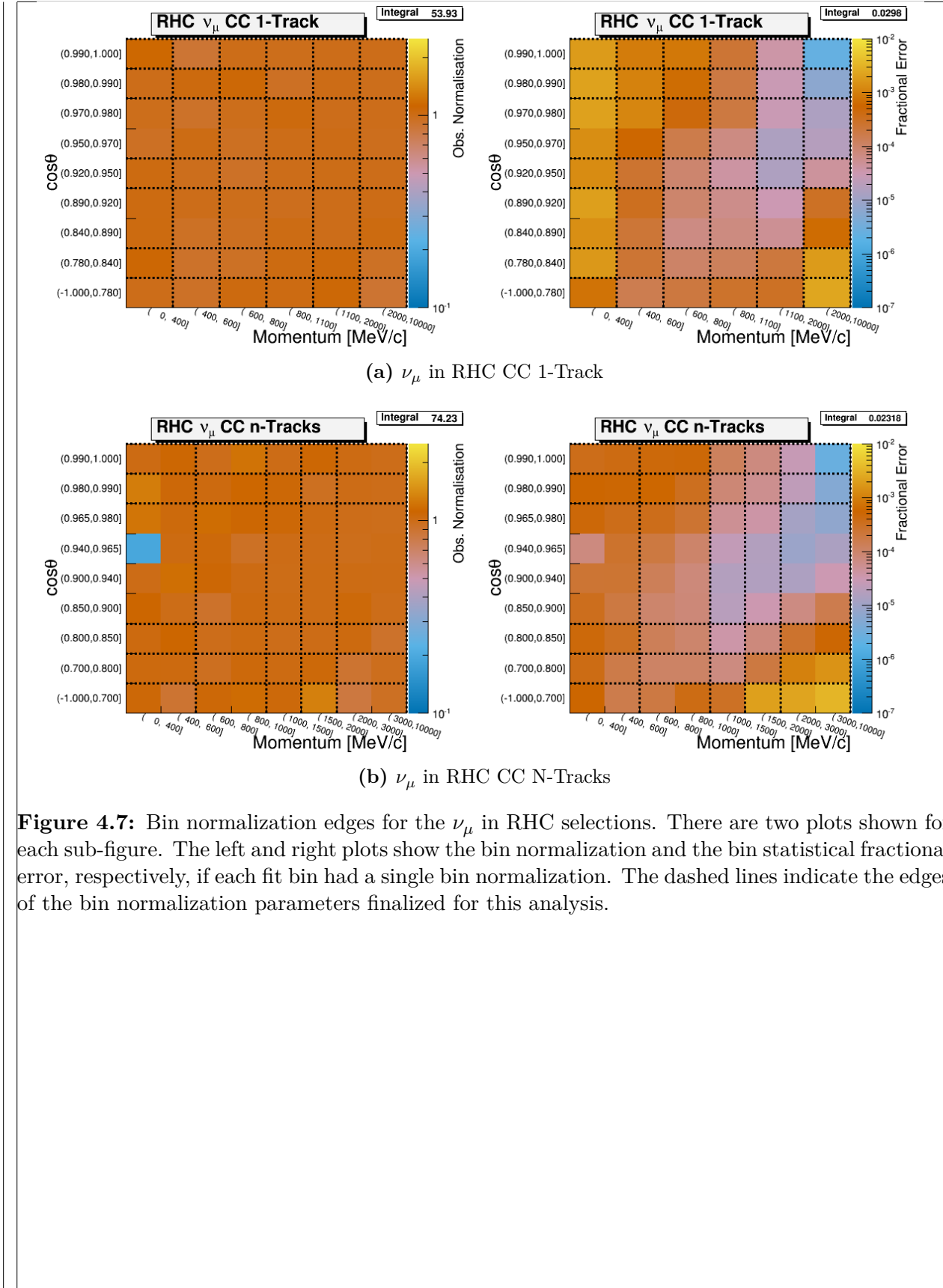


Figure 4.6: Bin normalization edges for the $\bar{\nu}_\mu$ in RHC selections. There are two plots shown for each sub-figure. The left and right plots show the bin normalization and the bin statistical fractional error, respectively, if each fit bin had a single bin normalization. The dashed lines indicate the edges of the bin normalization parameters finalized for this analysis.



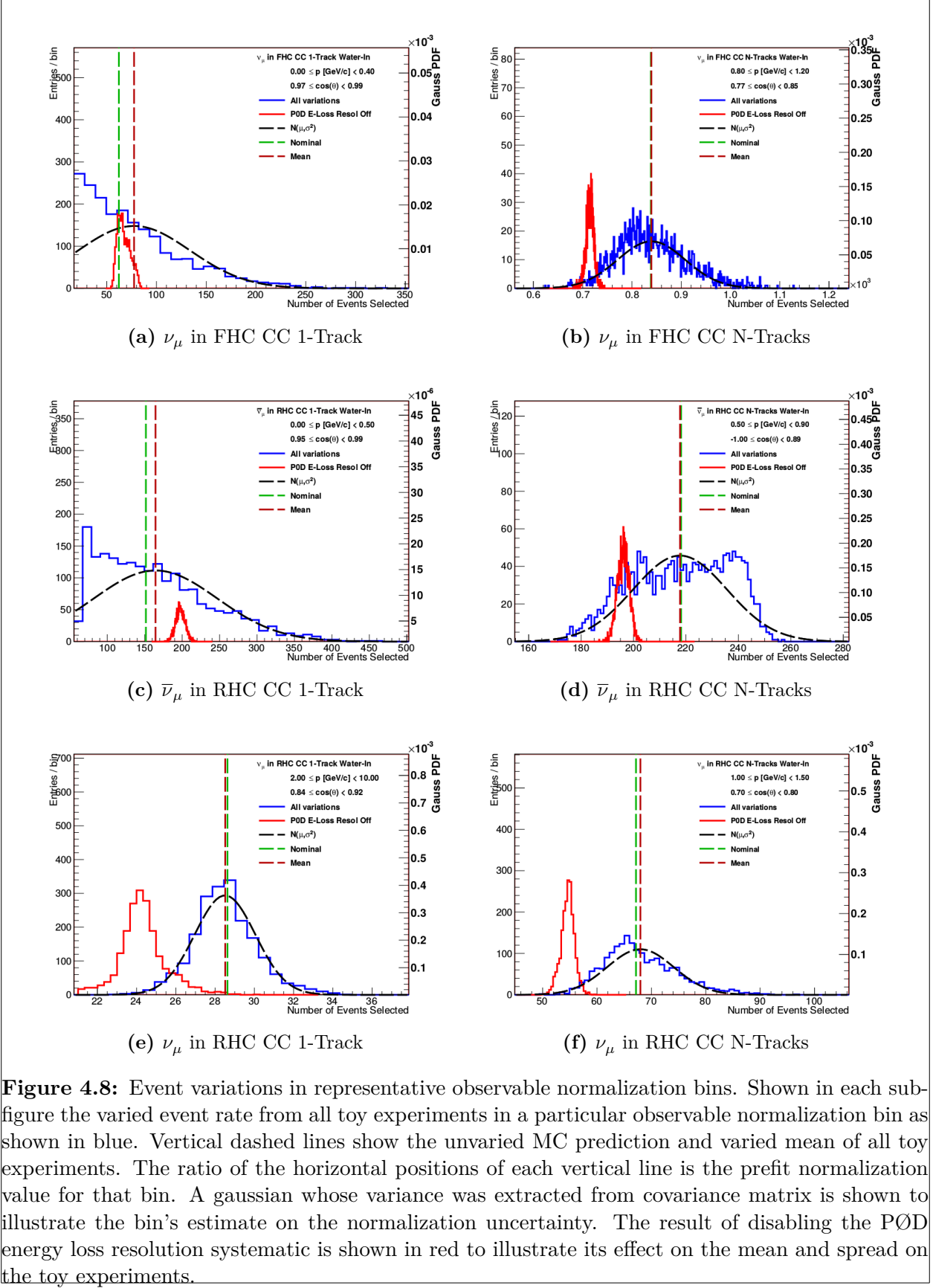


Figure 4.8: Event variations in representative observable normalization bins. Shown in each sub-figure the varied event rate from all toy experiments in a particular observable normalization bin as shown in blue. Vertical dashed lines show the unvaried MC prediction and varied mean of all toy experiments. The ratio of the horizontal positions of each vertical line is the prefit normalization value for that bin. A gaussian whose variance was extracted from covariance matrix is shown to illustrate the bin's estimate on the normalization uncertainty. The result of disabling the PØD energy loss resolution systematic is shown in red to illustrate its effect on the mean and spread on the toy experiments.

- $\bar{\nu}_\mu$ in RHC CC N-Tracks bin normalization edges:
 - p [GeV/c]: 0, 0.5, 0.9, 1.25, 1.6, 3, 30
 - $\cos \theta$: -1, 0.89, 0.95, 0.97, 0.99, 1
- ν_μ in RHC CC T-track bin normalization edges:
 - p [GeV/c]: 0, 0.4, 0.6, 0.8, 1.1, 2, 10
 - $\cos \theta$: -1, 0.78, 0.84, 0.92, 0.95, 0.98, 0.99, 1
- ν_μ in RHC CC N-Tracks bin normalization edges:
 - p [GeV/c]: 0, 0.6, 1, 1.5, 2, 10
 - $\cos \theta$: -1, 0.7, 0.8, 0.85, 0.98, 0.99, 1

4.2.2.3 The PØD-Only Systematics

There are four new PØD-only systematics that are considered for this BANFF fit analysis as listed in Table 4.2 on page 98. All the new sources were initially analyzed in the PØD ν_μ CC- 0π cross section analysis [6].

The energy loss scale and resolution affect the measured momentum in the PØD and are very significant sources of uncertainty. In the ν_μ CC- 0π cross section analysis, the same selection as the ν_μ in FHC CC 1-Track selection, the scale and resolution contributed 1.3% and 6.7%, respectively, to the cross section uncertainty. Those large uncertainties are due to the inherent design of the PØD as a low resolution tracking detector. Slight variations in the track reconstruction can significantly alter the energy loss as measured in (3.5).

The remain systematics, the PØD mass and the PØD-TPC matching efficiency, were not available to analyze in toy experiments variations. They were not implemented in the BANFF framework and unavailable to implement due to time constraints on the author. Instead, they were treated as additional uncorrelated systematics on each bin normalization

uncertainty with the normalization value remaining fixed. The covariance matrix is updated using in the following manner

$$\sigma_{\text{Det}}^2(x, y) \rightarrow \left(\frac{\sigma_{\text{Det}}^2(x, y)}{\bar{x} \cdot \bar{y}} + \tilde{\sigma}_{\text{Mass}}^2 + \tilde{\sigma}_{\text{Match}}^2 \right) \bar{x} \cdot \bar{y}, \quad (4.9)$$

where $\tilde{\sigma}_{\text{Mass}}$ is the fractional uncertainty in the PØD mass and $\tilde{\sigma}_{\text{Match}}$ is the fractional uncertainty in the matching efficiency.

The PØD mass uncertainty is a normalization systematic which affects the event rate. This is a challenging systematic for analyses of recent T2K data due to increasingly faulty sensors to measure the water content. The procedure to fill the water bags required filling them in unison to prevent uneven bulging. However, faulty sensors would provide poor quality data, hence bags were under and overfilled. Prior PØD analyses have estimated the mass uncertainty using similar toy experiment techniques, but did not integrate them into the BANFF framework. In particular in the ν_μ in CC-0 π analysis [6], the PØD mass had an 1.5% systematic effect on the cross section. Since this estimate uses the same method of toy experiments, *a conservative estimate of $\tilde{\sigma}_{\text{Mass}} = 2\%$ was included in this analysis based on the 1.5% mass uncertainty in the cross section.*

The PØD and TPC matching efficiency is estimated to have a small systematic effect on the analysis. It was analyzed to have over a 99.8% data and MC efficiency in the single track ν_μ CC-0 π analysis and thus neglected. However, since this analysis includes multiple track selections, that matching efficiency is unknown. Also, it is hard to imagine a CS that could constrain it. The best handle is from the private T2K technical note on the $\bar{\nu}_\mu/\nu_\mu$ cross section analysis [16] which estimated the uncertainty at less than 0.14% using its in-house matching algorithm. Since that was single bin measurement employing different matching algorithm, the uncertainty is not guaranteed to remain constant across $(p, \cos \theta)$ bins. *A conservative estimate of $\tilde{\sigma}_{\text{Match}} = 1\%$ was chosen in order to account for the inherent uncertainty in this systematic.*

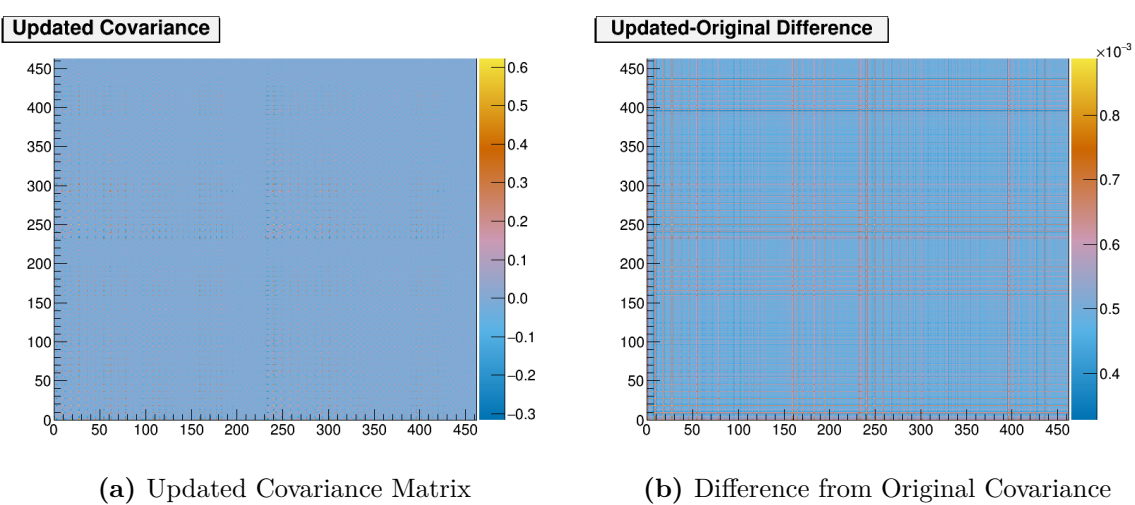


Figure 4.9: Updated detector covariance matrix (a) and the difference from the original (b).

Together, the two additional sources of uncertainty increase each term in the covariance matrix by $0.0005\bar{x} \cdot \bar{y}$, which increases each bin normalization error by about 2.23%. The updated covariance matrix used in this analysis is shown in Figure 4.9 on page 108.

4.2.3 Cross Section Model

There are a number of cross section model systematics implemented in BANFF to account for the uncertainties in cross section measurements. The cross section models used in this analysis use the T2K 2017 parameterization, which is a canonical set of parameters shared among all analyses in T2K. A gross description of the cross section model is provided here with a full technical description of the parameterization is given in the following reference [7].

4.2.3.1 Exclusive Channels

The cross section models with the largest impact on T2K's oscillation sensitivity are CCQE and CCQE-like interactions, collectively called CC-0 π . At energies near the ν_e appearance maximum, $E_\nu = 0.6$ GeV, the CCQE interaction is the largest contributor to the neutrino cross section as shown in Figure 1.30 on page 45. The CCQE model in NEUT, the Llewellyn-Smith model [33] is important historically since it has one unknown parameter.

ter called the Axial Mass, M_A^{QE} , and it well predicts the neutrino energy in low-Z, bubble chamber data. Additionally, the nuclear medium is modeled as a relativistic Fermi gas [36] with a Fermi momentum parameter p_F . Since the number of nucleons is higher in carbon ($A=12$) than oxygen ($A=16$), two different Fermi momentum parameters are specified. There are current model deficiencies and theoretical challenges that make this combined model in NEUT an effective model. As such, flat priors are applied to all CCQE parameters to prevent unintentional biases in the fit result.

There are also CCQE-like interactions that require parameterization since they produce similar topologies to true CCQE events. The T2K experiment currently models CCQE-like interactions involving correlated nucleon interactions with the lowest ordering pair scattering called “2 particle, 2 hole” [35] (2p2h)¹². The “2p2h” interaction refers to the CC interaction mode where a neutrino scatters off neighboring and interacting nucleon pairs. However being relatively new and unconstrained in T2K, flat priors are also applied to all 2p2h normalization and shape parameters, with six in all. *Thus all CC-0 π cross section parameters are unconstrained in the fit, except where physically forbidden.*

NEUT considers other important exclusive channels like resonance states that produce one or more pions. An important pion production channel in T2K is single pion production, or CC-1 π . The CC-1 π model is based on the Rein-Seghal model [39] of neutrino-induced Δ resonance decay into a nucleon and single pion. There are three parameters that describe the CC-1 π , the resonant axial Mass M_A^{Res} , the axial form factor, C_A^5 , and the $1/2$ -isospin background. Again, this model is an effective model as mentioned in the original paper. But unlike the CC-0 π parameters, these and all subsequent models are constrained using Gaussian PDFs.

¹²The name 2p2h originates from Condensed Matter Physics which motivated the model. In solid state matter, a “hole” refers to the absence of an electron in a valence band. In the High Energy Physics context, 2p2h considers an interacting pair of nucleons (2p) scattering from an incoming particle. The imparted energy on the pair excites them to higher energy states leaving two “hole” states (2h) behind.

Harder to measure processes like neutral current (NC) processes and high energy CC normalizations are included as well. There are two CC coherent (Coh) pion production normalization parameters, one for C and O, and one for DIS. There are two NC parameters, one for Coh pion production and other. In order to maintain consistency between the ND280 constraint and oscillation analysis, SK-only normalization parameters are also in the fit, but held as fixed. There are three fixed parameters of this nature.

4.2.3.2 Nuclear Effects

The T2K experiment considers nuclear medium effects that affect the observables in observable cross section. Since outgoing leptons and hadrons must propagate through the nuclear medium before they can be observed, accounting for many body Physics is well motivated. A microscopic, many body nuclear model called “Random Phase Approximation” (RPA) [20] is used as a functional to scale the neutrino-nucleon scattering cross section. The RPA model, as a function of Q^2 , is parameterized as a Q^2 third-order Bernstein polynomial (BeRPA) with a high- Q^2 exponential decay tail. In the BANFF fit, there are four varied (A, B, D, E) and one fixed (U) BeRPA scale parameters.

Pion interactions inside the nucleus called final state interactions [27] (FSI) are considered in the analysis as well. The FSI nuclear model accounts for inelastic (INEL) scattering, pion absorption (ABS), pion production (PROD), and charge exchange (CEX) cross sections. There are a total of six FSI parameters in the fit.

4.2.3.3 Fit Parameters

There are a total of 31 cross section parameters in the BANFF fit. The fit parameters are listed in Table 4.3 on page 113 with the associated correlation matrix in Figure 4.10 on page 111. Following the definition of the flux and bin normalization parameters, cross section parameters are defined as fractional differences to nominal parameters.

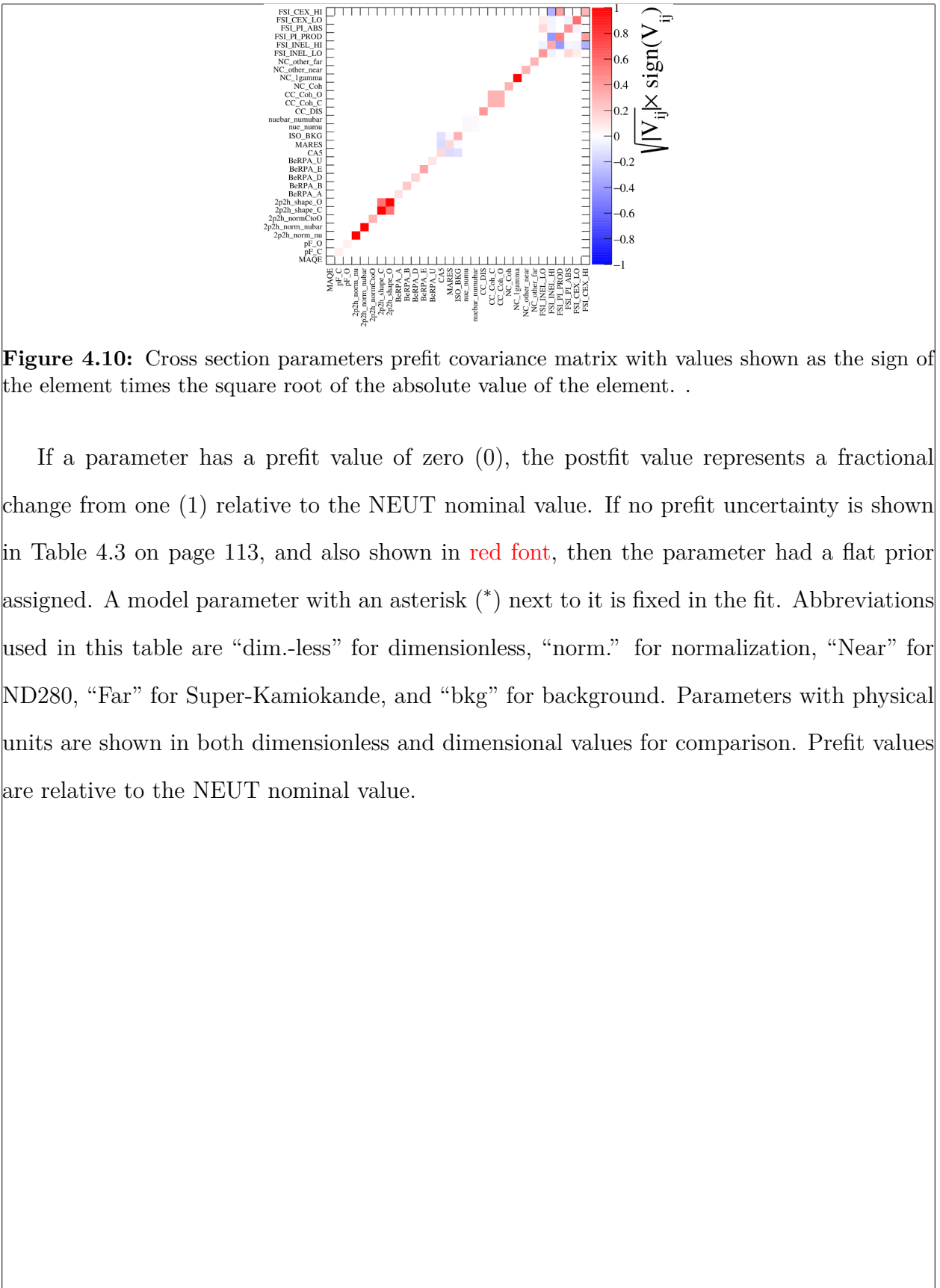


Figure 4.10: Cross section parameters prefit covariance matrix with values shown as the sign of the element times the square root of the absolute value of the element. .

If a parameter has a prefit value of zero (0), the postfit value represents a fractional change from one (1) relative to the NEUT nominal value. If no prefit uncertainty is shown in Table 4.3 on page 113, and also shown in red font, then the parameter had a flat prior assigned. A model parameter with an asterisk (*) next to it is fixed in the fit. Abbreviations used in this table are “dim.-less” for dimensionless, “norm.” for normalization, “Near” for ND280, “Far” for Super-Kamiokande, and “bkg” for background. Parameters with physical units are shown in both dimensionless and dimensional values for comparison. Prefit values are relative to the NEUT nominal value.

Table 4.3: Cross section model parameters in the fit. See the text for a full description.

Fit index	Topology	Model	Parameter	Prefit
562	FSI		Low energy INEL	0 ± 0.41
563			High energy INEL	0 ± 0.34
564			Pion PROD	0 ± 0.41
565			Pion ABS	0 ± 0.5
566			Low energy CEX	0 ± 0.57
567			High energy CEX	0 ± 0.28
568	CC-0 π	Llewellyn-Smith	M_A^{QE} (dim.-less)	1
569		RFG	M_A^{QE} (GeV/c ²)	1.20
570			p_F^C (dim.-less)	1
571			p_F^C (MeV/c)	217
572		Nieves 2p2h	p_F^O (dim.-less)	1
573			p_F^O (MeV/c)	225
574			ν norm. on ¹² C	1
575			$\bar{\nu}$ norm. on ¹² C	1
576			¹² C/ ¹⁶ O norm.	1
577	BeRPA nuclear model		¹² O shape location	0
578			¹⁶ C shape location	0
579			A scale	0.59 ± 0.118
580			B scale	1.05 ± 0.21
			D scale	1.13 ± 0.1695
			E scale	0.88 ± 0.352
			U scale*	1.2 ± 0.1

Table 4.3: Cross section model parameters in the fit. See the text for a full description.

Fit index	Topology	Model	Parameter	Prefit
581	CC- 1π	Rein-Seghal resonant 1π prodction	C_A^5	-0.0495 ± 0.148
582			M_A^{Res} (dim.-less)	0.1263 ± 0.157
			M_A^{Res} (GeV/c^2)	1.07 ± 0.15
583			I= $1/2$ bkg. norm.	-0.261 ± 0.307
584	Other	Event rate at SK	CC- ν_e/ν_μ^*	1 ± 0.0282
585			CC- $\bar{\nu}_e/\bar{\nu}_\mu^*$	1 ± 0.0282
586			CC-DIS	0 ± 0.4
587		Coherent pion production	CC norm. on ^{12}C	1 ± 0.3
588			CC norm. on ^{16}O	1 ± 0.3
589			NC norm.	1 ± 0.3
590		Event rate	NC- $1\gamma^*$	1 ± 1
591			NC Other Near	1 ± 0.3
592			NC Other Far*	1 ± 0.3

Chapter 5

Fitter Validation

Fitter validation

Chapter 6

Fitter Results

Fitter results

Chapter 7

PØD and FGD BANFF Comparisons

P0D-FGD comparisons

Bibliography

- [1] K. Abe et al. The T2K Experiment. *Nucl. Instrum. Meth.*, A659:106–135, 2011. 25, 28, 29, 31, 33, 37, 41
- [2] K. Abe et al. Measurements of the T2K neutrino beam properties using the INGRID on-axis near detector. *Nucl. Instrum. Meth.*, A694:211 – 223, 2012. 32, 34
- [3] K. Abe et al. Observation of Electron Neutrino Appearance in a Muon Neutrino Beam. *Phys. Rev. Lett.*, 112:061802, 2014. 26
- [4] K. Abe et al. Measurement of neutrino and antineutrino oscillations by the T2K experiment including a new additional sample of ν_e interactions at the far detector. 2017. 44, 90, 97, 98
- [5] K. Abe and Others. Measurement of ν_μ and $\bar{\nu}_\mu$ charged current inclusive cross sections and their ratio with the T2K off-axis near detector. *PHYSICAL REVIEW D*, 96(5), September 2017. 39, 54, 56
- [6] K. Abe and Others. First measurement of the ν_μ charged-current cross section on a water target without pions in the final state. *Phys. Rev. D*, 97:012001, Jan 2018. 54, 55, 56, 59, 106, 107
- [7] K. Abe and Others. Search for CP Violation in Neutrino and Antineutrino Oscillations by the T2K Experiment with 2.2×10^{21} Protons on Target. *Phys. Rev. Lett.*, 121:171802, Oct 2018. 26, 108

-
- [8] K. Abe and Others. First Measurement of the Anti-NuMu Charge Current Double Differential Cross Section on Water without Pions in the Final State. *Phys. Rev. D.*, Forthcoming. 54
- [9] N. Abgrall and Others. Measurements of π^\pm , K^\pm , K_S^0 , Λ and proton production in proton-carbon interactions at 31 GeV/c with the NA61/SHINE spectrometer at the CERN SPS. *Eur. Phys. J. C*, 76:84, 2016. 44, 90
- [10] C. Adams et al. The Long-Baseline Neutrino Experiment: Exploring Fundamental Symmetries of the Universe. 2013. arXiv:1307.7335. 4, 21, 25
- [11] S. Agostinelli et al. GEANT4: A Simulation toolkit. *Nucl. Instrum. Meth.*, A506:250–303, 2003. 62
- [12] Jiro Arafune, Masafumi Koike, and Joe Sato. CP violation and matter effect in long baseline neutrino oscillation experiments. *Phys. Rev. D*, 56:3093–3099, Sep 1997. 24
- [13] S. Baker and R. D. Cousins. Clarification of the use of Chi-Square and Likelihood Functions in Fits to Histograms. *Nucl. Instrum. Meth.*, A221:437–442, 1983. 49
- [14] T. Campbell. *Measurement of the muon anti-neutrino charged current double differential cross section with no pions in the final state on water using the pi-zero detector at T2K*. PhD thesis, Colorado State University, 2018. 54, 55
- [15] T. Campbell and Others. Analysis of ν_μ Charged Current Inclusive Events in the PØD in Runs 1+2+3+4, Mar 2014. T2K-TN-80 v4. 57
- [16] T. Campbell, E. Reinherz-Aronis, and W. Toki. The ANuMu/NuMu Cross Sections Ratio With the P0D+TPC Samples, 2017. 57, 107
- [17] J-PARC Center. What is J-PARC?, January 2019. <https://j-parc.jp/researcher/en/about/what/index.html>, Accessed on 26 January 2019. 27

-
- [18] A. Chulliat and Others. The US/UK World Magnetic Model for 2015-2020. Technical report, National Geophysical Data Center, NOAA, 2015. 35
- [19] B. T. Cleveland and Others. Measurement of the Solar Electron Neutrino Flux with the Homestake Chlorine Detector. *Astronomical Journal*, 496:505–526, March 1998. 13
- [20] Giampaolo Co'. Random phase approximation and neutrino-nucleus cross sections. *Acta Phys. Polon.*, B37:2235–2242, 2006. 110
- [21] R. Das. *Measurement of NuMu induced charged current inclusive cross section on water using the near detector of the T2K experiment*. PhD thesis, Colorado State University, Fort Collins, CO., 2016. 54, 56
- [22] A. de Gouvea et al. Working Group Report: Neutrinos. In *Proceedings, 2013 Community Summer Study on the Future of U.S. Particle Physics: Snowmass on the Mississippi*, 2013. arXiv:1310.4340. 21
- [23] I. Esteban et al. Global analysis of three-flavour neutrino oscillations: synergies and tensions in the determination of θ_{23} , δ_{CP} , and the mass ordering. 2018. arXiv:1811.05487. 23
- [24] A. Ferrero. The ND280 Near Detector of the T2K Experiment. *AIP Conference Proceedings*, 1189(1):77–82, 2009. 25
- [25] J. A. Formaggio and G. P. Zeller. From eV to EeV: Neutrino Cross Sections Across Energy Scales. *Rev. Mod. Phys.*, 84:1307–1341, 2012. 45
- [26] S. Fukuda et al. The Super-Kamiokande detector. *Nuclear Instruments and Methods in Physics Research Section A: Accelerators, Spectrometers, Detectors and Associated Equipment*, 501(2):418 – 462, 2003. 25
- [27] Tomasz Golan, Cezary Juszczak, and Jan T. Sobczyk. Final State Interactions Effects in Neutrino-Nucleus Interactions. *Phys. Rev. C*, 86:015505, 2012. 110

-
- [28] M. Hartz and Others. Constraining the Flux and Cross Section Models with Data from the ND280 Detector for the 2014/15 Oscillation Analysis, May 2015. T2K-TN-220 v4. 47, 50
- [29] Y. Hayato. A neutrino interaction simulation program library NEUT. *Acta Phys. Polon.*, B40:2477–2489, 2009. 45
- [30] Susumu Igarashi. Recent Progress of J-PARC MR Beam Commissioning and Operation. In *Proceedings, 57th ICFA Advanced Beam Dynamics Workshop on High-Intensity and High-Brightness Hadron Beams (HB2016): Malmö, Sweden, July 3-8, 2016*, page MOAM6P60, 2016. 28
- [31] C. Jarlskog. A Basis Independent Formulation of the Connection Between Quark Mass Matrices, CP Violation and Experiment,. *Z. Phys.*, C29:491–497, 1985. 22
- [32] E. Komatsu and Others. Seven-year Wilkinson Microwave Anisotropy Probe (WMAP) Observations: Cosmological Interpretation. *Astrophys. J.*, 192:18, February 2011. 24
- [33] C. H. Llewellyn Smith. Neutrino Reactions at Accelerator Energies. *Phys. Rept.*, 3:261–379, 1972. 108
- [34] Z Maki, M. Nakagawa, and S. Sakata. Remarks on the Unified Model of Elementary Particles. *Progr. Theor. Exp. Phys.*, 28(5), 1962. 19
- [35] M. Martini, M. Ericson, G. Chanfray, and J. Marteau. A Unified approach for nucleon knock-out, coherent and incoherent pion production in neutrino interactions with nuclei. *Phys. Rev.*, C80:065501, 2009. 109
- [36] Kajetan Niewczas and Jan T. Sobczyk. Search for nucleon-nucleon correlations in neutrino-argon scattering. *Phys. Rev.*, C93(3):035502, 2016. 109
- [37] B. Pontecorvo. Inverse Beta Processes and Nonconservation of Lepton Charge. *J. Exp. Theor. Phys.*, 28(5), 1957. 19

-
- [38] B. Pontecorvo. Mesonium and Anti-Mesonium. *Sov. Phys. JETP*, 6:429, 1957. 14
- [39] Dieter Rein and Lalit M Sehgal. Neutrino-excitation of baryon resonances and single pion production. *Ann. Phys.*, 133(1):79–153, 1981. 109
- [40] P. K. Saha et al. Simulation, measurement, and mitigation of beam instability caused by the kicker impedance in the 3-GeV rapid cycling synchrotron at the Japan Proton Accelerator Research Complex. *Phys. Rev. Accel. Beams*, 21:024203, Feb 2018. 28
- [41] Andrei D Sakharov. Violation of CP invariance, C asymmetry, and baryon asymmetry of the universe. *Soviet Physics Uspekhi*, 34(5):392, 1991. 25
- [42] J. Schechter and J. W. F. Valle. Neutrinoless double- β decay in $SU(2) \times U(1)$ theories. *Phys. Rev. D*, 25:2951–2954, 1982. 20
- [43] N. Schmitz. *Neutrinophysik*. Teubner, Stuttgart, 1997. 18
- [44] T. Sekiguchi et al. Development and operational experience of magnetic horn system for T2K experiment. *Nuclear Instruments and Methods in Physics Research Section A: Accelerators, Spectrometers, Detectors and Associated Equipment*, 789:57 – 80, 2015. 29
- [45] M. Tanabashi et al. The Review of Particle Physics. *Phys. Rev. D*, 98(030001), 2018. 19, 23
- [46] Peter von Ballmoos. Antimatter in the Universe: constraints from gamma-ray astronomy. *Hyperfine Interactions*, 228(1):91–100, Oct 2014. 25
- [47] G. Welch and G. Bishop. An Introduction to the Kalman Filter. Technical Report 95041, University of North Carolina at Chapel Hill, Chapel Hill, NC 27599-3175, 7 2006. A description of the mathematics involved in the Kalman filer. 55
- [48] L. Wolfenstein. Neutrino oscillations in matter. *Phys. Rev. D*, 17:2369–2374, May 1978. 23

-
-
- [49] Y. Yamazaki, editor. *Accelerator technical design report for high-intensity proton accelerator facility project, J-PARC*. Number 2002-013. Japan Atomic Energy Research Institute, 2003. 28
 - [50] Kai Zuber. *Neutrino Physics*. CRC Press, Boca Raton, FL., 2nd edition, 2012. 1, 13, 18

Appendix A

The PØD-Only Bin Normalization Parameters

The observable normalizations used in the PØD-only BANFF fit are tabulated here.

Table A.1: Observable normalization fit bins.

Fit Index	Sample	p [GeV/c]	$\cos\theta$	Prefit
100	ν_μ 1-Trk Wtr	$0 \leq p < 0.40$	$-1 \leq \cos\theta < 0.70$	1.21 ± 0.67
101		$0.40 \leq p < 0.60$	$-1 \leq \cos\theta < 0.70$	0.87 ± 0.18
102		$0.60 \leq p < 0.80$	$-1 \leq \cos\theta < 0.70$	1.12 ± 0.44
103		$0.80 \leq p < 1.25$	$-1 \leq \cos\theta < 0.70$	1.13 ± 0.43
104		$1.25 \leq p < 2.00$	$-1 \leq \cos\theta < 0.70$	1.02 ± 0.17
105		$2.00 \leq p < 3.00$	$-1 \leq \cos\theta < 0.70$	0.93 ± 0.20
106		$3.00 \leq p < 4.00$	$-1 \leq \cos\theta < 0.70$	1.00 ± 0.28
107		$4.00 \leq p < 5.50$	$-1 \leq \cos\theta < 0.70$	0.82 ± 0.33
108		$5.50 \leq p < 30$	$-1 \leq \cos\theta < 0.70$	1.26 ± 0.58
109		$0 \leq p < 0.40$	$0.70 \leq \cos\theta < 0.80$	1.27 ± 0.74
110	ν_μ 1-Trk Wtr	$0.40 \leq p < 0.60$	$0.70 \leq \cos\theta < 0.80$	0.89 ± 0.18
111		$0.60 \leq p < 0.80$	$0.70 \leq \cos\theta < 0.80$	1.02 ± 0.27

Table A.1: Observable normalization fit bins.

Fit Index	Sample	p [GeV/c]	$\cos\theta$	Prefit
112		$0.80 \leq p < 1.25$	$0.70 \leq \cos\theta < 0.80$	1.09 ± 0.33
113		$1.25 \leq p < 2.00$	$0.70 \leq \cos\theta < 0.80$	1.02 ± 0.17
114		$2.00 \leq p < 3.00$	$0.70 \leq \cos\theta < 0.80$	0.96 ± 0.15
115		$3.00 \leq p < 4.00$	$0.70 \leq \cos\theta < 0.80$	0.99 ± 0.21
116		$4.00 \leq p < 5.50$	$0.70 \leq \cos\theta < 0.80$	0.94 ± 0.29
117		$5.50 \leq p < 30$	$0.70 \leq \cos\theta < 0.80$	1.05 ± 0.53
118		$0 \leq p < 0.40$	$0.80 \leq \cos\theta < 0.94$	1.33 ± 0.78
119		$0.40 \leq p < 0.60$	$0.80 \leq \cos\theta < 0.94$	0.91 ± 0.21
120	ν_μ 1-Trk Wtr	$0.60 \leq p < 0.80$	$0.80 \leq \cos\theta < 0.94$	0.97 ± 0.14
121		$0.80 \leq p < 1.25$	$0.80 \leq \cos\theta < 0.94$	1.03 ± 0.17
122		$1.25 \leq p < 2.00$	$0.80 \leq \cos\theta < 0.94$	1.01 ± 0.09
123		$2.00 \leq p < 3.00$	$0.80 \leq \cos\theta < 0.94$	1.00 ± 0.05
124		$3.00 \leq p < 4.00$	$0.80 \leq \cos\theta < 0.94$	1.00 ± 0.12
125		$4.00 \leq p < 5.50$	$0.80 \leq \cos\theta < 0.94$	0.95 ± 0.15
126		$5.50 \leq p < 30$	$0.80 \leq \cos\theta < 0.94$	0.96 ± 0.38
127		$0 \leq p < 0.40$	$0.94 \leq \cos\theta < 0.97$	1.29 ± 0.73
128		$0.40 \leq p < 0.60$	$0.94 \leq \cos\theta < 0.97$	0.93 ± 0.22
129		$0.60 \leq p < 0.80$	$0.94 \leq \cos\theta < 0.97$	0.96 ± 0.09
130	ν_μ 1-Trk Wtr	$0.80 \leq p < 1.25$	$0.94 \leq \cos\theta < 0.97$	1.02 ± 0.11
131		$1.25 \leq p < 2.00$	$0.94 \leq \cos\theta < 0.97$	1.00 ± 0.07
132		$2.00 \leq p < 3.00$	$0.94 \leq \cos\theta < 0.97$	1.00 ± 0.03
133		$3.00 \leq p < 4.00$	$0.94 \leq \cos\theta < 0.97$	0.99 ± 0.08
134		$4.00 \leq p < 5.50$	$0.94 \leq \cos\theta < 0.97$	1.00 ± 0.14
135		$5.50 \leq p < 30$	$0.94 \leq \cos\theta < 0.97$	0.99 ± 0.20
136		$0 \leq p < 0.40$	$0.97 \leq \cos\theta < 0.99$	1.25 ± 0.65

Table A.1: Observable normalization fit bins.

Fit Index	Sample	p [GeV/c]	$\cos\theta$	Prefit
137		$0.40 \leq p < 0.60$	$0.97 \leq \cos\theta < 0.99$	0.94 ± 0.20
138		$0.60 \leq p < 0.80$	$0.97 \leq \cos\theta < 0.99$	0.95 ± 0.08
139		$0.80 \leq p < 1.25$	$0.97 \leq \cos\theta < 0.99$	1.01 ± 0.11
140	ν_μ 1-Trk Wtr	$1.25 \leq p < 2.00$	$0.97 \leq \cos\theta < 0.99$	1.00 ± 0.07
141		$2.00 \leq p < 3.00$	$0.97 \leq \cos\theta < 0.99$	1.00 ± 0.06
142		$3.00 \leq p < 4.00$	$0.97 \leq \cos\theta < 0.99$	1.00 ± 0.03
143		$4.00 \leq p < 5.50$	$0.97 \leq \cos\theta < 0.99$	0.98 ± 0.10
144		$5.50 \leq p < 30$	$0.97 \leq \cos\theta < 0.99$	0.97 ± 0.14
145		$0 \leq p < 0.40$	$0.99 \leq \cos\theta < 1$	1.25 ± 0.58
146		$0.40 \leq p < 0.60$	$0.99 \leq \cos\theta < 1$	0.93 ± 0.18
147		$0.60 \leq p < 0.80$	$0.99 \leq \cos\theta < 1$	0.96 ± 0.11
148		$0.80 \leq p < 1.25$	$0.99 \leq \cos\theta < 1$	1.01 ± 0.11
149		$1.25 \leq p < 2.00$	$0.99 \leq \cos\theta < 1$	1.01 ± 0.08
150	ν_μ 1-Trk Wtr	$2.00 \leq p < 3.00$	$0.99 \leq \cos\theta < 1$	1.01 ± 0.10
151		$3.00 \leq p < 4.00$	$0.99 \leq \cos\theta < 1$	1.00 ± 0.06
152		$4.00 \leq p < 5.50$	$0.99 \leq \cos\theta < 1$	1.00 ± 0.05
153		$5.50 \leq p < 30$	$0.99 \leq \cos\theta < 1$	0.98 ± 0.10
154	ν_μ N-Trks Wtr	$0 \leq p < 0.40$	$-1 \leq \cos\theta < 0.77$	1.18 ± 0.61
155		$0.40 \leq p < 0.60$	$-1 \leq \cos\theta < 0.77$	0.89 ± 0.15
156		$0.60 \leq p < 0.80$	$-1 \leq \cos\theta < 0.77$	1.01 ± 0.16
157		$0.80 \leq p < 1.20$	$-1 \leq \cos\theta < 0.77$	1.03 ± 0.19
158		$1.20 \leq p < 2.20$	$-1 \leq \cos\theta < 0.77$	1.02 ± 0.15
159		$2.20 \leq p < 3.50$	$-1 \leq \cos\theta < 0.77$	1.04 ± 0.16
160	ν_μ N-Trks Wtr	$3.50 \leq p < 10.0$	$-1 \leq \cos\theta < 0.77$	0.93 ± 0.26
161		$10.0 \leq p < 30$	$-1 \leq \cos\theta < 0.77$	0.94 ± 0.67

Table A.1: Observable normalization fit bins.

Fit Index	Sample	p [GeV/c]	$\cos\theta$	Prefit
162		$0 \leq p < 0.40$	$0.77 \leq \cos\theta < 0.85$	1.13 ± 0.56
163		$0.40 \leq p < 0.60$	$0.77 \leq \cos\theta < 0.85$	0.92 ± 0.15
164		$0.60 \leq p < 0.80$	$0.77 \leq \cos\theta < 0.85$	0.98 ± 0.07
165		$0.80 \leq p < 1.20$	$0.77 \leq \cos\theta < 0.85$	1.00 ± 0.09
166		$1.20 \leq p < 2.20$	$0.77 \leq \cos\theta < 0.85$	1.01 ± 0.08
167		$2.20 \leq p < 3.50$	$0.77 \leq \cos\theta < 0.85$	1.01 ± 0.06
168		$3.50 \leq p < 10.0$	$0.77 \leq \cos\theta < 0.85$	0.98 ± 0.16
169		$10.0 \leq p < 30$	$0.77 \leq \cos\theta < 0.85$	0.98 ± 0.52
170	ν_μ N-Trks Wtr	$0 \leq p < 0.40$	$0.85 \leq \cos\theta < 0.90$	1.13 ± 0.53
171		$0.40 \leq p < 0.60$	$0.85 \leq \cos\theta < 0.90$	0.92 ± 0.14
172		$0.60 \leq p < 0.80$	$0.85 \leq \cos\theta < 0.90$	0.98 ± 0.05
173		$0.80 \leq p < 1.20$	$0.85 \leq \cos\theta < 0.90$	1.00 ± 0.07
174		$1.20 \leq p < 2.20$	$0.85 \leq \cos\theta < 0.90$	1.00 ± 0.06
175		$2.20 \leq p < 3.50$	$0.85 \leq \cos\theta < 0.90$	1.01 ± 0.05
176		$3.50 \leq p < 10.0$	$0.85 \leq \cos\theta < 0.90$	0.99 ± 0.12
177		$10.0 \leq p < 30$	$0.85 \leq \cos\theta < 0.90$	1.03 ± 0.46
178		$0 \leq p < 0.40$	$0.90 \leq \cos\theta < 0.97$	1.13 ± 0.52
179		$0.40 \leq p < 0.60$	$0.90 \leq \cos\theta < 0.97$	0.94 ± 0.13
180	ν_μ N-Trks Wtr	$0.60 \leq p < 0.80$	$0.90 \leq \cos\theta < 0.97$	0.97 ± 0.06
181		$0.80 \leq p < 1.20$	$0.90 \leq \cos\theta < 0.97$	0.99 ± 0.08
182		$1.20 \leq p < 2.20$	$0.90 \leq \cos\theta < 0.97$	1.00 ± 0.07
183		$2.20 \leq p < 3.50$	$0.90 \leq \cos\theta < 0.97$	1.00 ± 0.03
184		$3.50 \leq p < 10.0$	$0.90 \leq \cos\theta < 0.97$	0.99 ± 0.10
185		$10.0 \leq p < 30$	$0.90 \leq \cos\theta < 0.97$	0.98 ± 0.25
186		$0 \leq p < 0.40$	$0.97 \leq \cos\theta < 1$	1.09 ± 0.47

Table A.1: Observable normalization fit bins.

Fit Index	Sample	p [GeV/c]	$\cos\theta$	Prefit
187		$0.40 \leq p < 0.60$	$0.97 \leq \cos\theta < 1$	0.96 ± 0.11
188		$0.60 \leq p < 0.80$	$0.97 \leq \cos\theta < 1$	0.96 ± 0.09
189		$0.80 \leq p < 1.20$	$0.97 \leq \cos\theta < 1$	1.00 ± 0.09
190	ν_μ N-Trks Wtr	$1.20 \leq p < 2.20$	$0.97 \leq \cos\theta < 1$	1.01 ± 0.09
191		$2.20 \leq p < 3.50$	$0.97 \leq \cos\theta < 1$	1.01 ± 0.08
192		$3.50 \leq p < 10.0$	$0.97 \leq \cos\theta < 1$	0.99 ± 0.05
193		$10.0 \leq p < 30$	$0.97 \leq \cos\theta < 1$	0.97 ± 0.13
194	$\bar{\nu}_\mu$ RHC 1-Trk Wtr	$0 \leq p < 0.50$	$-1 \leq \cos\theta < 0.82$	1.00 ± 0.36
195		$0.50 \leq p < 0.60$	$-1 \leq \cos\theta < 0.82$	0.90 ± 0.15
196		$0.60 \leq p < 0.80$	$-1 \leq \cos\theta < 0.82$	1.05 ± 0.26
197		$0.80 \leq p < 1.25$	$-1 \leq \cos\theta < 0.82$	1.04 ± 0.20
198		$1.25 \leq p < 2.00$	$-1 \leq \cos\theta < 0.82$	1.00 ± 0.17
199		$2.00 \leq p < 3.00$	$-1 \leq \cos\theta < 0.82$	1.01 ± 0.17
200	$\bar{\nu}_\mu$ RHC 1-Trk Wtr	$3.00 \leq p < 30$	$-1 \leq \cos\theta < 0.82$	1.00 ± 0.39
201		$0 \leq p < 0.50$	$0.82 \leq \cos\theta < 0.90$	1.06 ± 0.43
202		$0.50 \leq p < 0.60$	$0.82 \leq \cos\theta < 0.90$	0.91 ± 0.13
203		$0.60 \leq p < 0.80$	$0.82 \leq \cos\theta < 0.90$	0.97 ± 0.16
204		$0.80 \leq p < 1.25$	$0.82 \leq \cos\theta < 0.90$	1.04 ± 0.17
205		$1.25 \leq p < 2.00$	$0.82 \leq \cos\theta < 0.90$	1.00 ± 0.11
206		$2.00 \leq p < 3.00$	$0.82 \leq \cos\theta < 0.90$	0.99 ± 0.11
207		$3.00 \leq p < 30$	$0.82 \leq \cos\theta < 0.90$	0.92 ± 0.28
208		$0 \leq p < 0.50$	$0.90 \leq \cos\theta < 0.95$	1.07 ± 0.44
209		$0.50 \leq p < 0.60$	$0.90 \leq \cos\theta < 0.95$	0.93 ± 0.14
210	$\bar{\nu}_\mu$ RHC 1-Trk Wtr	$0.60 \leq p < 0.80$	$0.90 \leq \cos\theta < 0.95$	0.96 ± 0.11
211		$0.80 \leq p < 1.25$	$0.90 \leq \cos\theta < 0.95$	1.03 ± 0.14

Table A.1: Observable normalization fit bins.

Fit Index	Sample	p [GeV/c]	$\cos\theta$	Prefit
212		$1.25 \leq p < 2.00$	$0.90 \leq \cos\theta < 0.95$	1.01 ± 0.08
213		$2.00 \leq p < 3.00$	$0.90 \leq \cos\theta < 0.95$	0.98 ± 0.06
214		$3.00 \leq p < 30$	$0.90 \leq \cos\theta < 0.95$	0.95 ± 0.17
215		$0 \leq p < 0.50$	$0.95 \leq \cos\theta < 0.99$	1.08 ± 0.45
216		$0.50 \leq p < 0.60$	$0.95 \leq \cos\theta < 0.99$	0.93 ± 0.16
217		$0.60 \leq p < 0.80$	$0.95 \leq \cos\theta < 0.99$	0.96 ± 0.09
218		$0.80 \leq p < 1.25$	$0.95 \leq \cos\theta < 0.99$	1.02 ± 0.12
219		$1.25 \leq p < 2.00$	$0.95 \leq \cos\theta < 0.99$	1.01 ± 0.07
220	$\bar{\nu}_\mu$ RHC 1-Trk Wtr	$2.00 \leq p < 3.00$	$0.95 \leq \cos\theta < 0.99$	1.00 ± 0.04
221		$3.00 \leq p < 30$	$0.95 \leq \cos\theta < 0.99$	0.98 ± 0.09
222		$0 \leq p < 0.50$	$0.99 \leq \cos\theta < 1$	1.09 ± 0.43
223		$0.50 \leq p < 0.60$	$0.99 \leq \cos\theta < 1$	0.94 ± 0.15
224		$0.60 \leq p < 0.80$	$0.99 \leq \cos\theta < 1$	0.93 ± 0.10
225		$0.80 \leq p < 1.25$	$0.99 \leq \cos\theta < 1$	1.02 ± 0.12
226		$1.25 \leq p < 2.00$	$0.99 \leq \cos\theta < 1$	1.01 ± 0.08
227		$2.00 \leq p < 3.00$	$0.99 \leq \cos\theta < 1$	1.00 ± 0.07
228		$3.00 \leq p < 30$	$0.99 \leq \cos\theta < 1$	0.99 ± 0.05
229	$\bar{\nu}_\mu$ RHC N-Trks Wtr	$0 \leq p < 0.50$	$-1 \leq \cos\theta < 0.89$	1.02 ± 0.34
230		$0.50 \leq p < 0.90$	$-1 \leq \cos\theta < 0.89$	1.00 ± 0.09
231		$0.90 \leq p < 1.25$	$-1 \leq \cos\theta < 0.89$	1.01 ± 0.07
232		$1.25 \leq p < 1.60$	$-1 \leq \cos\theta < 0.89$	0.99 ± 0.13
233		$1.60 \leq p < 3.00$	$-1 \leq \cos\theta < 0.89$	0.99 ± 0.11
234		$3.00 \leq p < 30$	$-1 \leq \cos\theta < 0.89$	0.98 ± 0.33
235		$0 \leq p < 0.50$	$0.89 \leq \cos\theta < 0.95$	1.05 ± 0.34
236		$0.50 \leq p < 0.90$	$0.89 \leq \cos\theta < 0.95$	0.97 ± 0.05

Table A.1: Observable normalization fit bins.

Fit Index	Sample	p [GeV/c]	$\cos\theta$	Prefit
237		$0.90 \leq p < 1.25$	$0.89 \leq \cos\theta < 0.95$	1.02 ± 0.06
238		$1.25 \leq p < 1.60$	$0.89 \leq \cos\theta < 0.95$	0.98 ± 0.09
239		$1.60 \leq p < 3.00$	$0.89 \leq \cos\theta < 0.95$	0.99 ± 0.06
240	$\bar{\nu}_\mu$ RHC N-Trks Wtr	$3.00 \leq p < 30$	$0.89 \leq \cos\theta < 0.95$	0.98 ± 0.14
241		$0 \leq p < 0.50$	$0.95 \leq \cos\theta < 0.97$	1.04 ± 0.36
242		$0.50 \leq p < 0.90$	$0.95 \leq \cos\theta < 0.97$	0.97 ± 0.05
243		$0.90 \leq p < 1.25$	$0.95 \leq \cos\theta < 0.97$	1.01 ± 0.05
244		$1.25 \leq p < 1.60$	$0.95 \leq \cos\theta < 0.97$	1.00 ± 0.09
245		$1.60 \leq p < 3.00$	$0.95 \leq \cos\theta < 0.97$	1.01 ± 0.06
246		$3.00 \leq p < 30$	$0.95 \leq \cos\theta < 0.97$	0.98 ± 0.12
247		$0 \leq p < 0.50$	$0.97 \leq \cos\theta < 0.99$	1.03 ± 0.37
248		$0.50 \leq p < 0.90$	$0.97 \leq \cos\theta < 0.99$	1.01 ± 0.05
249		$0.90 \leq p < 1.25$	$0.97 \leq \cos\theta < 0.99$	1.00 ± 0.05
250	$\bar{\nu}_\mu$ RHC N-Trks Wtr	$1.25 \leq p < 1.60$	$0.97 \leq \cos\theta < 0.99$	0.99 ± 0.07
251		$1.60 \leq p < 3.00$	$0.97 \leq \cos\theta < 0.99$	1.01 ± 0.07
252		$3.00 \leq p < 30$	$0.97 \leq \cos\theta < 0.99$	0.99 ± 0.07
253		$0 \leq p < 0.50$	$0.99 \leq \cos\theta < 1$	1.07 ± 0.39
254		$0.50 \leq p < 0.90$	$0.99 \leq \cos\theta < 1$	0.98 ± 0.07
255		$0.90 \leq p < 1.25$	$0.99 \leq \cos\theta < 1$	1.02 ± 0.08
256		$1.25 \leq p < 1.60$	$0.99 \leq \cos\theta < 1$	1.01 ± 0.08
257		$1.60 \leq p < 3.00$	$0.99 \leq \cos\theta < 1$	0.99 ± 0.09
258		$3.00 \leq p < 30$	$0.99 \leq \cos\theta < 1$	0.99 ± 0.06
259	ν_μ RHC 1-Trk Wtr	$0 \leq p < 0.40$	$-1 \leq \cos\theta < 0.78$	1.24 ± 0.60
260		$0.40 \leq p < 0.60$	$-1 \leq \cos\theta < 0.78$	0.91 ± 0.16
261		$0.60 \leq p < 0.80$	$-1 \leq \cos\theta < 0.78$	1.00 ± 0.13

Table A.1: Observable normalization fit bins.

Fit Index	Sample	p [GeV/c]	$\cos\theta$	Prefit
262		$0.80 \leq p < 1.10$	$-1 \leq \cos\theta < 0.78$	1.02 ± 0.21
263		$1.10 \leq p < 2.00$	$-1 \leq \cos\theta < 0.78$	1.03 ± 0.17
264		$2.00 \leq p < 10.0$	$-1 \leq \cos\theta < 0.78$	0.99 ± 0.21
265		$0 \leq p < 0.40$	$0.78 \leq \cos\theta < 0.84$	1.27 ± 0.64
266		$0.40 \leq p < 0.60$	$0.78 \leq \cos\theta < 0.84$	0.95 ± 0.16
267		$0.60 \leq p < 0.80$	$0.78 \leq \cos\theta < 0.84$	0.99 ± 0.06
268		$0.80 \leq p < 1.10$	$0.78 \leq \cos\theta < 0.84$	0.98 ± 0.11
269		$1.10 \leq p < 2.00$	$0.78 \leq \cos\theta < 0.84$	1.04 ± 0.14
270	ν_μ RHC 1-Trk Wtr	$2.00 \leq p < 10.0$	$0.78 \leq \cos\theta < 0.84$	0.99 ± 0.16
271		$0 \leq p < 0.40$	$0.84 \leq \cos\theta < 0.92$	1.20 ± 0.60
272		$0.40 \leq p < 0.60$	$0.84 \leq \cos\theta < 0.92$	0.95 ± 0.20
273		$0.60 \leq p < 0.80$	$0.84 \leq \cos\theta < 0.92$	0.97 ± 0.07
274		$0.80 \leq p < 1.10$	$0.84 \leq \cos\theta < 0.92$	1.00 ± 0.08
275		$1.10 \leq p < 2.00$	$0.84 \leq \cos\theta < 0.92$	1.00 ± 0.08
276		$2.00 \leq p < 10.0$	$0.84 \leq \cos\theta < 0.92$	1.00 ± 0.10
277		$0 \leq p < 0.40$	$0.92 \leq \cos\theta < 0.95$	1.10 ± 0.52
278		$0.40 \leq p < 0.60$	$0.92 \leq \cos\theta < 0.95$	0.99 ± 0.16
279		$0.60 \leq p < 0.80$	$0.92 \leq \cos\theta < 0.95$	0.95 ± 0.06
280	ν_μ RHC 1-Trk Wtr	$0.80 \leq p < 1.10$	$0.92 \leq \cos\theta < 0.95$	0.99 ± 0.04
281		$1.10 \leq p < 2.00$	$0.92 \leq \cos\theta < 0.95$	1.00 ± 0.07
282		$2.00 \leq p < 10.0$	$0.92 \leq \cos\theta < 0.95$	1.00 ± 0.06
283		$0 \leq p < 0.40$	$0.95 \leq \cos\theta < 0.98$	1.19 ± 0.50
284		$0.40 \leq p < 0.60$	$0.95 \leq \cos\theta < 0.98$	0.98 ± 0.15
285		$0.60 \leq p < 0.80$	$0.95 \leq \cos\theta < 0.98$	0.96 ± 0.09
286		$0.80 \leq p < 1.10$	$0.95 \leq \cos\theta < 0.98$	0.99 ± 0.07

Table A.1: Observable normalization fit bins.

Fit Index	Sample	p [GeV/c]	$\cos\theta$	Prefit
287		$1.10 \leq p < 2.00$	$0.95 \leq \cos\theta < 0.98$	1.00 ± 0.06
288		$2.00 \leq p < 10.0$	$0.95 \leq \cos\theta < 0.98$	1.00 ± 0.04
289		$0 \leq p < 0.40$	$0.98 \leq \cos\theta < 0.99$	1.12 ± 0.46
290	ν_μ RHC 1-Trk Wtr	$0.40 \leq p < 0.60$	$0.98 \leq \cos\theta < 0.99$	1.01 ± 0.15
291		$0.60 \leq p < 0.80$	$0.98 \leq \cos\theta < 0.99$	0.98 ± 0.09
292		$0.80 \leq p < 1.10$	$0.98 \leq \cos\theta < 0.99$	1.00 ± 0.09
293		$1.10 \leq p < 2.00$	$0.98 \leq \cos\theta < 0.99$	0.98 ± 0.07
294		$2.00 \leq p < 10.0$	$0.98 \leq \cos\theta < 0.99$	1.00 ± 0.03
295		$0 \leq p < 0.40$	$0.99 \leq \cos\theta < 1$	1.29 ± 0.47
296		$0.40 \leq p < 0.60$	$0.99 \leq \cos\theta < 1$	0.98 ± 0.20
297		$0.60 \leq p < 0.80$	$0.99 \leq \cos\theta < 1$	0.95 ± 0.16
298		$0.80 \leq p < 1.10$	$0.99 \leq \cos\theta < 1$	1.03 ± 0.10
299		$1.10 \leq p < 2.00$	$0.99 \leq \cos\theta < 1$	1.01 ± 0.08
300	ν_μ RHC 1-Trk Wtr	$2.00 \leq p < 10.0$	$0.99 \leq \cos\theta < 1$	1.00 ± 0.03
301	ν_μ RHC N-Trks Wtr	$0 \leq p < 0.60$	$-1 \leq \cos\theta < 0.70$	0.97 ± 0.21
302		$0.60 \leq p < 1.00$	$-1 \leq \cos\theta < 0.70$	1.01 ± 0.13
303		$1.00 \leq p < 1.50$	$-1 \leq \cos\theta < 0.70$	1.01 ± 0.15
304		$1.50 \leq p < 2.00$	$-1 \leq \cos\theta < 0.70$	1.15 ± 0.19
305		$2.00 \leq p < 10.0$	$-1 \leq \cos\theta < 0.70$	0.95 ± 0.23
306		$0 \leq p < 0.60$	$0.70 \leq \cos\theta < 0.80$	1.00 ± 0.26
307		$0.60 \leq p < 1.00$	$0.70 \leq \cos\theta < 0.80$	0.99 ± 0.08
308		$1.00 \leq p < 1.50$	$0.70 \leq \cos\theta < 0.80$	1.01 ± 0.11
309		$1.50 \leq p < 2.00$	$0.70 \leq \cos\theta < 0.80$	0.98 ± 0.09
310	ν_μ RHC N-Trks Wtr	$2.00 \leq p < 10.0$	$0.70 \leq \cos\theta < 0.80$	1.00 ± 0.16
311		$0 \leq p < 0.60$	$0.80 \leq \cos\theta < 0.85$	1.01 ± 0.28

Table A.1: Observable normalization fit bins.

Fit Index	Sample	p [GeV/c]	$\cos\theta$	Prefit
312		$0.60 \leq p < 1.00$	$0.80 \leq \cos\theta < 0.85$	0.98 ± 0.06
313		$1.00 \leq p < 1.50$	$0.80 \leq \cos\theta < 0.85$	1.00 ± 0.08
314		$1.50 \leq p < 2.00$	$0.80 \leq \cos\theta < 0.85$	1.02 ± 0.08
315		$2.00 \leq p < 10.0$	$0.80 \leq \cos\theta < 0.85$	0.98 ± 0.11
316		$0 \leq p < 0.60$	$0.85 \leq \cos\theta < 0.98$	1.02 ± 0.25
317		$0.60 \leq p < 1.00$	$0.85 \leq \cos\theta < 0.98$	0.98 ± 0.07
318		$1.00 \leq p < 1.50$	$0.85 \leq \cos\theta < 0.98$	1.00 ± 0.07
319		$1.50 \leq p < 2.00$	$0.85 \leq \cos\theta < 0.98$	1.00 ± 0.07
320	ν_μ RHC N-Trks Wtr	$2.00 \leq p < 10.0$	$0.85 \leq \cos\theta < 0.98$	1.00 ± 0.06
321		$0 \leq p < 0.60$	$0.98 \leq \cos\theta < 0.99$	1.02 ± 0.24
322		$0.60 \leq p < 1.00$	$0.98 \leq \cos\theta < 0.99$	0.96 ± 0.10
323		$1.00 \leq p < 1.50$	$0.98 \leq \cos\theta < 0.99$	1.01 ± 0.09
324		$1.50 \leq p < 2.00$	$0.98 \leq \cos\theta < 0.99$	0.99 ± 0.09
325		$2.00 \leq p < 10.0$	$0.98 \leq \cos\theta < 0.99$	0.99 ± 0.04
326		$0 \leq p < 0.60$	$0.99 \leq \cos\theta < 1$	1.00 ± 0.25
327		$0.60 \leq p < 1.00$	$0.99 \leq \cos\theta < 1$	0.98 ± 0.11
328		$1.00 \leq p < 1.50$	$0.99 \leq \cos\theta < 1$	1.00 ± 0.09
329		$1.50 \leq p < 2.00$	$0.99 \leq \cos\theta < 1$	1.01 ± 0.10
330	ν_μ RHC N-Trks Wtr	$2.00 \leq p < 10.0$	$0.99 \leq \cos\theta < 1$	1.00 ± 0.04
331	ν_μ 1-Trk Air	$0 \leq p < 0.40$	$-1 \leq \cos\theta < 0.70$	1.17 ± 0.66
332		$0.40 \leq p < 0.60$	$-1 \leq \cos\theta < 0.70$	0.86 ± 0.19
333		$0.60 \leq p < 0.80$	$-1 \leq \cos\theta < 0.70$	1.17 ± 0.53
334		$0.80 \leq p < 1.25$	$-1 \leq \cos\theta < 0.70$	1.15 ± 0.44
335		$1.25 \leq p < 2.00$	$-1 \leq \cos\theta < 0.70$	0.97 ± 0.19
336		$2.00 \leq p < 3.00$	$-1 \leq \cos\theta < 0.70$	1.02 ± 0.19

Table A.1: Observable normalization fit bins.

Fit Index	Sample	p [GeV/c]	$\cos\theta$	Prefit
337		$3.00 \leq p < 4.00$	$-1 \leq \cos\theta < 0.70$	1.02 ± 0.31
338		$4.00 \leq p < 5.50$	$-1 \leq \cos\theta < 0.70$	0.97 ± 0.37
339		$5.50 \leq p < 30$	$-1 \leq \cos\theta < 0.70$	0.88 ± 0.62
340	ν_μ 1-Trk Air	$0 \leq p < 0.40$	$0.70 \leq \cos\theta < 0.80$	1.27 ± 0.75
341		$0.40 \leq p < 0.60$	$0.70 \leq \cos\theta < 0.80$	0.87 ± 0.17
342		$0.60 \leq p < 0.80$	$0.70 \leq \cos\theta < 0.80$	1.04 ± 0.31
343		$0.80 \leq p < 1.25$	$0.70 \leq \cos\theta < 0.80$	1.09 ± 0.34
344		$1.25 \leq p < 2.00$	$0.70 \leq \cos\theta < 0.80$	1.01 ± 0.18
345		$2.00 \leq p < 3.00$	$0.70 \leq \cos\theta < 0.80$	1.03 ± 0.17
346		$3.00 \leq p < 4.00$	$0.70 \leq \cos\theta < 0.80$	0.94 ± 0.27
347		$4.00 \leq p < 5.50$	$0.70 \leq \cos\theta < 0.80$	0.93 ± 0.38
348		$5.50 \leq p < 30$	$0.70 \leq \cos\theta < 0.80$	1.00 ± 0.58
349		$0 \leq p < 0.40$	$0.80 \leq \cos\theta < 0.94$	1.32 ± 0.79
350	ν_μ 1-Trk Air	$0.40 \leq p < 0.60$	$0.80 \leq \cos\theta < 0.94$	0.90 ± 0.20
351		$0.60 \leq p < 0.80$	$0.80 \leq \cos\theta < 0.94$	0.98 ± 0.17
352		$0.80 \leq p < 1.25$	$0.80 \leq \cos\theta < 0.94$	1.04 ± 0.19
353		$1.25 \leq p < 2.00$	$0.80 \leq \cos\theta < 0.94$	1.01 ± 0.10
354		$2.00 \leq p < 3.00$	$0.80 \leq \cos\theta < 0.94$	1.00 ± 0.07
355		$3.00 \leq p < 4.00$	$0.80 \leq \cos\theta < 0.94$	0.97 ± 0.14
356		$4.00 \leq p < 5.50$	$0.80 \leq \cos\theta < 0.94$	1.06 ± 0.22
357		$5.50 \leq p < 30$	$0.80 \leq \cos\theta < 0.94$	1.00 ± 0.33
358		$0 \leq p < 0.40$	$0.94 \leq \cos\theta < 0.97$	1.29 ± 0.73
359		$0.40 \leq p < 0.60$	$0.94 \leq \cos\theta < 0.97$	0.91 ± 0.20
360	ν_μ 1-Trk Air	$0.60 \leq p < 0.80$	$0.94 \leq \cos\theta < 0.97$	0.97 ± 0.11
361		$0.80 \leq p < 1.25$	$0.94 \leq \cos\theta < 0.97$	1.02 ± 0.12

Table A.1: Observable normalization fit bins.

Fit Index	Sample	p [GeV/c]	$\cos\theta$	Prefit
362		$1.25 \leq p < 2.00$	$0.94 \leq \cos\theta < 0.97$	1.00 ± 0.07
363		$2.00 \leq p < 3.00$	$0.94 \leq \cos\theta < 0.97$	1.01 ± 0.04
364		$3.00 \leq p < 4.00$	$0.94 \leq \cos\theta < 0.97$	0.98 ± 0.09
365		$4.00 \leq p < 5.50$	$0.94 \leq \cos\theta < 0.97$	0.98 ± 0.15
366		$5.50 \leq p < 30$	$0.94 \leq \cos\theta < 0.97$	0.98 ± 0.21
367		$0 \leq p < 0.40$	$0.97 \leq \cos\theta < 0.99$	1.23 ± 0.68
368		$0.40 \leq p < 0.60$	$0.97 \leq \cos\theta < 0.99$	0.91 ± 0.20
369		$0.60 \leq p < 0.80$	$0.97 \leq \cos\theta < 0.99$	0.98 ± 0.12
370	ν_μ 1-Trk Air	$0.80 \leq p < 1.25$	$0.97 \leq \cos\theta < 0.99$	1.02 ± 0.11
371		$1.25 \leq p < 2.00$	$0.97 \leq \cos\theta < 0.99$	0.99 ± 0.08
372		$2.00 \leq p < 3.00$	$0.97 \leq \cos\theta < 0.99$	1.01 ± 0.06
373		$3.00 \leq p < 4.00$	$0.97 \leq \cos\theta < 0.99$	1.00 ± 0.04
374		$4.00 \leq p < 5.50$	$0.97 \leq \cos\theta < 0.99$	0.98 ± 0.11
375		$5.50 \leq p < 30$	$0.97 \leq \cos\theta < 0.99$	0.98 ± 0.15
376		$0 \leq p < 0.40$	$0.99 \leq \cos\theta < 1$	1.21 ± 0.58
377		$0.40 \leq p < 0.60$	$0.99 \leq \cos\theta < 1$	0.90 ± 0.16
378		$0.60 \leq p < 0.80$	$0.99 \leq \cos\theta < 1$	0.99 ± 0.12
379		$0.80 \leq p < 1.25$	$0.99 \leq \cos\theta < 1$	1.02 ± 0.12
380	ν_μ 1-Trk Air	$1.25 \leq p < 2.00$	$0.99 \leq \cos\theta < 1$	1.01 ± 0.09
381		$2.00 \leq p < 3.00$	$0.99 \leq \cos\theta < 1$	1.01 ± 0.10
382		$3.00 \leq p < 4.00$	$0.99 \leq \cos\theta < 1$	1.00 ± 0.06
383		$4.00 \leq p < 5.50$	$0.99 \leq \cos\theta < 1$	1.00 ± 0.05
384		$5.50 \leq p < 30$	$0.99 \leq \cos\theta < 1$	0.98 ± 0.10
385	ν_μ N-Trks Air	$0 \leq p < 0.40$	$-1 \leq \cos\theta < 0.77$	1.18 ± 0.62
386		$0.40 \leq p < 0.60$	$-1 \leq \cos\theta < 0.77$	0.88 ± 0.15

Table A.1: Observable normalization fit bins.

Fit Index	Sample	p [GeV/c]	$\cos\theta$	Prefit
387		$0.60 \leq p < 0.80$	$-1 \leq \cos\theta < 0.77$	1.03 ± 0.21
388		$0.80 \leq p < 1.20$	$-1 \leq \cos\theta < 0.77$	1.03 ± 0.21
389		$1.20 \leq p < 2.20$	$-1 \leq \cos\theta < 0.77$	1.01 ± 0.16
390	ν_μ N-Trks Air	$2.20 \leq p < 3.50$	$-1 \leq \cos\theta < 0.77$	1.00 ± 0.22
391		$3.50 \leq p < 10.0$	$-1 \leq \cos\theta < 0.77$	0.99 ± 0.32
392		$10.0 \leq p < 30$	$-1 \leq \cos\theta < 0.77$	0.93 ± 0.69
393		$0 \leq p < 0.40$	$0.77 \leq \cos\theta < 0.85$	1.13 ± 0.58
394		$0.40 \leq p < 0.60$	$0.77 \leq \cos\theta < 0.85$	0.91 ± 0.14
395		$0.60 \leq p < 0.80$	$0.77 \leq \cos\theta < 0.85$	0.99 ± 0.10
396		$0.80 \leq p < 1.20$	$0.77 \leq \cos\theta < 0.85$	1.01 ± 0.11
397		$1.20 \leq p < 2.20$	$0.77 \leq \cos\theta < 0.85$	1.01 ± 0.08
398		$2.20 \leq p < 3.50$	$0.77 \leq \cos\theta < 0.85$	1.00 ± 0.08
399		$3.50 \leq p < 10.0$	$0.77 \leq \cos\theta < 0.85$	1.03 ± 0.18
400	ν_μ N-Trks Air	$10.0 \leq p < 30$	$0.77 \leq \cos\theta < 0.85$	0.97 ± 0.51
401		$0 \leq p < 0.40$	$0.85 \leq \cos\theta < 0.90$	1.12 ± 0.55
402		$0.40 \leq p < 0.60$	$0.85 \leq \cos\theta < 0.90$	0.92 ± 0.13
403		$0.60 \leq p < 0.80$	$0.85 \leq \cos\theta < 0.90$	0.99 ± 0.08
404		$0.80 \leq p < 1.20$	$0.85 \leq \cos\theta < 0.90$	1.00 ± 0.08
405		$1.20 \leq p < 2.20$	$0.85 \leq \cos\theta < 0.90$	1.01 ± 0.07
406		$2.20 \leq p < 3.50$	$0.85 \leq \cos\theta < 0.90$	1.00 ± 0.06
407		$3.50 \leq p < 10.0$	$0.85 \leq \cos\theta < 0.90$	0.98 ± 0.13
408		$10.0 \leq p < 30$	$0.85 \leq \cos\theta < 0.90$	0.93 ± 0.45
409		$0 \leq p < 0.40$	$0.90 \leq \cos\theta < 0.97$	1.09 ± 0.51
410	ν_μ N-Trks Air	$0.40 \leq p < 0.60$	$0.90 \leq \cos\theta < 0.97$	0.93 ± 0.11
411		$0.60 \leq p < 0.80$	$0.90 \leq \cos\theta < 0.97$	0.99 ± 0.08

Table A.1: Observable normalization fit bins.

Fit Index	Sample	p [GeV/c]	$\cos\theta$	Prefit
412		$0.80 \leq p < 1.20$	$0.90 \leq \cos\theta < 0.97$	1.00 ± 0.08
413		$1.20 \leq p < 2.20$	$0.90 \leq \cos\theta < 0.97$	1.00 ± 0.07
414		$2.20 \leq p < 3.50$	$0.90 \leq \cos\theta < 0.97$	1.00 ± 0.03
415		$3.50 \leq p < 10.0$	$0.90 \leq \cos\theta < 0.97$	0.99 ± 0.10
416		$10.0 \leq p < 30$	$0.90 \leq \cos\theta < 0.97$	0.97 ± 0.28
417		$0 \leq p < 0.40$	$0.97 \leq \cos\theta < 1$	1.09 ± 0.48
418		$0.40 \leq p < 0.60$	$0.97 \leq \cos\theta < 1$	0.94 ± 0.12
419		$0.60 \leq p < 0.80$	$0.97 \leq \cos\theta < 1$	0.98 ± 0.11
420	ν_μ N-Trks Air	$0.80 \leq p < 1.20$	$0.97 \leq \cos\theta < 1$	1.01 ± 0.10
421		$1.20 \leq p < 2.20$	$0.97 \leq \cos\theta < 1$	1.01 ± 0.09
422		$2.20 \leq p < 3.50$	$0.97 \leq \cos\theta < 1$	1.01 ± 0.07
423		$3.50 \leq p < 10.0$	$0.97 \leq \cos\theta < 1$	0.99 ± 0.06
424		$10.0 \leq p < 30$	$0.97 \leq \cos\theta < 1$	0.97 ± 0.13
425	$\bar{\nu}_\mu$ RHC 1-Trk Air	$0 \leq p < 0.50$	$-1 \leq \cos\theta < 0.82$	0.99 ± 0.29
426		$0.50 \leq p < 0.60$	$-1 \leq \cos\theta < 0.82$	0.92 ± 0.14
427		$0.60 \leq p < 0.80$	$-1 \leq \cos\theta < 0.82$	1.05 ± 0.24
428		$0.80 \leq p < 1.25$	$-1 \leq \cos\theta < 0.82$	1.05 ± 0.18
429		$1.25 \leq p < 2.00$	$-1 \leq \cos\theta < 0.82$	1.02 ± 0.17
430	$\bar{\nu}_\mu$ RHC 1-Trk Air	$2.00 \leq p < 3.00$	$-1 \leq \cos\theta < 0.82$	0.87 ± 0.19
431		$3.00 \leq p < 30$	$-1 \leq \cos\theta < 0.82$	0.96 ± 0.41
432		$0 \leq p < 0.50$	$0.82 \leq \cos\theta < 0.90$	1.03 ± 0.35
433		$0.50 \leq p < 0.60$	$0.82 \leq \cos\theta < 0.90$	0.91 ± 0.12
434		$0.60 \leq p < 0.80$	$0.82 \leq \cos\theta < 0.90$	1.00 ± 0.16
435		$0.80 \leq p < 1.25$	$0.82 \leq \cos\theta < 0.90$	1.03 ± 0.15
436		$1.25 \leq p < 2.00$	$0.82 \leq \cos\theta < 0.90$	0.99 ± 0.12

Table A.1: Observable normalization fit bins.

Fit Index	Sample	p [GeV/c]	$\cos\theta$	Prefit
437		$2.00 \leq p < 3.00$	$0.82 \leq \cos\theta < 0.90$	0.99 ± 0.15
438		$3.00 \leq p < 30$	$0.82 \leq \cos\theta < 0.90$	0.93 ± 0.31
439		$0 \leq p < 0.50$	$0.90 \leq \cos\theta < 0.95$	1.05 ± 0.37
440	$\bar{\nu}_\mu$ RHC 1-Trk Air	$0.50 \leq p < 0.60$	$0.90 \leq \cos\theta < 0.95$	0.92 ± 0.11
441		$0.60 \leq p < 0.80$	$0.90 \leq \cos\theta < 0.95$	0.98 ± 0.12
442		$0.80 \leq p < 1.25$	$0.90 \leq \cos\theta < 0.95$	1.03 ± 0.12
443		$1.25 \leq p < 2.00$	$0.90 \leq \cos\theta < 0.95$	1.02 ± 0.08
444		$2.00 \leq p < 3.00$	$0.90 \leq \cos\theta < 0.95$	0.97 ± 0.08
445		$3.00 \leq p < 30$	$0.90 \leq \cos\theta < 0.95$	0.97 ± 0.19
446		$0 \leq p < 0.50$	$0.95 \leq \cos\theta < 0.99$	1.06 ± 0.37
447		$0.50 \leq p < 0.60$	$0.95 \leq \cos\theta < 0.99$	0.93 ± 0.12
448		$0.60 \leq p < 0.80$	$0.95 \leq \cos\theta < 0.99$	0.97 ± 0.11
449		$0.80 \leq p < 1.25$	$0.95 \leq \cos\theta < 0.99$	1.02 ± 0.10
450	$\bar{\nu}_\mu$ RHC 1-Trk Air	$1.25 \leq p < 2.00$	$0.95 \leq \cos\theta < 0.99$	1.00 ± 0.07
451		$2.00 \leq p < 3.00$	$0.95 \leq \cos\theta < 0.99$	0.99 ± 0.04
452		$3.00 \leq p < 30$	$0.95 \leq \cos\theta < 0.99$	0.99 ± 0.10
453		$0 \leq p < 0.50$	$0.99 \leq \cos\theta < 1$	1.07 ± 0.35
454		$0.50 \leq p < 0.60$	$0.99 \leq \cos\theta < 1$	0.89 ± 0.12
455		$0.60 \leq p < 0.80$	$0.99 \leq \cos\theta < 1$	0.99 ± 0.11
456		$0.80 \leq p < 1.25$	$0.99 \leq \cos\theta < 1$	1.02 ± 0.11
457		$1.25 \leq p < 2.00$	$0.99 \leq \cos\theta < 1$	0.99 ± 0.09
458		$2.00 \leq p < 3.00$	$0.99 \leq \cos\theta < 1$	1.01 ± 0.07
459		$3.00 \leq p < 30$	$0.99 \leq \cos\theta < 1$	0.99 ± 0.06
460	$\bar{\nu}_\mu$ RHC N-Trks Air	$0 \leq p < 0.50$	$-1 \leq \cos\theta < 0.89$	1.00 ± 0.29
461		$0.50 \leq p < 0.90$	$-1 \leq \cos\theta < 0.89$	1.00 ± 0.10

Table A.1: Observable normalization fit bins.

Fit Index	Sample	p [GeV/c]	$\cos\theta$	Prefit
462		$0.90 \leq p < 1.25$	$-1 \leq \cos\theta < 0.89$	1.04 ± 0.09
463		$1.25 \leq p < 1.60$	$-1 \leq \cos\theta < 0.89$	0.98 ± 0.14
464		$1.60 \leq p < 3.00$	$-1 \leq \cos\theta < 0.89$	0.98 ± 0.13
465		$3.00 \leq p < 30$	$-1 \leq \cos\theta < 0.89$	0.92 ± 0.33
466		$0 \leq p < 0.50$	$0.89 \leq \cos\theta < 0.95$	1.00 ± 0.31
467		$0.50 \leq p < 0.90$	$0.89 \leq \cos\theta < 0.95$	0.99 ± 0.06
468		$0.90 \leq p < 1.25$	$0.89 \leq \cos\theta < 0.95$	1.02 ± 0.06
469		$1.25 \leq p < 1.60$	$0.89 \leq \cos\theta < 0.95$	0.99 ± 0.11
470	$\bar{\nu}_\mu$ RHC N-Trks Air	$1.60 \leq p < 3.00$	$0.89 \leq \cos\theta < 0.95$	0.99 ± 0.06
471		$3.00 \leq p < 30$	$0.89 \leq \cos\theta < 0.95$	0.96 ± 0.16
472		$0 \leq p < 0.50$	$0.95 \leq \cos\theta < 0.97$	1.00 ± 0.32
473		$0.50 \leq p < 0.90$	$0.95 \leq \cos\theta < 0.97$	1.00 ± 0.07
474		$0.90 \leq p < 1.25$	$0.95 \leq \cos\theta < 0.97$	1.00 ± 0.06
475		$1.25 \leq p < 1.60$	$0.95 \leq \cos\theta < 0.97$	1.00 ± 0.11
476		$1.60 \leq p < 3.00$	$0.95 \leq \cos\theta < 0.97$	1.00 ± 0.06
477		$3.00 \leq p < 30$	$0.95 \leq \cos\theta < 0.97$	0.99 ± 0.13
478		$0 \leq p < 0.50$	$0.97 \leq \cos\theta < 0.99$	1.03 ± 0.32
479		$0.50 \leq p < 0.90$	$0.97 \leq \cos\theta < 0.99$	0.99 ± 0.07
480	$\bar{\nu}_\mu$ RHC N-Trks Air	$0.90 \leq p < 1.25$	$0.97 \leq \cos\theta < 0.99$	1.02 ± 0.07
481		$1.25 \leq p < 1.60$	$0.97 \leq \cos\theta < 0.99$	0.99 ± 0.10
482		$1.60 \leq p < 3.00$	$0.97 \leq \cos\theta < 0.99$	1.01 ± 0.08
483		$3.00 \leq p < 30$	$0.97 \leq \cos\theta < 0.99$	0.98 ± 0.09
484		$0 \leq p < 0.50$	$0.99 \leq \cos\theta < 1$	1.02 ± 0.31
485		$0.50 \leq p < 0.90$	$0.99 \leq \cos\theta < 1$	1.01 ± 0.07
486		$0.90 \leq p < 1.25$	$0.99 \leq \cos\theta < 1$	1.02 ± 0.08

Table A.1: Observable normalization fit bins.

Fit Index	Sample	p [GeV/c]	$\cos\theta$	Prefit
487		$1.25 \leq p < 1.60$	$0.99 \leq \cos\theta < 1$	0.98 ± 0.10
488		$1.60 \leq p < 3.00$	$0.99 \leq \cos\theta < 1$	1.00 ± 0.09
489		$3.00 \leq p < 30$	$0.99 \leq \cos\theta < 1$	0.99 ± 0.07
490	ν_μ RHC 1-Trk Air	$0 \leq p < 0.40$	$-1 \leq \cos\theta < 0.78$	1.10 ± 0.50
491		$0.40 \leq p < 0.60$	$-1 \leq \cos\theta < 0.78$	0.92 ± 0.12
492		$0.60 \leq p < 0.80$	$-1 \leq \cos\theta < 0.78$	1.03 ± 0.16
493		$0.80 \leq p < 1.10$	$-1 \leq \cos\theta < 0.78$	1.02 ± 0.20
494		$1.10 \leq p < 2.00$	$-1 \leq \cos\theta < 0.78$	1.08 ± 0.14
495		$2.00 \leq p < 10.0$	$-1 \leq \cos\theta < 0.78$	0.81 ± 0.31
496		$0 \leq p < 0.40$	$0.78 \leq \cos\theta < 0.84$	1.23 ± 0.50
497		$0.40 \leq p < 0.60$	$0.78 \leq \cos\theta < 0.84$	0.93 ± 0.18
498		$0.60 \leq p < 0.80$	$0.78 \leq \cos\theta < 0.84$	0.93 ± 0.09
499		$0.80 \leq p < 1.10$	$0.78 \leq \cos\theta < 0.84$	1.03 ± 0.12
500	ν_μ RHC 1-Trk Air	$1.10 \leq p < 2.00$	$0.78 \leq \cos\theta < 0.84$	1.05 ± 0.14
501		$2.00 \leq p < 10.0$	$0.78 \leq \cos\theta < 0.84$	1.00 ± 0.21
502		$0 \leq p < 0.40$	$0.84 \leq \cos\theta < 0.92$	1.17 ± 0.49
503		$0.40 \leq p < 0.60$	$0.84 \leq \cos\theta < 0.92$	0.95 ± 0.15
504		$0.60 \leq p < 0.80$	$0.84 \leq \cos\theta < 0.92$	0.97 ± 0.08
505		$0.80 \leq p < 1.10$	$0.84 \leq \cos\theta < 0.92$	1.00 ± 0.10
506		$1.10 \leq p < 2.00$	$0.84 \leq \cos\theta < 0.92$	1.00 ± 0.08
507		$2.00 \leq p < 10.0$	$0.84 \leq \cos\theta < 0.92$	1.04 ± 0.16
508		$0 \leq p < 0.40$	$0.92 \leq \cos\theta < 0.95$	1.13 ± 0.47
509		$0.40 \leq p < 0.60$	$0.92 \leq \cos\theta < 0.95$	0.99 ± 0.13
510	ν_μ RHC 1-Trk Air	$0.60 \leq p < 0.80$	$0.92 \leq \cos\theta < 0.95$	0.94 ± 0.09
511		$0.80 \leq p < 1.10$	$0.92 \leq \cos\theta < 0.95$	0.99 ± 0.07

Table A.1: Observable normalization fit bins.

Fit Index	Sample	p [GeV/c]	$\cos\theta$	Prefit
512		$1.10 \leq p < 2.00$	$0.92 \leq \cos\theta < 0.95$	1.00 ± 0.06
513		$2.00 \leq p < 10.0$	$0.92 \leq \cos\theta < 0.95$	0.99 ± 0.08
514		$0 \leq p < 0.40$	$0.95 \leq \cos\theta < 0.98$	1.06 ± 0.46
515		$0.40 \leq p < 0.60$	$0.95 \leq \cos\theta < 0.98$	0.95 ± 0.14
516		$0.60 \leq p < 0.80$	$0.95 \leq \cos\theta < 0.98$	0.97 ± 0.11
517		$0.80 \leq p < 1.10$	$0.95 \leq \cos\theta < 0.98$	1.01 ± 0.10
518		$1.10 \leq p < 2.00$	$0.95 \leq \cos\theta < 0.98$	1.00 ± 0.07
519		$2.00 \leq p < 10.0$	$0.95 \leq \cos\theta < 0.98$	0.99 ± 0.06
520	ν_μ RHC 1-Trk Air	$0 \leq p < 0.40$	$0.98 \leq \cos\theta < 0.99$	1.07 ± 0.46
521		$0.40 \leq p < 0.60$	$0.98 \leq \cos\theta < 0.99$	1.00 ± 0.15
522		$0.60 \leq p < 0.80$	$0.98 \leq \cos\theta < 0.99$	1.02 ± 0.16
523		$0.80 \leq p < 1.10$	$0.98 \leq \cos\theta < 0.99$	0.96 ± 0.10
524		$1.10 \leq p < 2.00$	$0.98 \leq \cos\theta < 0.99$	1.01 ± 0.08
525		$2.00 \leq p < 10.0$	$0.98 \leq \cos\theta < 0.99$	0.99 ± 0.04
526		$0 \leq p < 0.40$	$0.99 \leq \cos\theta < 1$	1.19 ± 0.46
527		$0.40 \leq p < 0.60$	$0.99 \leq \cos\theta < 1$	0.89 ± 0.17
528		$0.60 \leq p < 0.80$	$0.99 \leq \cos\theta < 1$	0.99 ± 0.15
529		$0.80 \leq p < 1.10$	$0.99 \leq \cos\theta < 1$	0.99 ± 0.10
530	ν_μ RHC 1-Trk Air	$1.10 \leq p < 2.00$	$0.99 \leq \cos\theta < 1$	1.00 ± 0.09
531		$2.00 \leq p < 10.0$	$0.99 \leq \cos\theta < 1$	1.00 ± 0.03
532	ν_μ RHC N-Trks Air	$0 \leq p < 0.60$	$-1 \leq \cos\theta < 0.70$	0.97 ± 0.22
533		$0.60 \leq p < 1.00$	$-1 \leq \cos\theta < 0.70$	1.02 ± 0.17
534		$1.00 \leq p < 1.50$	$-1 \leq \cos\theta < 0.70$	1.00 ± 0.14
535		$1.50 \leq p < 2.00$	$-1 \leq \cos\theta < 0.70$	1.28 ± 0.22
536		$2.00 \leq p < 10.0$	$-1 \leq \cos\theta < 0.70$	0.83 ± 0.25

Table A.1: Observable normalization fit bins.

Fit Index	Sample	p [GeV/c]	$\cos\theta$	Prefit
537		$0 \leq p < 0.60$	$0.70 \leq \cos\theta < 0.80$	0.98 ± 0.22
538		$0.60 \leq p < 1.00$	$0.70 \leq \cos\theta < 0.80$	0.99 ± 0.09
539		$1.00 \leq p < 1.50$	$0.70 \leq \cos\theta < 0.80$	1.00 ± 0.11
540	ν_μ RHC N-Trks Air	$1.50 \leq p < 2.00$	$0.70 \leq \cos\theta < 0.80$	1.03 ± 0.11
541		$2.00 \leq p < 10.0$	$0.70 \leq \cos\theta < 0.80$	1.04 ± 0.20
542		$0 \leq p < 0.60$	$0.80 \leq \cos\theta < 0.85$	1.01 ± 0.25
543		$0.60 \leq p < 1.00$	$0.80 \leq \cos\theta < 0.85$	0.98 ± 0.08
544		$1.00 \leq p < 1.50$	$0.80 \leq \cos\theta < 0.85$	1.01 ± 0.08
545		$1.50 \leq p < 2.00$	$0.80 \leq \cos\theta < 0.85$	1.00 ± 0.08
546		$2.00 \leq p < 10.0$	$0.80 \leq \cos\theta < 0.85$	0.99 ± 0.12
547		$0 \leq p < 0.60$	$0.85 \leq \cos\theta < 0.98$	0.99 ± 0.22
548		$0.60 \leq p < 1.00$	$0.85 \leq \cos\theta < 0.98$	1.00 ± 0.10
549		$1.00 \leq p < 1.50$	$0.85 \leq \cos\theta < 0.98$	1.01 ± 0.07
550	ν_μ RHC N-Trks Air	$1.50 \leq p < 2.00$	$0.85 \leq \cos\theta < 0.98$	1.00 ± 0.07
551		$2.00 \leq p < 10.0$	$0.85 \leq \cos\theta < 0.98$	1.00 ± 0.07
552		$0 \leq p < 0.60$	$0.98 \leq \cos\theta < 0.99$	1.00 ± 0.22
553		$0.60 \leq p < 1.00$	$0.98 \leq \cos\theta < 0.99$	0.99 ± 0.12
554		$1.00 \leq p < 1.50$	$0.98 \leq \cos\theta < 0.99$	1.04 ± 0.10
555		$1.50 \leq p < 2.00$	$0.98 \leq \cos\theta < 0.99$	0.99 ± 0.10
556		$2.00 \leq p < 10.0$	$0.98 \leq \cos\theta < 0.99$	0.99 ± 0.04
557		$0 \leq p < 0.60$	$0.99 \leq \cos\theta < 1$	1.01 ± 0.24
558		$0.60 \leq p < 1.00$	$0.99 \leq \cos\theta < 1$	0.99 ± 0.16
559		$1.00 \leq p < 1.50$	$0.99 \leq \cos\theta < 1$	0.97 ± 0.12
560	ν_μ RHC N-Trks Air	$1.50 \leq p < 2.00$	$0.99 \leq \cos\theta < 1$	1.06 ± 0.10
561		$2.00 \leq p < 10.0$	$0.99 \leq \cos\theta < 1$	1.00 ± 0.04